Understanding Ru Exsolution Process from $LaFe_{0.9}Ru_{0.1}O_3$ and its Impact on Catalytic Propane Oxidation Reaction

Cumulative dissertation

Presented by

Yu Wang

Submitted to the

Faculty of Biology and Chemistry

For the degree of

Doktor der Naturwissenschaften

(*Dr. rer. nat.*)

Justus Liebig University Giessen, Germany

Giessen, June 2024

This thesis is accepted as a doctoral dissertation in fulfillment of the requirements for the degree of *Doctor Rerum Naturalium* by the Faculty of Biology and Chemistry, Justus Liebig University Giessen, Germany.

1st. Reviewer Prof. Dr. Herbert Over

Institute of Physical Chemistry, Justus Liebig University Giessen

2nd. Reviewer Prof. Dr. Yanglong Guo

Research Institute of Industrial Catalysis, East China University of Science & Technology

“I declare that I have completed this dissertation single-handedly without the unauthorized help of a second party and only with the assistance acknowledged therein. I have appropriately acknowledged and cited all text passages that are derived verbatim from or are based on the content of published work of others, and all information relating to verbal communications. I consent to the use of an anti-plagiarism software to check my thesis. I have abided by the principles of good scientific conduct laid down in the charter of the Justus Liebig University Giessen „Satzung der Justus-Liebig-Universität Gießen zur Sicherung guter wissenschaftlicher Praxis“ in carrying out the investigations described in the dissertation.”

Giessen, 18.06.2024

Location, date

Signature

Acknowledgments

There are always a few decisions, which are important to one's life. Pursuing a Ph. D as the joint-training Ph.D student in this excellent group at Justus Liebig University Giessen is one of those pivotal decisions for me. Completing this doctoral thesis has been a long and challenging journey, and it would not have been possible without the guidance and support of many people to whom I am deeply grateful.

First of all, I would like to express my sincere appreciation to Prof. Dr. Herbert Over who provided me this opportunity to conduct my Ph.D project in his working group. During this period, His office door was always open whenever I needed help. He offered me continuous encouragement and maximum support for my research. Meanwhile, I am grateful for his interest in my project, for his positive attitude, and for the relaxed and pleasant working atmosphere he provided. I would say this unforgettable experience in his working group under his supervision will deeply affect me in my future life.

Equally, I want to show my gratitude to Prof. Dr. Yanglong Guo at East China University of Science and Technology for his invaluable guidance and support throughout my doctoral studies. His insightful advice, encouragement, and unwavering belief in my abilities have been instrumental in shaping my research and academic growth in the field of heterogenous catalysis. I am truly appreciative of the opportunities and knowledge he has provided me, which have been crucial to the completion of this thesis.

I would also like to thank my co-supervisor Prof. Dr. Bernd Smarsly at Justus Liebig University Giessen for his generous support in providing resources for the preparation of Ru-based perovskites, his insightful discussions on XRD and Raman data analysis, and his timely revisions of my manuscript.

Meanwhile, I want to show my sincere thanks to Dr. Jaime Gallego for his invaluable support, including his constructive suggestions, insightful comments and guidance in my research. I am also grateful for his generous assistance in my personal life.

I extent my grate to all the members of AG Over for their companionship and generous help. I am grateful to Dr. Phillip Timmer for his assistance with the DRIFTS measurement. I thank Alexander Spriewald Luciano for the help in solving all the problems I met in the lab. I am also thankful to Dr. Tim Weber and Lorena Glatthaar for the XPS measurement and corresponding data analysis. I thank Dr. Zheng Wang and Dr Wei Wang for their valuable guidance and

suggestions. I thank also Volkmar Koller and Florian Rink for their friendly discussions. Special acknowledgment goes to Gabi Sheller for her good arrangement.

Additionally, I want to express my appreciation to my friends and colleagues, including Hao Lu, Dr. Junwei Meng, Dr. Kangli Wang, Usman Ali, Dr. Rafael Meinusch, Dr. Fabian Schmitz, Lysander Wagner, Matteo Crisci, Felix Boll, Raoul Brand, Paul Debes, Luca Cartabia, Aline Trommer, Chantal Glatthaar from JLU; and Dr. Wenchao Hua, Dr. Yu Sun, Dr. Shuangshuang Zhang, Dr. Xuan Tang, Dr. Mingqi Li, Dongsheng Ye, Dr. Xiaohan Guo, Min Ding, Xiangkun Zhang, Yang You, Aijie Xu, Yake Lou from ECUST.

I am grateful to the Chinese Scholarship Council (CSC) for providing me with two years of financial support. I thank Prof. Over again for his financial support following the CSC funding, which allows me to continue my research and complete this doctoral thesis.

Last but not least, I gratefully acknowledge my parents who have always supported me in choosing my path. Wherever I am, I can always feel unwavering support behind me.

There is only one heroism in the world:

to see world as it is and to love it.

Romain Rolland

Kurzzusammenfassung

Die katalytische Umwandlung von Kohlenwasserstoffen, besonders die der leichten Alkane wie Propan, ist sowohl für die Umwelt, als auch für industrielle Anwendungen von großer Bedeutung. Oxide, die Edelmetall-Nanopartikel auf ihrer Oberfläche unterstützen, sind aufgrund ihrer großen Oberfläche vielversprechende Katalysatoren. Allerdings besitzen solche Systeme einige Probleme, wie zum Beispiel das Sintern der Nanopartikel unter Reaktionsbedingungen, wodurch die katalytische Leistung im Laufe der Zeit verringert werden kann. Die Entwicklung von Katalysatoren, welche sowohl eine hohe Aktivität, als auch Stabilität zeigen, ist daher unumgänglich. Eine reduktive Exsolution ist ein einfacher Weg zur Herstellung von Nanopartikeln, welche homogen auf der Oberfläche verteilt sind. Hierbei werden die Edelmetall-Ionen aus einer festen Lösung von Oxiden entzogen. Die dadurch entstehenden Nanopartikel sind in der Oberfläche des Materials verankert, wodurch eine bessere thermische Stabilität gewährleistet wird. Dies macht solche Materialien zu idealen Katalysatoren bei hohen Temperaturen, wie zum Beispiel für die vollständige Oxidation von Kohlenwasserstoffen.

Das Material, welches in dieser Arbeit untersucht wird, ist der Perowskit $LaFe_{0.9}Ru_{0.1}O_3$ (kurz: LFRO), in welchem 10% Fe in der B-Position mit Ru ersetzt werden. Eine Reduktion unter Wasserstoff bei 800 °C, welche eine typische Temperatur für die Exsolution ist, führt zur Bildung der verankerten Nanopartikel (LFRO-800R). Die Nanopartikel besitzen eine Core-Shell-Struktur, in welcher das aktive Ru mit einer kleinen Menge Fe in einer Legierung vorliegt und von einer inerten LaO_x Schicht umschlossen ist. Daher kommt es im Vergleich mit dem ursprünglichen LFRO zu einer geringeren katalytischen Aktivität für die Oxidation von Propan. Jedoch kann LFRO_800R mit einer oxidativen Behandlung bei 400 °C aktiviert werden, wodurch es bei einer Temperatur von 210 °C zu einer fünffach so hohen Aktivität im Vergleich zu LFRO kommt. Detaillierte Untersuchungen mittels TEM und CO-DRIFTS zeigen, dass das inerte LaO_x selektiv durch eine oxidative Behandlung bei 400°C entfernt werden kann. Währenddessen wird das freiliegende RuFe–Legierungspartikel in eine aktive oxidische Ru-Spezies überführt. Hierbei gibt es auch keine Anzeichen einer separaten FeO_x-Phase. Die Strukturentwicklung von LFRO wird bei verschiedenen Reduktionstemperaturen systematisch untersucht, um den RuFe-LaO_x Bildungsprozess aufzudecken. Beim Erhitzen von LFRO in reduzierender Atmosphäre geformt Ru an die Oberfläche und durchläuft dabei die Zustände $Ru^{3+} \rightarrow Ru^{\beta} \rightarrow Ru^{0}$. Hierbei ist Ru^{β} ein Zwischenzustand, in welchem Ru voraussichtlich diffundiert. Die Umwandlung von Ru^{3+} beginnt bereits bei 300 °C, während die nachfolgende Reduktion zu Ru^0, welche ein Indiz für die Exsolution ist, eine Temperatur von 400 °C benötigt. Wenn die Reduktionstemperatur höher als 500°C beträgt, wird Ru aus dem Volumen geformt und es kommt zur gleichzeitigen Separation von LaO_x. Ein weiteres Erhöhen der Reduktionstemperatur führt zum stetigen Wachstum der Nanopartikel, während das separierte LaO_x die Nanopartikel umschließt und so die Core-Shell-Struktur entsteht.

Die Informationen der Strukturentwicklung während der Exsolution von Ru aus LFRO unter variierenden Reaktionsbedingungen erlauben einen Einblick in die Exsolution als Strategie für die Entwicklung von Edelmetall-Katalysatoren für verschiedenste Anwendungen.

Abstract

The catalytic transformation of hydrocarbons, particularly light alkanes such as propane, is of critical importance for both environmental and industrial applications. Catalysts that support precious metal nanoparticles (NPs) on oxides have shown significant promise due to their high surface area. However, these systems often face challenges such as NP sintering under reaction conditions, which can diminish catalytic performance over time. To address this, the development of catalysts that present high activity and improved stability is essential. Reductive exsolution is a facile way to produce homogenously distributed nanoparticles through the extraction of uniformly incorporated precious metal ions from a solid oxide solution. Nanoparticles originated via exsolution anchor in the surface of the parent backbone, delivering improved thermal stability, which makes it an ideal catalyst for reactions conducted at elevated temperatures, such as hydrocarbons total oxidations.

The material studied in this work is the perovskite $LaFe_{0.9}Ru_{0.1}O_3$ (LFRO), in which 10% Fe in the B site is replaced by Ru. Reduction in hydrogen at 800 ℃ (a typical temperature for the exsolution) leads to the formation of socketed nanoparticles (LFRO-800R). These particles are revealed to be a core-shell structure in which the active Ru is alloyed with a slight amount of Fe, encapsulated by an inert LaO_x coating, thus exhibiting a lower catalytic activity compared with the pristine LFRO for the propane oxidation. However, LFRO_800R can be activated by an oxidative treatment at 400 ℃, leading to an improved activity which is five times higher than the activity of LFRO at 210 ℃. Detailed characterizations including TEM and CO-DRIFTS indicate that the inert LaO_x can be selectively removed by oxidative treatment at 400 ℃. Meanwhile, the exposed RuFe alloy particle transforms into catalytically active oxidic Ru species, without any indication of a separate FeO_x phase. The structure evolution of LFRO in each reduction temperature is systematically investigated to uncover the RuFe-LaO_x formation process. When heating LFRO in the reducing atmosphere, Ru exsolves to the surface processing through $Ru^{3+} \rightarrow Ru^{\beta} \rightarrow Ru^0$ and Ru is likely to diffuse in the form of Ru^{β} which serves as the intermediate species during this process. The transformation of Ru^{3+} initiates already at 300 °C while subsequent reduction to Ru^0 which is the sign for the exsolution requires 400 °C. When the reduction temperature is higher than 500 ℃, Ru in the bulk starts to be exsolved and accompanied by the co-segregation of LaO_x. Further enhancing of the reduction temperature leads to the continuous growth of Ru particles while the segregated LaO_x eventually encapsulates the exsolved Ru, forming the core-shell structured nanoparticles.The information on structure evolution during Ru exsolution from LFRO and following change in reaction condition provides insights into the rational design of precious metal-based catalysts via the exsolution strategy for various application scenarios.

Table of content

1. Introduction and Motivation

1.1 Ru-based catalyst in propane oxidation

Light hydrocarbons, regarded as promising alternatives to traditional fossil energy sources, have been widely used in recent years and hold a significant position in the national economy. These hydrocarbons mainly consist of alkanes and alkenes with four or fewer carbon atoms, typically existing in a gaseous state. As the typical volatile organic compounds (VOCs), the direct release of light hydrocarbons into the atmosphere is revealed to be deeply involved in the formation of ozone and chemical smog, causing severe problems to the environment and human health [1,2]. However, trace amounts of light hydrocarbons inevitably exist in the exhaust gas due to incomplete burning during the chemical process using light hydrocarbons as the fuel. Therefore, the effective removal of these trace amounts of light hydrocarbons from exhaust gases is of vital importance in modern society and has consequently attracted increasing attention over the past several decades. Addressing this issue is essential for mitigating environmental pollution and protecting public health, making it a significant research focus.

Elimination of the light hydrocarbons by direct thermal combustion is a typical strategy that can convert the light hydrocarbons into more environmentally friendly H_2O and CO_2. However, the thermal combustion of light hydrocarbons occurs only within a specific flammable range in an oxidative atmosphere. Taking propane as an example, when the propane concentration in the mixture is lower than the flammability limit (2.2 vol%) or higher than the upper flammability (9.6 vol%), the thermal combustion of propane is not favorable. On the other side, the chemical stability of light hydrocarbons requires high temperature for the cleavage of the C–H bond, leading to significant energy consumption. In contrast, catalytic combustion is proven to be an ideal strategy for the removal of trace amounts of light hydrocarbons due to its low operating temperature, (Normally lower than 500 °C) high efficiency and lack of undesired by-products [3,4]. With a catalyst, the activation energy of light hydrocarbons could be significantly reduced by providing an alternative reaction pathway that has a lower energy barrier so that the conversion of light hydrocarbons could be achieved at a lower temperature [5]. Compared to alkenes, the activation of light alkanes is more complicated due to their saturated structure. Therefore, propane is selected as the representative in this thesis for investigating light hydrocarbons catalytic combustion. In propane catalytic combustion reaction, noble metals generally exhibit superior catalytic performance compared to non-noble metals due to their

unique electronic structures and surface properties [6]. As far as precious metal-based catalysts, one of the main challenges is to improve their atomic efficiency due to their scarcity as well as their high price. In a typical heterogeneous catalytic process, initial adsorption of reactant molecules occurs on the surface of a solid catalyst, where subsequent activation transpires at specific active sites. That's to say, the active component is only accessible to the reactant molecules when it is on the surface of the catalyst [7]. In order to utilize the precious metal in an efficient way, a commonly adapted solution is diluting the precious metal by loading it onto the support.

The most common catalysts for light hydrocarbons primarily use platinum or palladium as active components[8–10]. However, the relatively high price of Pt and Pd motivate the search for their replacement. Ruthenium is known to be one of the most active elements in the activation of C–H and C–C bonds. More importantly, the price of Ru is much lower than Pt and Pd (the average price of Pt and Pd from January 1st 2024 to April 30th 2024 is around 32000 \$/kg and 35000 \$/kg, respectively, while the average price of Ru during the same period is around 15000 \$/kg), offering significant potential as a cost-effective alternative to the current commercial Pt-based and Pd-based catalysts [11]. Recent studies have demonstrated that Ru-based catalysts exhibit excellent catalytic activity for propane oxidation reactions [12–14]. For instance, Okal *et al.* reported that Ru/γ-Al_2O_3 catalyst (4.6 wt.% Ru) achieved a turnover frequency (TOF) of 0.0035 s^{-1} for propane combustion at 175 °C and reached full conversion at temperatures lower than 200 °C. However, residual chlorine species from the $RuCl_3$ precursor and the pretreatment atmosphere can affect the propane catalytic performance greatly. The optimal catalyst is the Cl^- free sample treated with H_2 and its exceptional activity can be attributed to either non-stoichiometric Ru_xO_y nanoclusters or large Ru metal particles coated with a thin layer of RuO_2. Under oxygen-rich conditions, the highly active RuO_x nanoclusters tend to sinter into crystalline RuO_2 particles when the calcination temperature is enhanced to 600 °C, leading to a decrease in activity [12]. To address this issue. researchers have explored methods to stabilize RuO_2 nanoparticles by introducing additional additives. For instance, Adamska and Baranowska *et al.* incorporated Mo and Re into Ru/Al_2O_3, producing bimetallic Ru-based catalysts. Among these, the Ru-Mo/γ-Al_2O_3 (5 wt.% Ru, 1.6 wt.% Mo) catalyst achieved a 95% propane conversion at 200 °C, with a TOF (turnover frequency) as high as 0.034 s^{-1} at 165 °C [15]. In another study, Ledwa *et al.* prepared $Ru_xCe_{1-x}O_{2-y}$ particles using the reverse microemulsion method and then supported them on an γ-Al_2O_3 carrier to obtain the final catalyst. Further characterizations have confirmed that this catalyst can effectively stabilize RuO_x active species after thermal calcination at 800 °C and achieved a 50% propane

conversion at 225 °C [16,17]. Seeking to enhance the interactions between Ru-CeO_2 mixed oxides and Al_2O_3 support, Liu *et al.* synthesized the nano-flower sheet-like alumina (NF-Al_2O_3) featuring abundant unsaturated pentacoordinate Al^{3+} site. These sites played a role in anchoring the Ru-CeO_2 active phase, resulting in excellent thermal stability and high catalytic activity for propane combustion reaction [18].

What's more, the catalytic performance of Ru-based supported catalysts is significantly influenced by the properties of the support material. Compared to Al_2O_3, CeO_2 not only disperses the RuO_x more effectively but also enhances the propane oxidation rate by participating in oxygen activation. This enhancement is attributed to the existence of abundant oxygen vacancies resulting from the rapid transformation between Ce^{3+} and Ce^{4+}, thereby exhibiting superior catalytic performance with the same Ru loading [14,19]. With the well-defined morphology of CeO_2 support, Wang *et al.* observed that the morphology of CeO_2 support does not significantly affect the chemical states of Ru species but altered the interaction between Ru and CeO_2, varying the oxygen vacancy concentration in the interface between Ru and CeO_2 [20]. The catalytic activity of propane combustion on Ru/CeO_2 was positively correlated with the oxygen vacancy concentration. Ru supported on CeO_2-nanorods, which predominantly expose CeO_2 (110) facet possessing the most oxygen vacancies, exhibited superior activity and stability in propane combustion compared to Ru supported on CeO_2-nanocubes and CeO_2-nanoctahedrons. Using defect-rich CeO_2 nanosheets as the support for Ru, a plentiful Ru-O-Ce interface can be achieved in Ru/CeO_2, which can efficiently accelerate the propane adsorption [21]. Ru/CeO_2 prepared by Sun *et al.* using the co-precipitation method exhibited superior activity and stability during propane combustion reaction due to the synergistic effect of different states of Ru species [22]. Detailed characterization demonstrated that the unsaturated RuO_x ($x < 2$) with high dispersity and low oxidation state formed on the CeO_2 surface provides the sites for propane adsorption and activation while the Ru in the CeO_2 bulk in the form of Ru-O-Ce can efficiently enhance the oxygen mobility. As a commercial catalyst in the Deacon reaction, RuO_2/TiO_2 has also been investigated in the propane combustion reaction [23,24]. Debecker *et al.* found that the Ru can selectively migrate to the rutile TiO_2 from anatase TiO_2 within the temperature range of 150 to 250 ℃ while further increasing the calcination temperature above 300 ℃ led to the irreversible crystallization and sintering, resulting in the remarkable decline on the catalytic performance in propane oxidation reaction [25]. The RuO_2/TiO_2 activity could be enhanced by pretreating in a reducing atmosphere. The catalytically active species were considered to be the metallic Ru, and the involvement of oxygen species from the interface of Ru and TiO_2 has been proven in the

reaction[26,27]. However, stabilization of the Ru by the enhanced metal support interaction between Ru using rutile TiO_2 seems not to work in the propane combustion reaction, since RuO_2/TiO_2 turned out to be the lowest activity among the chosen supports [28]. Another efficient approach to improving the thermal stability of the precious nanoparticles is encapsulating them with porous materials, which can act as the physical barrier to impede particle migration and prevent further sintering [29–31] The core-shell structure was initially introduced to satisfy this target. Li *et al.* synthesized the Ru-SiO_2 core-shell structure and this catalyst retained good stability even at temperatures as high as 650 °C, which could be attributed to the protection effect of the amorphous SiO_2 nano shell [32]. Zeolites have high thermal stability and high surface areas contributed by the uniform microporous structures, making them promising candidates to confine precious nanoparticles. [33]. Thanks to the development of advanced synthesis methods, the stabilization of precious nanoparticles with physical confinement is possible nowadays [34]. Tao et al fixed a series of ultrafine Ru nanoparticles whose average particle size was lower than 0.95 nm in the silicate-1 zeolite by a simple one-pot method. This catalyst can reach 95 % propane conversion at a temperature of 294 °C [35]. Most importantly, the encapsulated Ru nanoparticle exhibited superior thermal stability than the supported one prepared by the impregnation method, which could be attributed to the confinement effect of the zeolites. In addition to the confinement effect, the zeolite frame can also affect the electronic structure of confined precious metal species. It was revealed that the Al site of the zeolite skeleton was involved in the formation of more Ru-O-Al phase which played a role in preventing the agglomeration of Ru nanoparticles in harsh environments [36]. What's more, the Al site as a kind of Bronsted acid site contributed also to the adoption and activation of the reactant molecular.

However, these conventional techniques for the fabrication of supported precious metal catalysts often lack precision in controlling the particle size and distribution of the precious nanoparticle. Moreover, the synthesized supported catalyst always undergoes the undesired agglomeration during the calcination or high-temperature operation due to the relatively weak interaction between support and metal particle, decreasing the catalytic performance as well as shortening the operational lifespan [37]. Although some advanced methods are introduced to prepare high thermal stability Ru-based catalysts, the complicated process and the high requirement on the precursor limit the large-scale production [34,38]. Several decades ago, the exsolution was reported to be a promising strategy to address the challenges raised by conventional methods.

1.2 Exsolution background

1.2.1 exsolution and perovskites

Exsolution is a crucial process in materials science, characterized by the separation of a secondary phase from an initially homogeneous solid solution without the removal or addition of material. This phenomenon is particularly important in the preparation of precious metal-based catalysts. For these catalysts, the catalytically active precious metal must first be homogeneously incorporated into the lattice of the matrix oxide. However, the inherent differences in radius, valence and the structure of their oxides among different cations limit the formation of the oxide solid solution, bringing the obstacle for the preparation of precious metal-based catalyst by the exsolution strategy [39].

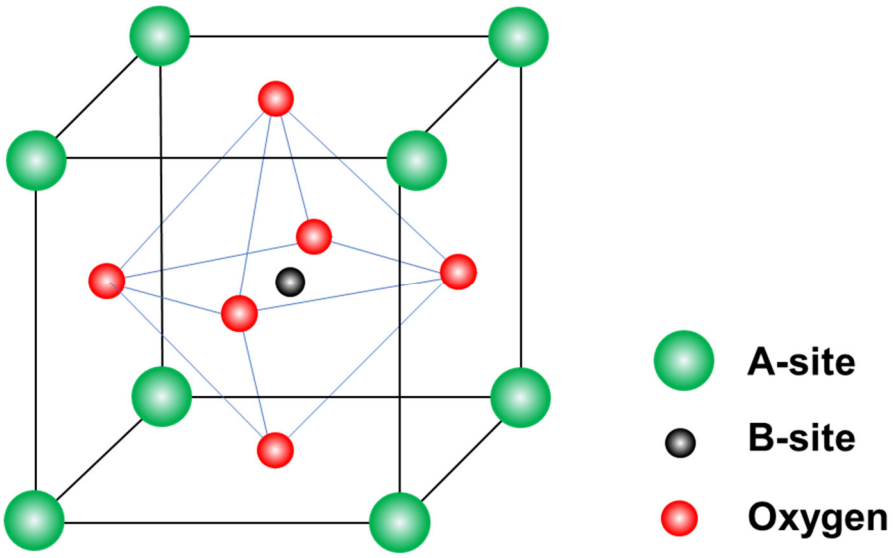

Figure 1.1 Schematic illustration of ideal cubic ABO_3 perovskite structure.

As one of the popular materials in scientific research, ABO_3 perovskite oxides with high structural flexibility provide the tunability to form a solid solution so that it is commonly considered to be the ideal candidate as the starting materials for exsolution. As illustrated in **Figure 1.1**, the ideal ABO_3 perovskite has a cubic structure in which the A-site element occupies the cube center with a 12–fold coordination while the B-site element stays at the octahedron center coordinated with six oxygen [40]. In general, the A site of perovskite structure is normally occupied by the alkali, alkali earth metal cations or lanthanides cations which have a relatively larger ionic radius while the B site consists of the variable valence transition metal cations. Usually, the A-site element plays a role in stabilizing the perovskite

structure while the B-site element is the active component for a catalytic process. According to this principle, the precious metal cations (Pt, Pd, Ru, Rh) are normally thought to stay in the B site of the perovskite structure. It is worth mentioning that Ag^{1+}, as the precious metal cation, is located in the A site of perovskite structure due to its quite large ionic radius. In order to evaluate the possibility of the formation of a stable perovskite structure, a tolerance factor (t) equation is proposed by Goldschmidt in **Eq**. **1** [41]:

$$t = \frac{(R_A + R_O)}{\sqrt{2} \bullet (R_B + R_O)} \ (0.75 < t < 1.13) \qquad \textbf{\textit{Eq}. 1}$$

where the R_A and R_B represent the radius of the A-site cation and B-site cation, respectively, and R_O means the radius of oxygen ions. The tolerance of perovskite structure allows the partial substitution in both A-site and B-site, which can modify the structure property of the host perovskite oxide.

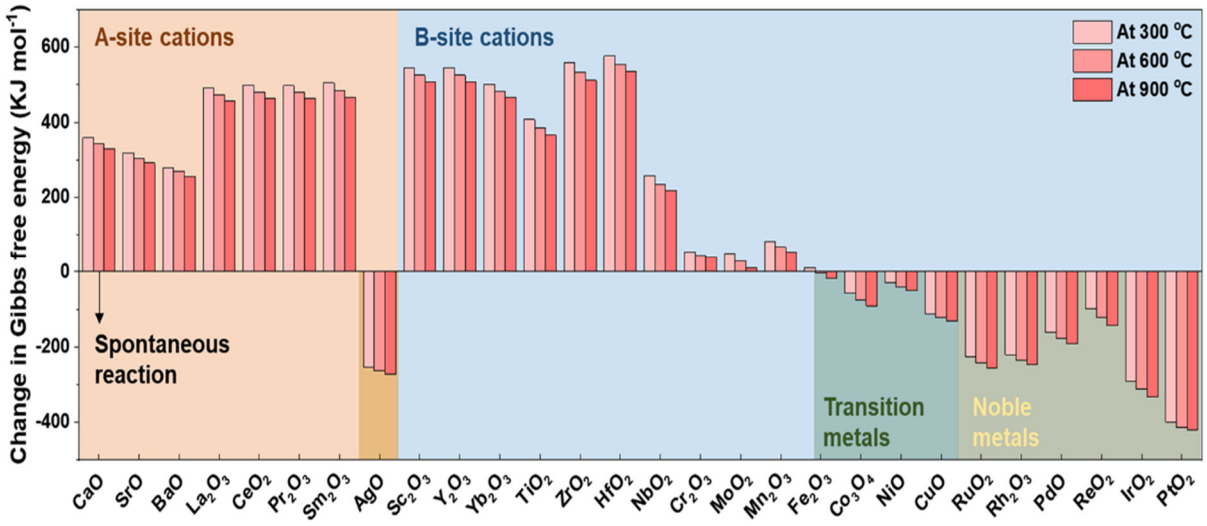

Figure 1.2 Variations of Gibbs free energy from oxide to corresponding metal in H_2 at 300, 600, 900 °C [42]. Copy right from Springer Nature.

For the cations in the perovskite structure, the exsolution order largely depends on the ease with which they can be reduced to the metal. Therefore, we could use the Gibbs free energy change between metal ions in the parent oxide lattice to desired metals (ΔG) to roughly estimate the exsolution order of different cations. As shown in **Figure 1.2**, the difference in Gibbs free energy between the precious metal oxides to metal is negative which is relatively lower than the other transition metals, suggesting that the precious metal cations could be preferentially exsolved when exposed to the reducing atmosphere. This characteristic provides the fundament of designing the precious metal-based catalyst by exsolution strategy. At the same time, the

negative ΔG could also be calculated in some 3d transition metals, like Co, Ni and Cu, indicating that the corresponding cations could also be exsolved. It should be mentioned that the Fe, which is quite common in the B site of the host perovskite position shows the ΔG around 0 is not easily exsolved when it solely occupies the B site of the perovskite structure [43]. The other B-site cations, as well as the lanthanides or alkaline earth cations in the A site of the perovskite structure which are calculated to the positive ΔG can hardly be exsolved [44].

Initial studies about exsolution are conducted on stochiometric perovskite ABO_3 (A/B=1), and precious metal cations (ΔG<0) which could be preferentially exsolved is homogenously incorporated into the matrix during the preparation. It was reported that Pd in $LaFe_{0.57}Co_{0.38}Pd_{0.05}O_3$ can be expelled to the surface under the reducing atmosphere, opening the possibility of preparing the precious metal-based catalysts by exsolution strategy [45]. With the help of the density functional theory (DFT) calculations, $LaPdO_{3-y}$ was revealed to form in the vicinity of the $LaFe_{1-x}Pd_xO_3$ surface which is stabilized by oxygen vacancies, allowing the efficient diffusion of Pd upon reduction [46]. Pt particles about 1–3 nm in diameter exsolved from $La_{0.9925}Ba_{0.0075}Al_{0.995}Pt_{0.005}O_3$ after low-temperature reduction at 600 ℃ were uniformly dispersed on the perovskite oxides surface, contributing to the good oxygen reduction reaction activity and stability in basic condition [47]. Similarly, the homogenously distributed Ru, Rh, Ni particles could be achieved by the reductive treatment at elevated temperatures.

1.2.2 Exsolution mechanism and the affecting factors

The reductive exsolution process is proposed to be four steps, including ionic diffusion, reduction, nucleation and growth (**Figure 1.3**) [48]. It is widely accepted that the reductive exsolution is triggered by the formation of oxygen vacancies. When exposing the perovskite oxides to the reducing atmosphere, the oxygen ion in the perovskite structure is released from the lattice, leaving the oxygen vacancies in the perovskite structure. (**Eq.2**)

$$ABO_3 + \alpha H_2 \rightarrow ABO_{3-\alpha} + \alpha O_V^{\cdot\cdot} + \alpha H_2O \qquad (\mathbf{Eq.2})$$

$$ABO_{3-\alpha} \rightarrow (1 - \alpha)ABO_3 + \alpha B + \alpha AO \qquad (\mathbf{Eq.3})$$

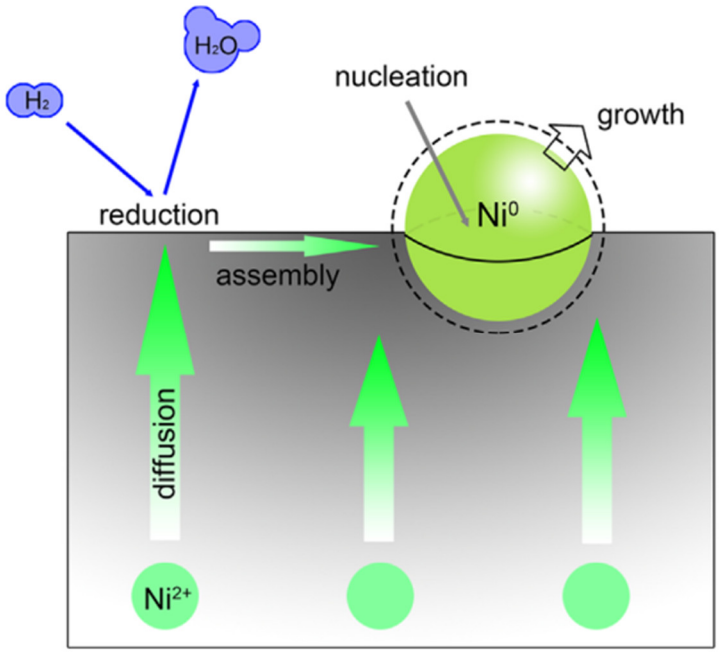

Figure 1.3. Mechanism of the B-site cations exsolution exemplifies with Ni^{2+}. Reprinted with permission from reference[48]. Copy right 2016 Elsevier.

Driven by the oxygen ion gradient, the oxygen vacancies gradually diffuse into the bulk lattice of the perovskite matrix. With a substantial accumulation of oxygen vacancies within the bulk, the stability of the perovskite structure is compromised, leading to the spontaneous diffusion of the metal cations towards the surface. Several investigations revealed that the exsolution of metal cations diffuse predominantly along the defective antiphase boundary [49], which is of vital importance for controlling particle density and distribution [50]. Once the cations reach the surface, they are trapped by the surface point defects (such as oxygen vacancies or cations vacancies) which act as the nucleation sites and are then reduced [51]. (**Eq. 3**) As the reduction continues, more cations from the bulk are exsolved to the surface, either forming additional clusters or migrating into the existing one, thereby increasing their size.

Wang *et al.* utilized $SrTi_{0.65}Fe_{0.35}O_3$ thin film to demonstrate that a rapid oxygen release rate can not only shorten the exsolution on the set time but enhance also the quantity of exsolved Fe [52]. Given the importance of oxygen release via oxygen vacancy formation in the host oxide for cation exsolution, various methods have been employed to introduce intrinsic and extrinsic oxygen vacancies to facilitate the exsolution process. These methods include adjustments to reduction temperature, oxygen pressure, A-site deficiency and lattice strain, etc.[53,54]

The most common method to trigger the exsolution is increasing the reduction temperature, which accelerates the formation and diffusion of oxygen vacancies. The population of exsolved Rh from $La_{0.43}Ca_{0.37}Rh_{0.01}Ti_{0.99}O_3$ revealed a reverse volcano curve as the reduction temperature varied from 500 ℃ to 1000 ℃. When the reduction temperature was lower than 700 ℃, the number of dissolved particles was positively correlated with the reduction temperature while a further increase in the temperature resulted in the decline of the quantity of exsolved Rh particles [55]. A similar result that the higher temperature accelerated the cations' exsolution but also led to the low density of the exsolved particle due to the agglomeration was also derived by Kim *et al* [56]. The exsolution is significantly affected by the oxygen partial pressure (pO_2) in the reducing atmosphere. Generally, the low pO_2 atmosphere is more favorable for the formation of oxygen thus facilitating the B-site cations exsolution. By varying the pO_2, it is further revealed that the lower pO_2 favors the high density of small particles while the higher pO_2 leads to the low density of big particles at the constant temperature [56]. Similar observations made by Gao *et al.* showed that the Ni exsolved from $La_{0.4}Sr_{0.4}Sc_{0.9}Ni_{0.1}O_{3-\delta}$ under pure H_2 formed larger particles compared to those exsolved in 20 vol% H_2/Ar [48]. These effects are related to changes in the nucleation kinetics, which could be described by classical nucleation theory [57]. During the exsolution, the nucleation rate of exsolved nanoparticles N_v (number of nuclei / (m^2/g)) could be expressed as the form in **Eq.4**,

$$N_V = -\frac{\Delta G}{kT} \qquad \boldsymbol{Eq.4}$$

where ΔG represents the critical nucleation energy barrier, k is the Boltzmann constant and T denotes the temperature. When pristine perovskite oxide is subjected to harsh conditions, such as high reduction temperatures or low oxygen partial pressures, the diffusion rate of the target cation is significantly accelerated, whereas the nucleation rate is considerably reduced. This leads to the formation of large particles with low density on the surface. A low pO_2 atmosphere could also be achieved or modified using CH_4, CO, UHV (ultra-high vacuum) or even by the introduction of water vapor [58,59]. Interestingly, when the reducing atmosphere shifts from H_2 to CO, the geometry of the exsolved particles changes from quasi-spherical to cubic [58]. This transition is notable because it suggests a strong influence of the gas environment on the morphological evolution of exsolved particles, highlighting the importance of precise control over atmospheric conditions in tailoring material properties.

The introduction of A-site deficiency (A/B<1) is an effective way to increase the intrinsic vacancies utilizing the structure tolerance of the perovskite structure. This kind of oxygen

vacancies, serving as the point defect, plays a role in initiating exsolution [44]. As illustrated by **Eq. 2**, the exsolution of B-site cations from stochiometric perovskite is usually accompanied by the co-segregation of the A-site element, which in turn impedes the B-site element exsolution due to its accumulation on the surface as AO. However, the A-site deficiency perovskite provides an efficient solution to avoid the co-segregation of the AO as indicated by **Eq. 5**.

$$A_{1-x}BO_{3-y} \rightarrow (1-x)ABO_3 + xB + zO_2 \qquad (\boldsymbol{Eq\ 5})$$

What's more, the A-site deficiency destabilizes the perovskite structure when exposed to the reductive atmosphere at elevated temperatures. This destabilization is driven by the formation of more stable stoichiometric perovskite oxides. To systematically explore the correlations between cation non-stoichiometry and the exsolution behavior, Neagu *et al.* prepared the A-site deficient perovskite $La_{0.52}Sr_{0.28}Ni_{0.06}Ti_{0.94}O_3$ and stoichiometric perovskite $La_{0.3}Sr_{0.7}N_{i0.06}Ti_{0.94}O_{3.09}$ which exhibited different behavior after exposing to the reducing atmosphere at elevated temperature. Homogenously distributed Ni particles were visible at the surface of A-site deficient $La_{0.52}Sr_{0.28}Ni_{0.06}Ti_{0.94}O_3$ perovskites thin film while no significant surface evolution was observed in the stoichiometric perovskite $La_{0.3}Sr_{0.7}N_{i0.06}Ti_{0.94}O_{3.09}$. Similarly, a high density of exsolved Ni particles could be obtained on the surface (almost 15 times) compared with stochiometric perovskite film reduced at the same condition [49]. The strong driving force induced by A-site deficiency can not only accelerate the exsolution of reducible cations but also contribute to the exsolution of unreducible cations like Mn and Ti, forming MnO_x and TiO_x in $La_{0.4}Sr_{0.4}TiO_3$ and $La_{0.4}Sr_{0.4}Mn_{0.06}Ti_{0.94}O_{3-\delta}$, respectively [44]. Equally, oxygen vacancies could also be achieved by replacing A-site cations with those of lower oxidation states. For instance, the oxygen vacancy concentration derived by XPS in $Cu/La_{0.3-x}Sr_{0.6+x}TiO_{3-\delta}$ ($0 < x < 0.3$) correlates directly with the x value, indicating a systematic increase in vacancies with increasing substitution. [60].

The replacement of host B-site element by a dopant with different radii and valence state introduces not only the intrinsic oxygen vacancies, but also enhances the lattice distortion, significantly influencing the exsolution behavior. $LaFeO_3$, a classic host for the element doping in both A-site and B-site, is frequently studied in the literature due to its thermal stability in both reductive and oxidative atmospheres. As illustrated in **Figure 1.1**, the exsolution of Fe is not thermal dynamically favorable when it solely occupies the B site of the perovskite structure. However, the exsolution of Fe could be achieved as a result of decreased segregation energy by doping another easily exsolvable cation. Meanwhile, the easily exsolved cations are reduced firstly into small metallic particles on the surface serving as an active site for the hydrogen

dissolution, promoting the further reduction by spillover effect [61]. For example, the CoFe alloy was observed on the surface of $La_{0.9}Fe_{0.9}Co_{0.1}O_3$ after a reduction of 500 ℃ while no particle could be found in $La_{0.9}FeO_3$ treated in the same condition. The different exsolution behavior on these two systems could be explained by the lower formation energy of Co-Fe bond on the surface than the Fe-Fe bond [62]. Liang *et al.* revealed that Ru doping can accelerate the exsolution of anchored FeCo(Ru) alloy through the combination of experimental results and DFT calculation [63]. By varying the Ni doping level in $(La0.75Sr0.25)(Cr_{0.5}Fe_{0.5-x}Ni_x)O_3$ perovskites, Papargyriou *et al.* demonstrated that the oxygen deficiency induced by the high Ni doping level could lower the valence of Fe^{3+}/Fe^{4+} and Ni^{2+}, thus accelerating NiFe exsolution [64]. Notably, part of the Fe can migrate from the exsolved MFe (M = Ni, Cu) alloy due to its high oxygen affinity, even in the reductive atmosphere containing a trace amount of oxygen, forming the MFe@FeO_x core-shell structure [65,66]. This unique core-shell structured nanoparticle decorated perovskites containing plentiful oxygen vacancies exhibit unexpectable catalytic activity and long-term stability when used as the cathode for CO_2 electrolysis. The core-shell structured Pd-NiO was also reported to be prepared by the exsolution from $LaFe_{0.9-x}Ni_xPd_{0.1}O_{3-\delta}$ and the shell thickness of NiO could be modified by varying the Ni content [67]. Recently, a topotactic ion exchange/exsolution method proposed by Joo *et al.* illustrated that the exsolution of host Co in $PrBaMn_{1.7}Co_{0.3}O_{5+\delta}$ could be promoted by deposited Fe due to the different segregation energy of these two elements [54]. As demonstrated by these examples, the exsolution of host B-site elements promoted by the doping of cations with low segregation energy consistently achieves the formation of bimetallic particles on the surface of perovskite. This provides an efficient strategy to prepare bimetallic nanoparticle catalysts via the exsolution technique.

The exsolution behavior from perovskite oxides is also altered by the crystal orientations. To thoroughly examine the effects of surface termination in exsolution processes, recent research employs epitaxially prepared perovskite thin film samples. Compared with the (100) and (111) orientation of $La_{0.4}Sr_{0.4}Ni_{0.03}Ti_{0.97}O_{3-\delta}$, the Ni can be preferentially exsolved from more defective (110), which could be attributed to the lower nucleation barrier due to the existence of an abundant surface defect [68]. Supported by the DFT calculation conducted by Gao *et al.*, the Ni segregation energy was revealed with as strong orientation-dependent effect in the $SrTiO_3$-based model system, and Ni could be preferentially exsolved from the (100) orientation [69]. On the contrary, Kim *et al.* revealed that the (111) oriented film of $La_{0.2}Sr_{0.7}Ti_{0.9}Ni_{0.1}O_{3-\delta}$ generated the most Ni particles with the smallest particle size and deepest embedment than the

film with (001) and (110) orientations, which could be explained its highest interictal energy that affects the nucleation behavior [70].

Lattice strain can affect the formation of defects in perovskites and regulate the extent of exsolution. Moreover, lattice strain can alter the electronic structure, local bonding configuration, surface energy gap, interface cation chemistry, and surface oxygen stoichiometry [71,72]. By growing $La_{0.2}Sr_{0.7}No_{0.1}Ti_{0.9}O_{3-\delta}$ thin film on a series of perovskite substrates with different lattice parameters, Han et al. modified the extent of thin film lattice strain and checked their exsolution behavior [73]. The findings revealed that the exsolved nanoparticles on the compressed strain-induced sample had a reduced average particle size and a greater population density in comparison to those on the tensile strained samples. Differently, the tension strain was revealed to be related to the formation of oxygen vacancies and Schottky defect, serving as the nucleation site on the $La_{0.6}Sr_{0.4}FeO_3$ thin film, which was beneficial for Fe exsolution [51]. Beside the mismatch of lattice parameters, the lattice strain can also be induced by the introduction of ions with different radii and valence [74], which is already presented in the former part.

Most of the nanoparticle exsolution is achieved by heating the sample in the reduction atmosphere, overcoming the energy barrier that triggers the exsolution. Theoretically, this energy can be delivered to the perovskites in alternative forms, such as light, electricity, or even plasma, as long as it can initiate the formation of oxygen vacancies and the reduction of cations [42,75–78]. For example, electrochemical switching has been proved to be an efficient strategy and demonstrated significant advantages over hydrogen gas reduction [79]. Applying electrochemical switching to $La_{0.43}Ca_{0.37}Ni_{0.06}Ti_{0.94O3-\delta}$ fuel electrode at a potential of 2 V in 50% H_2O/N_2 environment at 900 ℃, resulted in a more than threefold increase in exsolved Ni nanoparticle density compared to reduction for 17 hours at the same temperature in hydrogen. Jo *et al.* demonstrated that electrochemical reduction at 2.3 V for a few seconds led to the rapid growth of numerous small-sized nanoparticles in a few seconds, which could be explained by the reduced cations diffusion barriers and lowered growth limitations [80,81].

1.3 Novel features of perovskite

1.3.1 socketed structure

In contrast to deposited particles, exsolved particles exhibit a fascinating geometry known as the socketed structure, where the exsolved particle is partially submerged into the oxide support. This distinctive feature of the exsolution-based perovskite system enhances the interaction between the particle and the substrate. As a result, the materials demonstrate high activity and good resistance to coking and sintering [82].

Ni particles in **Figure 1.4a** fabricated by reducing the $La_{0.4}Sr_{0.4}Ni_{0.03}Ti_{0.97}O_{3-\gamma}$ were observed to pin into the perovskite with around 30% of their volume submerged into the parent oxide surface. The exsolved Ni particles can be selectively etched by concentrated HNO_3, leaving pits exhibiting a similar size distribution and density (**Figure 1.4c**) as seen in the Ni particle exsolved sample in **Figure 1.4d**, confirming the socketed structure [68]. Using the environment TEM, Neagu *et al.* revealed the perovskite surface evolution during Ni exsolution. During the exsolution process, the metal phase nucleates below the surface of the parent oxide matrix, setting the stage for the partial embedding of the particles. As the exsolved nanoclusters grow and migrate from the subsurface to the surface, they deform the surrounding oxide matrix, creating elastic strain fields. These strain fields contribute to the partial embedding or "socketing" of the particles within the matrix. There is a balance between the elastic strain energy and the surface energy. As a particle moves towards the surface, the reduction in elastic energy (due to the release of strain) is countered by an increase in surface energy. The socketed configuration represents an energetically favorable state where these competing energies are balanced. The migration process creates a pit on the surface of the matrix, and as the nanoparticle emerges, it remains partially embedded in this pit, leading to the characteristic socketed structure [83].

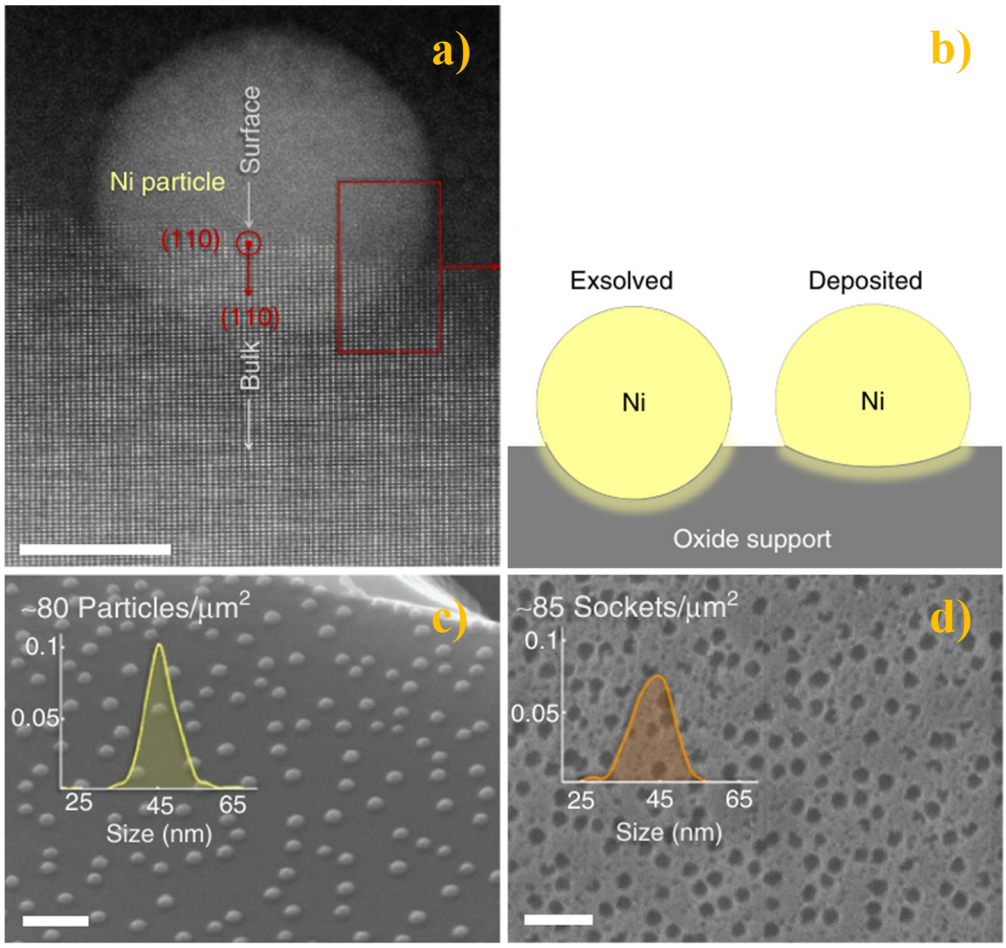

Figure 1.4. (a) High-angle annular dark-field imaging (HAADF) of a Ni nanoparticle exsolved from (110) facet, scale bar, 10nm (b) schematic illustration of the particle–substrate interface for transitional deposited and exsolved nickel particles, SEM images of exsolved Ni particles from $La_{0.52}Sr_{0.28}Ni_{0.06}Ti_{0.94}O_3$ (c) before and (d) after HNO_3 etching. the corresponding Ni particles and hole distribution. Reprinted with permission from reference [68]. Copy right from Springer Nature.

This socketed structure confines the mobility of exsolved particles on the surface, thereby impeding Oswald ripening at high temperatures, making it a strong candidate for various applications, such as high-temperature solid oxide electrolysis cells (HT-SOEC). Nano-socketed Fe-Ni alloy nanoparticles structured $(La_{0.6}Sr_{0.4})_{0.95}Ni_{0.2}Fe_{0.8}O_{3-\delta}$, fabricated by using the exsolution strategy, serve as the cathode exhibiting good stability and resistance to coking during a100-hours test in the CO_2 electrolysis at 850 °C [84]. Similarly, Wang *et al.* reported that self-grown Ni-Fe alloy particles prepared by reducing $Sr_2Fe_{1.3}Ni_{0.2}Mo_{0.5}O_{6-\delta}$ can achieve an electrolysis current density of 1257 mA/cm at 850 °C at an operating voltage of 1.3 V when used as a hydrogen oxidation electrode [85].

1.3.2 Redox reversibility

The thermal stability and durability of catalysts under elevated temperatures are of great importance for practical applications. Generally, the nanoparticle on the supported catalyst prepared by the conventional deposition method intents to migrate and agglomerate into the big particle, leading to the deactivation of the catalyst as a result of the decrease of the active site quantity. In particular, Ru can be transferred into volatile RuO_3 and RuO_4 when it is exposed to an oxidizing atmosphere at a temperature higher than 600 ℃, which limits the application of Ru-based catalysts in high-temperature oxidation reactions.

As one of the novel features of the exsolution-based perovskite oxide, the reversibility which means the exsolved metallic particle could dissolve back to its parent matrix by exposing it in the oxidative atmosphere at elevated temperature is attracting more and more attention. Initially reported in 2002, Nishihata *et al.* revealed that Pd in $LaFe_{0.57}Co_{0.38}Pd_{0.05}O_3$ can reversibly move back and forth in the form of solid solution (Pd as cation in the perovskite structure) and segregation (Pd nanoparticle), allowing the possibility of reactive the catalysts which suffered deactivation by coking, coarsening, sulfur poisoning [86]. This unique reversibility feature opens the door for the potential application in automotive emissions control and attracts worldwide attention, gaining the name of "intelligent catalyst" [87,88]. In order to get a more fundamental understanding of the reversibility, Density functional theory (DFT) was subsequently utilized. With it, Hamada *et al.* proposed a possible mechanism for the regeneration of Pd catalysts in $LaFe_{1-x}Pd_xO_3$. The Pd exists in the form of $LaPdO_{3-y}$ stabilized by the oxygen vacancies in the near-surface region of $LaFe_{1-x}Pd_xO_3$, providing a short diffusion path that allows the facile exsolution and redissolution during the redox treatment [46]. Steiger *et al.* demonstrated that the exsolution of Ni from $LaFe_{1-x}Ni_xO_3$ at 600 ℃ could be fully recovered by reoxidation at 650 ℃ for 2 h. The Ni particle achieved by the exsolution strategy exhibited good activity and highly redox stability in the CO_2 hydrogenation reaction [89]. Co-Fe nanoparticles expelled from $La_{0.3}Sr_{0.7}Cr_{0.3}Fe_{0.6}Co_{0.1}O_{3-x}$ can completely dissolve into the perovskite matrix when oxidized at 800 ℃ while they were still on the surface as the transition metal oxide when oxidized at 700 ℃ [90]. The preparation of perovskite oxides always requires high calcination temperature for the homogenous rearrangement of the different ionic, making the high crystallinity and low surface area (1–15 $m^2 \cdot g^{-1}$). Under the reductive atmosphere, the migration of exsolvable cations is sometimes limited by the long diffusion path. Although the diffusion of the cations from the deep bulk could be achieved by varying the reduction temperature or oxygen partial pressure, the undesired agglomeration of exsolved particles

somehow decreases the quantity of the active site. Recently, the reversibility of perovskite oxide has been utilized to overcome this problem. Lv *et al.* demonstrated that in $Sr_2Fe_{1.4}Ru_{0.1}Mo_{0.5}O_{6-\delta}$, Ru could be enriched in the near-surface through repeated redox treatment. The density of exsolved RuFe alloy particles increased approximately 3.6 times after four redox cycles, while their sizes remained similar. They further explored the dissolution of RuFe alloy and revealed that the Fe in the alloy first migrates to the surface, forming the FeO_x shell at an oxidation temperature of 200 ℃. Upon further increasing the oxidation temperature to 800 ℃, dissolution of FeO_x and subsequent disappearance of RuO_x were observed [91].

Contrary to the general impression, the exsolved particle is sometimes found to remain pinned in the perovskite oxide surface during the re-oxidation process. It has been observed that the dissolution of particles back into perovskite becomes limited after multiple exsolution and dissolution cycles [92]. With high-angle annular dark-field scanning transmission electron microscopy (HAADF-STEM), Katz *et al.* showed that the exsolved Pt cluster with a small size (around 1 nm) could dissolve back the perovskite matrix (Pt-doped $CaTiO_3$) while the relatively big Pt particles suffered agglomeration upon oxidation at 800 ℃ [93]. The dissolution of the exsolved particle upon oxidation is also affected by the chemistry of structural defect.

Compared with the particles exsolved from the A-site deficient perovskite, the dissolution of metal particles expelled from stochiometric perovskite is more favorable. As far as the stochiometric perovskite (ABO_3), the exsolution of B site cation will lead to the co-precipitation of the same amount of A site oxide under a reducing atmosphere theoretically to reach the stable stoichiometric state, which can, in turn, facilitate the metal dissolution by reacting with it to reconstruct the pristine oxides (**Eq. 6**).

$$(1-x)ABO_3 + xAO + xB + xO_2 \leftrightarrow ABO_3 \qquad (\boldsymbol{Eq.6})$$

While the segregation of A site oxide is limited under the reducing condition due to the formation of stable stochiometric perovskite oxides, making the exsolution irreversible. (**Eq. 6**) Supported by the investigation conducted by Neagu et al, the Ni expelled from A-site deficient $La_{0.8}Ce_{0.1}Ni_{0.4}Ti_{0.6}O_3$ remained oxidized and socketed into the surface rather than dissolving back to the parent matrix after after testing in a CO oxidation reaction at 520 ℃ [94]. By varying the oxidation temperature, Jiang *et al.* observed that exsolved Ru from $La_{0.9}Fe_{0.92}Ru_{0.08-x}O_{3-\delta}$ was still on the surface but oxidized to RuO_2 at 400 ℃, achieving a high OER activity compared with the pristine oxides, mainly attributed to the formation of catalytically active RuO_2

component. Further increasing the oxidation temperature to 550 ℃ led to the disappearance of the exsolved particles [95].

1.3.3 surface tunability by acid etching

As mentioned above, the A-site elements consisting of alkaline, alkaline-earth, or lanthanide cations play a vital role in perovskite structure stability, but they are inert in most of the catalytic process. Upon annealing in an oxygen-enriched atmosphere, the A-O bond predominates on the topmost surface, and the subsequent segregation of A-site cations such as Sr^{2+}, Ba^{2+}, La^{3+}, and Pb^{2+} to the surface oxides of the perovskite sample is frequently reported in the literature [96]. Meanwhile, the ratio of the top-most layer of the perovskite which terminates with the A-O bond has been revealed to positively correlate with the calcination time [97].

For ABO_3 perovskite oxides, the bond length of A-O is greater than that of the B-O bond, corresponding to a higher bond energy, which theoretically opens the door to selectively removing A-site cations from the perovskite backbone. Multiple investigations have demonstrated that metal cations can be selectively removed from the framework following acid/base treatment, owing to their varying solubility in acidic or alkaline solutions [98]. Si *et al.* selectively removed La from three-dimensionally ordered perovskite by HNO_3 etching, forming the γ-MnO_2 which exhibited higher activity for CO oxidation compared to pristine $LaMnO_3$ and the normal γ-MnO_2 [99]. Adjusting the concentration of HNO_3 could partially preserve the perovskite structure, resulting in the formation of MnO_2/$LaMnO_3$ catalysts [100].

Another interesting example involves using $SrIrO_3$ thin film in the oxygen evolution reaction in the acidic condition. During the electrochemical testing, the IrO_x/$SrTiO_3$ gradually formed as the Sr leached from $SrTiO_3$ perovskite thin film, demonstrating improved catalytic performance and good stability [101]. In addition to exposing the active B site element, acid etching contributes also to the formation of a mesoporous structure with improved surface area due to A site element removal. Nong et. al prepared porous TiO_2 with a high specific surface area of 317 m^2/g by leaching K^+ from $K_2Ti_{18}O_{17}$ with formic acid under hydrothermal conditions [102]. When the B site is doped with Ru, the high surface area mesoporous $Ti_{1-x}Ru_xO_2$ mixed oxides could be derived [103]. In some cases, an excess of A-site elements beyond the stoichiometric ratio is intentionally added during the preparation process to introduce porosity. Research conducted by Wang *et al.* indicated that the porous $LaCoO_3$ could be achieved by the selective dissolution of the *in-situ* formed La_2O_3 particles from a pre-

synthesized $LaCoO_3$-La_2O_3 precursor, obtaining enhanced activity and water resistance during the ethyl acetate combustion [104].

However, the pristine crystal structure is inevitably destroyed by the acid etching in harsh conditions (high concentration of strong acid), giving rise to the thermal stability issue. In this scenario, a variety of weak acids such as citric acid, acetic acid, and tartaric acid are applied for the surface modulation of the perovskites while preserving their original structure. Treatment with 1 M acetic acid leaches the La-O termination in stoichiometric $LaCoO_3$, resulting in the dominance of Co-O termination on the perovskite oxide surface, thereby enhancing low-temperature catalytic performance for simultaneous NO and Hg^0 elimination. The Co-O termination could also be influenced by higher acetic acid concentrations [105]. Dissolution of the different A-site elements is sometimes affected by the etching time. An investigation demonstrated that short-time etching treatment on $La_{0.6}Sr_{0.4}Co_{0.2}Fe_{0.8}O_{3-\delta}$ could preferentially dissolve the Sr^{2+} in the A site due to its high solubility and the extended treatment time led to the further dissolution of La^{3+} [106]. Acid treatment on the perovskites could also introduce the secondary phase and alter the catalytic performance. Etching treatment on $La_3Mn_2O_7$ achieved by phosphoric acid removed the superficial La and yields the insoluble lanthanum phosphate on the surface, providing abundant Bronsted acid which facilitates the activation of the reactant molecular [107].

Acid etching, as a feasible surface modulation method, could also be applied in the bulk transition metal oxides. Co_3O_4 subjected to etching treatment with acetic acid showed a significant improvement in the propane combustion reaction, attributed to the formation of abundant defects, higher surface CO^{2+} content, and increased adsorbed oxygen content [108]. When used as the support for the precious metal, the abundant surface vacancies achieved by HF treatment on the acid-etched Co_3O_4 favor the high dispersity and thermal stability of RuO_x species, leading to outstanding vinyl chloride activity [109].

1.4 Motivation

The development of high-performance catalysts for the elimination of volatile organic compounds (VOCs) has become a crucial global priority to mitigate environmental pollution. One of the significant challenges in this field is the thermal stability of supported precious metal catalysts, which often limits their practical application. High-temperature exsolved nanoparticles have emerged as a promising solution to enhance the stability and activity of these catalysts due to the unique socketed structure and strong interactions between support and nanoparticles. However, the exsolution process of target precious metals can be accompanied by the segregation or co-exsolution of unwanted components, potentially altering the catalytic performance.

This thesis focuses on $LaFeO_3$ (LFO), a perovskite oxide known for its high tunability and stability. By partially substituting iron in LFO with ruthenium (resulting in $LaFe_{0.9}Ru_{0.1}O_3$, LFRO), I aim to fabricate thermally stable, socketed Ru nanoparticles (NPs) via an exsolution strategy. These Ru NPs are expected to exhibit high catalytic activity and good stability for the total oxidation of propane, serving as a model reaction for VOCs elimination. Despite the theoretical advantages, initial measurements showed that Ru-exsolved samples (LFRO_800R) exhibited substantially lower catalytic activity than expected. Advanced characterization techniques (including XRD, XPS, Raman, SEM, HRTEM, CO-DRIFTS, and EDS mappings) revealed that the exsolved particles formed a core-shell structure, where the active Ru alloyed with a slight amount of Fe is encapsulated by an inert LaOx coating layer. This coating layer can be selectively removed by oxidizing at 400 °C, which exposes the active Ru and significantly enhancing the catalytic activity for propane oxidation. The detailed information of this part could be found in **Chapter 2.1**.

The mechanism of the RuFe-LaO_x core-shell structured nanoparticle formation is the following question. In order to address these questions, a series of LFRO samples reduced at various temperatures ranging from 300°C to 800°C are prepared. Their catalytic activity and other structural and morphological properties are studied before and after reoxidation at 400°C. A variety of advanced experimental characterization methods are employed to track the surface evolution, the development of exsolved Ru particles, and the formation/removal of the passivating LaOx layer. These methods include *in-situ* TEM, *in-situ* XPS, *in-situ* DRIFTS, and notably, catalytic activity testing using propane combustion as the model reaction. Our findings reveal that the reduction of Ru in LFRO perovskites commences at 300 °C under reducing

conditions. The Ru exsolution is restricted to the near-surface zone at 500°C, while bulk exsolution and LaOx segregation start at 600°C. The detailed information could be seen in **Chapter 2.2**.

By providing valuable insights into the exsolution process and the dynamics of passivation layers, this thesis aims to enhance the practical application of catalysts and contribute to the broader field of environmental protection and sustainable technology development. Understanding the formation mechanism of the exsolved RuFe-LaO_x core-shell structure and its correlation with reduction temperature is critical for designing exsolution-based catalysts specially using perovskites as parent oxides for various applications.

1.5 Reference

1. Zhou, X.; Zhou, X.; Wang, C.; Zhou, H. Environmental and Human Health Impacts of Volatile Organic Compounds: A Perspective Review. *Chemosphere* **2023**, *313*, 137489, doi:10.1016/j.chemosphere.2022.137489
2. Manisalidis, I.; Stavropoulou, E.; Stavropoulos, A.; Bezirtzoglou, E. Environmental and Health Impacts of Air Pollution: A Review. *Front. Public Health* **2020**, *8*, 14, doi:10.3389/fpubh.2020.00014
3. Kamal, M.S.; Razzak, S.A.; Hossain, M.M. Catalytic Oxidation of Volatile Organic Compounds (VOCs) – A Review. *Atmos Environ.* **2016**, *140*, 117–134, doi:10.1016/j.atmosenv.2016.05.031
4. He, X.; Dong, F.; Han, W.; Tang, Z.; Ding, Y. Recent Advances and Future Challenges in the Catalytic Combustion of Light Hydrocarbon VOCs. *J. Mater. Chem. A* **2024**, *12*, 7470–7507, doi:10.1039/D3TA07590G
5. He, C.; Cheng, J.; Zhang, X.; Douthwaite, M.; Pattisson, S.; Hao, Z. Recent Advances in the Catalytic Oxidation of Volatile Organic Compounds: A Review Based on Pollutant Sorts and Sources. *Chem Rev.* **2019**, *119*, 4471–4568, doi:10.1021/acs.chemrev.8b00408
6. Liotta, L.F. Catalytic Oxidation of Volatile Organic Compounds on Supported Noble Metals. *Appl. Catal. B* **2010**, *100*, 403–412, doi:10.1016/j.apcatb.2010.08.023
7. Gao, X.; Bai, Y.; Zhang, H.; Wang, X. Catalytic Oxidation of N-Decane, n-Hexane, and Propane over Pt/CeO_2 Catalysts. *ACS Omega* **2023**, *8*, 6791–6800, doi:10.1021/acsomega.2c07399
8. Huang, Z.; Ding, J.; Yang, X.; Liu, H.; Song, P.; Guo, Y.; Guo, Y.; Wang, L.; Zhan, W. Highly Efficient Oxidation of Propane at Low Temperature over a Pt-Based Catalyst by Optimization Support. *Environ. Sci. Technol.* **2022**, *56*, 17278–17287, doi:10.1021/acs.est.2c05599
9. Toso, A.; Colussi, S.; Padigapaty, S.; de Leitenburg, C.; Trovarelli, A. High Stability and Activity of Solution Combustion Synthesized Pd-Based Catalysts for Methane Combustion in Presence of Water. *Appl. Catal., B* **2018**, *230*, 237–245, doi:10.1016/j.apcatb.2018.02.049
10. Mkhwanazi, T.P.O.; Farahani, M.D.; Mahomed, A.S.; Singh, S.; Friedrich, H.B. Engineering of Catalytic Sites of $Pd_xCe_{1-x}O_{2-\delta}$ for Dehydrogenation, Oxygen Insertion and Reverse Water Gas Shift Reactions during Methane Combustion. *Appl. Catal., B* **2020**, *275*, 119118, doi:10.1016/j.apcatb.2020.119118
11. Johnson Matthey. *PGM management*. https://matthey.com/products-and-markets/pgms-and-circularity/pgm-management (accessed 2024-5-31)
12. Okal, J.; Zawadzki, M. Influence of Catalyst Pretreatments on Propane Oxidation over $Ru/\gamma\text{-}Al_2O_3$. *Catal. Letters* **2009**, *132*, 225–234, doi:10.1007/s10562-009-0100-2

13. Okal, J.; Zawadzki, M. Combustion of Propane over Novel Zinc Aluminate-Supported Ruthenium Catalysts. *Appl. Catal., B* **2011**, *105*, 182–190, doi:10.1016/j.apcatb.2011.04.013

14. Okal, J.; Zawadzki, M.; Krajczyk, L. Light Alkane Oxidation over Ru Supported on ZnAl2O4, CeO_2 and Al_2O_3. *Catal. Today* **2011**, *176*, 173– 176, doi:10.1016/j.cattod.2010.11.096

15. Baranowska, K.; Okal, J. Bimetallic Ru-Re/γ-Al_2O_3 Catalysts for the Catalytic Combustion of Propane: Effect of the Re Addition. *Appl. Catal., A Gen* **2015**, *499*, 158–167, doi:10.1016/j.apcata.2015.04.023

16. Ledwa, K.A.; Kępiński, L.; Ptak, M.; Szukiewicz, R. $Ru_{0.05}Ce_{0.95}O_{2-y}$ Deposited on Functionalized Alumina as a Smart Catalyst for Propane Oxidation. *Appl. Catal., B* **2020**, *274*, 119090, doi:10.1016/j.apcatb.2020.119090

17. Ledwa, K.A.; Pawlyta, M.; Kępiński, L. $Ru_xCe_{1-x}O_{2-y}$ Nanoparticles Deposited on Functionalized γ-Al_2O_3 as a Thermally Stable Oxidation Catalyst. *Appl. Catal., B* **2018**, *230*, 135–144, doi:10.1016/j.apcatb.2018.02.037.

18. Liu, W.; Yang, S.; Zhang, Q.; He, T.; Luo, Y.; Tao, J.; Wu, D.; Peng, H. Insights into Flower like Al_2O_3 Spheres with Rich Unsaturated Pentacoordinate Al^{3+} Sites Stabilizing Ru-CeO_x for Propane Total Oxidation. *Appl. Catal., B* **2021**, *292*, 120171, doi:10.1016/j.apcatb.2021.120171

19. Hu, Z.; Wang, Z.; Guo, Y.; Wang, L.; Guo, Y.; Zhang, J.; Zhan, W. Total Oxidation of Propane over a Ru/CeO_2 Catalyst at Low Temperature. *Environ. Sci. Technol.* **2018**, *52*, 9531–9541, doi:10.1021/acs.est.8b03448

20. Wang, Z.; Huang, Z.; Brosnahan, J.T.; Zhang, S.; Guo, Y.; Guo, Y.; Wang, L.; Wang, Y.; Zhan, W. Ru/CeO2 Catalyst with Optimized CeO_2 Support Morphology and Surface Facets for Propane Combustion. *Environ. Sci. Technol.* **2019**, *53*, 5349–5358, doi:10.1021/acs.est.9b01929

21. Wu, J.; Chen, B.; Yan, J.; Zheng, X.; Wang, X.; Deng, W.; Dai, Q. Ultra-Active Ru Supported on CeO_2 Nanosheets for Catalytic Combustion of Propane: Experimental Insights into Interfacial Active Sites. *Chem. Eng. J.* **2022**, *438*, 135501, doi:10.1016/j.cej.2022.135501

22. Sun, Y.; Ye, F.; Ding, J.; Li, J.; Guo, Y.; Wang, L.; Guo, Y.; Dai, S.; Zhan, W. Regulating the Spatial Distribution of Ru Nanoparticles on CeO_2 Support for Enhanced Propane Oxidation. *ACS Appl. Nano Mater.* **2022**, *5*, 3937–3945, doi:10.1021/acsanm.1c04526

23. Wang, W.; Timmer, P.; Luciano, A.S.; Wang, Y.; Weber, T.; Glatthaar, L.; Guo, Y.; Smarsly, B.M.; Over, H. Inserted Hydrogen Promotes Oxidation Catalysis of Mixed $Ru_{0.3}Ti_{0.7}O_2$ as Exemplified with Total Propane Oxidation and the HCl Oxidation Reaction. *Catal. Sci. Technol.* **2023**, *13*, 1395–1408, doi:10.1039/d2cy02000a

24. Wang, W.; Wang, Y.; Timmer, P.; Spriewald-Luciano, A.; Weber, T.; Glatthaar, L.; Guo, Y.; Smarsly, B.M.; Over, H. Hydrogen Incorporation in $Ru_xTi_{1-x}O_2$ Mixed Oxides

Promotes Total Oxidation of Propane. *Inorganics* **2023**, *11*, 330, doi:10.3390/inorganics11080330

25. Debecker, D.P.; Farin, B.; Gaigneaux, E.M.; Sanchez, C.; Sassoye, C. Total Oxidation of Propane with a Nano-RuO_2/TiO_2 Catalyst. *Appl. Catal., A Gen.* **2014**, *481*, 11–18, doi:10.1016/j.apcata.2014.04.043

26. Wang, M.; Li, G.; Wang, S.; Liu, X.; Wang, A.; Cao, H.; Zhang, C. Catalytic Oxidation of Propane over Nanorod-like TiO_2 Supported Ru Catalysts: Structure-Activity Dependence and Mechanistic Insights. *Chem. Eng. J.* **2024**, *481*, 148344, doi:10.1016/j.cej.2023.148344

27. Camposeco, R.; Miguel, O.; Torres, A.E.; Armas, D.E.; Zanella, R. Highly Active Ru/TiO_2 Nanostructures for Total Catalytic Oxidation of Propane. *Environ. Sci. Pollut. R.* **2023**, *30*, 98076–98090, doi:10.1007/s11356-023-29153-w

28. Wang, Z.; Khalid, O.; Wang, W.; Wang, Y.; Weber, T.; Spriewald Luciano, A.; Zhan, W.; Smarsly, B.M.; Over, H. Comparison Study of the Effect of CeO_2-Based Carrier Materials on the Total Oxidation of CO, Methane, and Propane over RuO_2. *Catal. Sci. Technol.* **2021**, *11*, 6839–6853, doi:10.1039/d1cy01277k

29. Sastre, G.; Corma, A. The Confinement Effect in Zeolites. *J. Mol. Catal. A Chem.* **2009**, *305*, 3–7, doi:10.1016/j.molcata.2008.10.042

30. Leung, K.C.; Tan, E.; Li, G.; Ng, B.K.Y.; Ho, P.L.; Lebedev, K.; Tsang, S.C.E. Metal-Loaded Zeolites in Ammonia Decomposition Catalysis. *Farad. Disc.* **2023**, *243*, 520–548, doi:10.1039/d2fd00175f

31. Wang, L.; Wang, L.; Meng, X.; Xiao, F.-S. New strategies for the preparation of sinter-resistant metal-nanoparticle-based catalysts. *Adv. Mater.* **2019**, *31*, 1901905, doi:10.1002/adma.201901905

32. Li, Y.; Yao, L.; Song, Y.; Liu, S.; Zhao, J.; Ji, W.; Au, C.T. Core-Shell Structured Microcapsular-like Ru@SiO_2 Reactor for Efficient Generation of COx-Free Hydrogen through Ammonia Decomposition. *Chem. Commun.,* **2010**, *46*, 5298–5300, doi:10.1039/c0cc00430h

33. Sun, Q.; Wang, N.; Yu, J. Advances in Catalytic Applications of Zeolite-Supported Metal Catalysts. *Adv. Mater.* 2021, *33*. 2104442, doi:10.1002/adma.202104442

34. Liu, Y.; Li, Z.; Yu, Q.; Chen, Y.; Chai, Z.; Zhao, G.; Liu, S.; Cheong, W.C.; Pan, Y.; Zhang, Q.; et al. A General Strategy for Fabricating Isolated Single Metal Atomic Site Catalysts in Y Zeolite. *J. Am. Chem. Soc.* **2019**, *141*, 9305–9311, doi:10.1021/jacs.9b02936

35. Tao, J.; Zhang, Q.; Zhao, Y.; Chen, H.; Liu, W.; He, Y.; Yin, Y.; He, T.; Chen, J.; Wang, X.; et al. Elucidating the Role of Confinement and Shielding Effect over Zeolite Enveloped Ru Catalysts for Propane Low Temperature Degradation. *Chemosphere* **2022**, *302*, 134884 doi:10.1016/j.chemosphere.2022.134884

36. Zheng, Y.; Han, R.; Wang, Y.; Xu, W.; Liu, Q. High-Temperature Shock-Resistant Zeolite-Confined Ru Subnanometric Species Boosts Highly Catalytic Oxidation of Dichloromethane. *Appl. Catal., B* **2024**, *355*, doi:10.1016/j.apcatb.2024.124195

37. Hansen, T.W.; Delariva, A.T.; Challa, S.R.; Datye, A.K. Sintering of Catalytic Nanoparticles: Particle Migration or Ostwald Ripening? *Acc. Chem. Res.* **2013**, *46*, 1720–1730, doi:10.1021/ar3002427

38. De Rogatis, L.; Cargnello, M.; Gombac, V.; Lorenzut, B.; Montini, T.; Fornasiero, P. Embedded Phases: A Way to Active and Stable Catalysts. *ChemSusChem* 2010, *3*, 24–42, doi:10.1002/cssc.200900151

39. Cimino, A.; Stone, F.S. Oxide Solid Solution as Catalysts. *Adv. Catal.* **2002**, *47*, 141–306, doi:10.1016/S0360-0564(02)47007-1

40. Kumar, A.; Kumar, A.; Krishnan, V. Perovskite Oxide Based Materials for Energy and Environment-Oriented Photocatalysis. *ACS Catal.* **2020**, *10*, 10253–10315, doi:10.1021/acscatal.0c02947

41. Ubic, R.; Tolman, K.; Talley, K.; Joshi, B.; Schmidt, J.; Faulkner, E.; Owens, J.; Papac, M.; Garland, A.; Rumrill, C.; et al. Lattice-Constant Prediction and Effect of Vacancies in Aliovalently Doped Perovskites. *J. Alloys Compd.* **2015**, *644*, 982–995, doi:10.1016/j.jallcom.2015.04.213

42. Kim, Y.H.; Jeong, H.; Won, B.R.; Jeon, H.; Park, C. ho; Park, D.; Kim, Y.; Lee, S.; Myung, J. ha Nanoparticle Exsolution on Perovskite Oxides: Insights into Mechanism, Characteristics and Novel Strategies. *Nano-Micro Lett.* **2024**, *16*, 33, doi:10.1007/s40820-023-01258-4

43. Tang, C.; Kousi, K.; Neagu, D.; Metcalfe, I.S. Trends and Prospects of Bimetallic Exsolution. *Chem. Eur. J.* **2021**, *27*, 6666–6675, doi:10.1002/chem.202004950

44. Neagu, D.; Tsekouras, G.; Miller, D.N.; Ménard, H.; Irvine, J.T.S. In Situ Growth of Nanoparticles through Control of Non-Stoichiometry. *Nat. Chem.* **2013**, *5*, 916–923, doi:10.1038/nchem.1773

45. Liu, C.Y.; Bard, A.J. Pressure-Induced Insulator-Conductor Transition in a Photoconducting Organic Liquid-Crystal Film. *Nature* **2002**, *418*, 162–164, doi:10.1038/nature00875

46. Hamada, I.; Uozumi, A.; Morikawa, Y.; Yanase, A.; Katayama-Yoshida, H. A Density Functional Theory Study of Self-Regenerating Catalysts $LaFe_{1-x}MxO_{3-y}$ (M = Pd, Rh, Pt). *J. Am. Chem. Soc.* **2011**, *133*, 18506–18509, doi:10.1021/ja110302t

47. Ozkan, S.; Kim, S.J.; Miller, D.N.; Irvine, J.T.S. A New Approach to Fuel Cell Electrodes: Lanthanum Aluminate Yielding Fine Pt Nanoparticle Exsolution for Oxygen Reduction Reaction. *Adv. Energy Mater.* **2024**, *14*, 2303025 doi:10.1002/aenm.202303025

48. Gao, Y.; Chen, D.; Saccoccio, M.; Lu, Z.; Ciucci, F. From Material Design to Mechanism Study: Nanoscale Ni Exsolution on a Highly Active A-Site Deficient Anode Material for

Solid Oxide Fuel Cells. *Nano Energy* **2016**, *27*, 499–508, doi:10.1016/j.nanoen.2016.07.013

49. Han, H.; Xing, Y.; Park, B.; Bazhanov, D.I.; Jin, Y.; Irvine, J.T.S.; Lee, J.; Oh, S.H. Anti-Phase Boundary Accelerated Exsolution of Nanoparticles in Non-Stoichiometric Perovskite Thin Films. *Nat. Commun.* **2022**, *13*, 6682, oi:10.1038/s41467-022-34289-3

50. Jo, Y.R.; Koo, B.; Seo, M.J.; Kim, J.K.; Lee, S.; Kim, K.; Han, J.W.; Jung, W.C.; Kim, B.J. Growth Kinetics of Individual Co Particles Ex-Solved on $SrTi_{0.75}Co_{0.25}O_{3-\delta}$ Polycrystalline Perovskite Thin Films. *J. Am. Chem. Soc.* **2019**, *141*, 6690–6697, doi:10.1021/jacs.9b01882

51. Wang, J.; Yang, J.; Opitz, A.K.; Bowman, W.; Bliem, R.; Dimitrakopoulos, G.; Nenning, A.; Waluyo, I.; Hunt, A.; Gallet, J.J.; et al. Tuning Point Defects by Elastic Strain Modulates Nanoparticle Exsolution on Perovskite Oxides. *Chem. Mater.* **2021**, *33*, 5021–5034, doi:10.1021/acs.chemmater.1c00821

52. Wang, J.; Kalaev, D.; Yang, J.; Waluyo, I.; Hunt, A.; Sadowski, J.T.; Tuller, H.L.; Yildiz, B. Fast Surface Oxygen Release Kinetics Accelerate Nanoparticle Exsolution in Perovskite Oxides. *J. Am. Chem. Soc.* **2023**, *145*, 1714–1727, doi:10.1021/jacs.2c10256

53. Kwon, O.; Joo, S.; Choi, S.; Sengodan, S.; Kim, G. Review on Exsolution and Its Driving Forces in Perovskites. *J. Phys. Energy* **2020**, *2*. 032001, doi:10.1088/2515-7655/ab8c1f

54. Joo, S.; Kwon, O.; Kim, K.; Kim, S.; Kim, H.; Shin, J.; Jeong, H.Y.; Sengodan, S.; Han, J.W.; Kim, G. Cation-Swapped Homogeneous Nanoparticles in Perovskite Oxides for High Power Density. *Nat. Commun.* **2019**, *10*, 697, doi:10.1038/s41467-019-08624-0

55. Tang, C.; Kousi, K.; Neagu, D.; Portolés, J.; Papaioannou, E.I.; Metcalfe, I.S. Towards Efficient Use of Noble Metals: Via Exsolution Exemplified for CO Oxidation. *Nanoscale* **2019**, *11*, 16935–16944, doi:10.1039/c9nr05617c

56. Kim, J.K.; Jo, Y.R.; Kim, S.; Koo, B.; Kim, J.H.; Kim, B.J.; Jung, W.C. Exceptional Tunability over Size and Density of Spontaneously Formed Nanoparticles via Nucleation Dynamics. *ACS Appl. Mater. Interfaces* **2020**, *12*, 24039–24047, doi:10.1021/acsami.0c05215

57. O'Leary, W.; Giordano, L.; Rupp, J.L.M. Tuning Reduction Conditions to Understand and Control Ni Exsolution from $Sr_{0.8}La_{0.1}Ca_{0.1}Ti_{0.94}Ni_{0.06}O_{3-\delta}$. *J. Mater. Chem. A* **2023**, *11*, 21429–21442, doi:10.1039/d3ta04817a

58. Neagu, D.; Kyriakou, V.; Roiban, I.L.; Aouine, M.; Tang, C.; Caravaca, A.; Kousi, K.; Schreur-Piet, I.; Metcalfe, I.S.; Vernoux, P.; et al. In Situ Observation of Nanoparticle Exsolution from Perovskite Oxides: From Atomic Scale Mechanistic Insight to Nanostructure Tailoring. *ACS Nano* **2019**, *13*, 12996–13005, doi:10.1021/acsnano.9b05652

59. Thalinger, R.; Gocyla, M.; Heggen, M.; Klötzer, B.; Penner, S. Exsolution of Fe and SrO Nanorods and Nanoparticles from Lanthanum Strontium Ferrite $La_{0.6}Sr_{0.4}FeO_{3-\delta}$ Materials

by Hydrogen Reduction. *J. Phys. Chem. C* **2015**, *119*, 22050–22056, doi:10.1021/acs.jpcc.5b06014

60. Chen, M.; Xu, Y.; Zhang, Y.; Zhang, Z.; Li, X.; Wang, Q.; Huang, M.; Fang, W.; Zhang, Y.; Jiang, H.; et al. Promoting CO_2 Electroreduction Over Nano-Socketed Cu/Perovskite Heterostructures via A-Site-Valence-Controlled Oxygen Vacancies. *Small* **2024**, 2400615, doi:10.1002/smll.202400615

61. Qiu, Y.P.; Shi, Q.; Wang, W.Z.; Xia, S.H.; Dai, H.; Yin, H.; Yang, Z.Q.; Wang, P. Facile Synthesis of Highly Dispersed and Well-Alloyed Bimetallic Nanoparticles on Oxide Support. *Small* **2022**, *18*, 2106143, doi:10.1002/smll.202106143

62. Jiang, Y.; Geng, Z.; Sun, Y.; Wang, X.; Huang, K.; Cong, Y.; Shi, F.; Wang, Y.; Zhang, W.; Feng, S. Highly Efficient B-Site Exsolution Assisted by Co Doping in Lanthanum Ferrite toward High-Performance Electrocatalysts for Oxygen Evolution and Oxygen Reduction. *ACS Sustainable Chem. Eng.* **2020**, *8*, 302–310, doi:10.1021/acssuschemeng.9b05344

63. Liang, Y.; Cui, Y.; Chao, Y.; Han, N.; Sunarso, J.; Liang, P.; He, X.; Zhang, C.; Liu, S. Exsolution of CoFe(Ru) Nanoparticles in Ru-Doped $(La_{0.8}Sr_{0.2})_{0.9}Co_{0.1}Fe_{0.8}Ru_{0.1}O_{3-\delta}$ for Efficient Oxygen Evolution Reaction. *Nano Res.* **2022**, *15*, 6977–6986, doi:10.1007/s12274022-4328-0

64. Papargyriou, D.; Miller, D.N.; Irvine, J.T.S. Exsolution of Fe-Ni Alloy Nanoparticles from (La,Sr)(Cr,Fe,Ni)O_3 Perovskites as Potential Oxygen Transport Membrane Catalysts for Methane Reforming. *J. Mater. Chem. A* **2019**, *7*, 15812–15822, doi:10.1039/c9ta03711j

65. Wang, Z.; Tan, T.; Du, K.; Zhang, Q.; Liu, M.; Yang, C. A High-Entropy Layered Perovskite Coated with In Situ Exsolved Core-Shell CuFe@FeO_x Nanoparticles for Efficient CO_2 Electrolysis. *Adv. Mater.* **2024**, *36*, 2312119, doi:10.1002/adma.202312119.

66. Tan, T.; Wang, Z.; Qin, M.; Zhong, W.; Hu, J.; Yang, C.; Liu, M. In Situ Exsolution of Core-Shell Structured NiFe/FeOx Nanoparticles on $Pr_{0.4}Sr_{1.6}(NiFe)_{1.5}Mo_{0.5}O_{6-\delta}$ for CO_2 Electrolysis. *Adv. Funct. Mater.* **2022**, *32*, 202202878, doi:10.1002/adfm.202202878

67. Buharon, M.; Singh, S.; Komarala, E.P.; Rosen, B.A. Expanding Possibilities for Solid-Phase Crystallization by Exsolving Tunable Pd-NiO Core-Shell Nanostructures. *CrystEngComm* **2018**, *20*, 6372–6376, doi:10.1039/c8ce01294f

68. Neagu, D.; Oh, T.S.; Miller, D.N.; Ménard, H.; Bukhari, S.M.; Gamble, S.R.; Gorte, R.J.; Vohs, J.M.; Irvine, J.T.S. Nano-Socketed Nickel Particles with Enhanced Coking Resistance Grown in Situ by Redox Exsolution. *Nat. Commun.* **2015**, *6*, 8120, doi:10.1038/ncomms9120

69. Gao, Y.; Lu, Z.; You, T.L.; Wang, J.; Xie, L.; He, J.; Ciucci, F. Energetics of Nanoparticle Exsolution from Perovskite Oxides. *J. Phys. Chem. Lett.* **2018**, *9*, 3772–3778, doi:10.1021/acs.jpclett.8b01380

70. Kim, K.J.; Han, H.; Defferriere, T.; Yoon, D.; Na, S.; Kim, S.J.; Dayaghi, A.M.; Son, J.; Oh, T.S.; Jang, H.M.; et al. Facet-Dependent in Situ Growth of Nanoparticles in Epitaxial

Thin Films: The Role of Interfacial Energy. *J. Am. Chem. Soc.* **2019**, *141*, 7509–7517, doi:10.1021/jacs.9b02283.

71. Cai, Z.; Kuru, Y.; Han, J.W.; Chen, Y.; Yildiz, B. Surface Electronic Structure Transitions at High Temperature on Perovskite Oxides: The Case of Strained $La_{0.8}Sr_{0.2}CoO_3$ Thin Films. *J. Am. Chem. Soc.* **2011**, *133*, 17696–17704, doi:10.1021/ja2059445

72. Kushima, A.; Yildiz, B. Oxygen Ion Diffusivity in Strained Yttria Stabilized Zirconia: Where Is the Fastest Strain? *J. Mater. Chem.* **2010**, *20*, 4809–4819, doi:10.1039/c000259c.

73. Han, H.; Park, J.; Nam, S.Y.; Kim, K.J.; Choi, G.M.; Parkin, S.S.P.; Jang, H.M.; Irvine, J.T.S. Lattice Strain-Enhanced Exsolution of Nanoparticles in Thin Films. *Nat. Commun.* **2019**, *10*, 1471, doi:10.1038/s41467-019-09395-4

74. Oh, T.S.; Rahani, E.K.; Neagu, D.; Irvine, J.T.S.; Shenoy, V.B.; Gorte, R.J.; Vohs, J.M. Evidence and Model for Strain-Driven Release of Metal Nanocatalysts from Perovskites during Exsolution. *J. Phys. Chem. Lett.* **2015**, *6*, 5106–5110, doi:10.1021/acs.jpclett.5b02292

75. Yang, Y.; Li, J.; Sun, Y. The Metal/Oxide Heterointerface Delivered by Solid-Based Exsolution Strategy: A Review. *Chem. Eng. J.* **2022**, *440*, 135868, doi:10.1016/j.cej.2022.135868

76. Fu, C.J.; Ma, Q.; Gao, L.; Li, S. Recent Advances in Perovskite Oxides Electrocatalysts: Ordered Perovskites, Cations Segregation and Exsolution. *ChemCatChem* **2023**, *15*, e202300389, doi:10.1002/cctc.202300389

77. Khalid, H.; Haq, A. ul; Alessi, B.; Wu, J.; Savaniu, C.D.; Kousi, K.; Metcalfe, I.S.; Parker, S.C.; Irvine, J.T.S.; Maguire, P.; et al. Rapid Plasma Exsolution from an A-Site Deficient Perovskite Oxide at Room Temperature. *Adv. Energy Mater.* **2022**, *12*, 202201131, doi:10.1002/aenm.202201131

78. Sun, Z.; Fan, W.; Lin, T. Rapidly Tuning the Electrocatalytic Activity of Perovskite Oxides by Plasma Treatment. *J. Mater. Chem. A* **2023**, *11*, 24982–24990, doi:10.1039/d3ta05214a

79. Myung, J.H.; Neagu, D.; Miller, D.N.; Irvine, J.T.S. Switching on Electrocatalytic Activity in Solid Oxide Cells. *Nature* **2016**, *537*, 528–531, doi:10.1038/nature19090.

80. Jo, S.; Jeong, H.G.; Kim, Y.H.; Neagu, D.; Myung, J. ha Stability and Activity Controls of Cu Nanoparticles for High-Performance Solid Oxide Fuel Cells. *Appl. Catal., B* **2021**, *285*, 119828, doi:10.1016/j.apcatb.2020.119828

81. Kim, Y.H.; Jeong, H.; Won, B.R.; Myung, J. ha Exsolution Modeling and Control to Improve the Catalytic Activity of Nanostructured Electrodes. *Adv. Mater.* **2023**, *35*, 2208984, doi:10.1002/adma.202208984

82. Naeem, M.A.; Abdala, P.M.; Armutlulu, A.; Kim, S.M.; Fedorov, A.; Müller, C.R. Exsolution of Metallic Ru Nanoparticles from Defective, Fluorite-Type Solid Solutions

$Sm_2Ru_xCe_{2-x}O_7$ to Impart Stability on Dry Reforming Catalysts. *ACS Catal.* **2020**, *10*, 1923–1937, doi:10.1021/acscatal.9b04555

83. Neagu, D.; Kyriakou, V.; Roiban, I. L.; Aouine, M.; Tang, C.; Caravaca, A.; Kousi, K.; Schreur-Piet, I.; Metcalfe, I. S.; Vernoux, P.; Van De Sanden, M. C. M.; Tsampas, M. N. In Situ Observation of Nanoparticle Exsolution from Perovskite Oxides: From Atomic Scale Mechanistic Insight to Nanostructure Tailoring. *ACS Nano* **2019**, *13*, 12996–13005, doi:10.1021/acsnano.9b05652

84. Liu, S.; Liu, Q.; Luo, J.L. Highly Stable and Efficient Catalyst with in Situ Exsolved Fe-Ni Alloy Nanospheres Socketed on an Oxygen Deficient Perovskite for Direct CO_2 Electrolysis. *ACS Catal.* **2016**, *6*, 6219–6228, doi:10.1021/acscatal.6b01555

85. Wang, Y.; Lei, X.; Zhang, Y.; Chen, F.; Liu, T. In-Situ Growth of Metallic Nanoparticles on Perovskite Parent as a Hydrogen Electrode for Solid Oxide Cells. *J. Power Sources* **2018**, *405*, 114–123, doi:10.1016/j.jpowsour.2018.10.023

86. Liu, C.Y.; Bard, A.J. Pressure-Induced Insulator-Conductor Transition in a Photoconducting Organic Liquid-Crystal Film. *Nature* **2002**, *418*, 162–164, doi:10.1038/nature00875

87. Tanaka, H. An Intelligent Catalyst: The Self-Regenerative Palladium-Perovskite Catalyst for Automotive Emissions Control. *Catal. Surv. Asia* **2005,** *9*, 63–74, doi:10.1007/s10563-005-5992-2

88. Nishihata, Y.; Mizuki, J.; Tanaka, H.; Uenishi, M.; Kimura, M. Self-Regeneration of Palladium-Perovskite Catalysts in Modern Automobiles. *J. Phys. Chem. Solids* **2005**, *66*, 274–282, doi:10.1016/j.jpcs.2004.06.090

89. Steiger, P.; Delmelle, R.; Foppiano, D.; Holzer, L.; Heel, A.; Nachtegaal, M.; Kröcher, O.; Ferri, D. Structural Reversibility and Nickel Particle Stability in Lanthanum Iron Nickel Perovskite-Type Catalysts. *ChemSusChem* **2017**, *10*, 2505–2517, doi:10.1002/cssc.201700358

90. Lai, K.Y.; Manthiram, A. Self-Regenerating Co-Fe Nanoparticles on Perovskite Oxides as a Hydrocarbon Fuel Oxidation Catalyst in Solid Oxide Fuel Cells. *Chem. Mater.* **2018**, *30*, 2515–2525, doi:10.1021/acs.chemmater.7b04569

91. Lv, H.; Lin, L.; Zhang, X.; Li, R.; Song, Y.; Matsumoto, H.; Ta, N.; Zeng, C.; Fu, Q.; Wang, G.; et al. Promoting Exsolution of RuFe Alloy Nanoparticles on $Sr_2Fe_{1.4}Ru_{0.1}Mo_{0.5}O_{6-\delta}$ via Repeated Redox Manipulations for CO_2 Electrolysis. *Nat. Commun.* **2021**, *12*, 5665, doi:10.1038/s41467-021-26001-8

92. Katz, M.B.; Graham, G.W.; Duan, Y.; Liu, H.; Adamo, C.; Schlom, D.G.; Pan, X. Self-Regeneration of Pd-$LaFeO_3$ Catalysts: New Insight from Atomic-Resolution Electron Microscopy. *J. Am. Chem. Soc.* **2011**, *133*, 18090–18093, doi:10.1021/ja2082284

93. Katz, M.B.; Zhang, S.; Duan, Y.; Wang, H.; Fang, M.; Zhang, K.; Li, B.; Graham, G.W.; Pan, X. Reversible Precipitation/Dissolution of Precious-Metal Clusters in Perovskite-

Based Catalyst Materials: Bulk versus Surface Re-Dispersion. *J. Catal.* **2012**, *293*, 145–148, doi:10.1016/j.jcat.2012.06.017

94. Neagu, D.; Papaioannou, E.I.; Ramli, W.K.W.; Miller, D.N.; Murdoch, B.J.; Ménard, H.; Umar, A.; Barlow, A.J.; Cumpson, P.J.; Irvine, J.T.S.; et al. Demonstration of Chemistry at a Point through Restructuring and Catalytic Activation at Anchored Nanoparticles. *Nat. Commun.* **2017**, *8*, 1855, doi:10.1038/s41467-017-01880-y

95. Jiang, Y.; Geng, Z.; Yuan, L.; Sun, Y.; Cong, Y.; Huang, K.; Wang, L.; Zhang, W. Nanoscale Architecture of $RuO_2/La_{0.9}Fe_{0.92}Ru_{0.08-x}O_{3-\delta}$ Composite via Manipulating the Exsolution of Low Ru-Substituted A-Site Deficient Perovskite. *ACS Sustain. Chem. Eng.* **2018**, *6*, 11999–12005, doi:10.1021/acssuschemeng.8b02288

96. Koo, B.; Kim, K.; Kim, J.K.; Kwon, H.; Han, J.W.; Jung, W.C. Sr Segregation in Perovskite Oxides: Why It Happens and How It Exists. *Joule* 2018, *2*, 1476–1499. doi:10.1016/j.joule.2018.07.016

97. Bachelet, R.; Sánchez, F.; Palomares, F.J.; Ocal, C.; Fontcuberta, J. Atomically Flat SrO-Terminated $SrTiO_3$ (001) Substrate. *Appl. Phys. Lett.* **2009**, *95*, 14915, doi:10.1063/1.3240869

98. Yang, B.; Zhao, Y.; Fang, L. Effects of Acid Etching on the Structure of PtNi Catalyst and Total Exposed Active Sites. *Surf. Interface Anal.* **2020**, *52*, 573–583, doi:10.1002/sia.6787

99. Si, W.; Wang, Y.; Peng, Y.; Li, J. Selective Dissolution of A-Site Cations in ABO_3 Perovskites: A New Path to High-Performance Catalysts. *Angew. Chem. Int. Ed.* **2015**, *54*, 7954–7957, doi:10.1002/anie.201502632

100. Si, W.; Wang, Y.; Zhao, S.; Hu, F.; Li, J. A Facile Method for in Situ Preparation of the $MnO_2/LaMnO_3$ Catalyst for the Removal of Toluene. *Environ. Sci. Technol.* **2016**, *50*, 4572–4578, doi:10.1021/acs.est.5b06255

101. Seitz, L.C.; Dickens, C.F.; Nishio, K.; Hikita, Y.; Montoya, J.; Doyle, A.; Kirk, C.; Vojvodic, A.; Hwang, H.Y.; Norskov, J.K.; et al. A Highly Active and Stable $IrOx/SrIrO_3$ Catalyst for the Oxygen Evolution Reaction. *Science*, **2016**, *353*, 1011 – 1014, doi:10.1126/science.aaf5050

102. Nong, S.; Dong, C.; Wang, Y.; Huang, F. Constructing Porous TiO_2 crystals by an Etching Process for Long-Life Lithium-Ion Batteries. *Nanoscale* **2020**, *12*, 18429–18436, doi:10.1039/d0nr04861e

103. Nong, S.; Dong, W.; Yin, J.; Dong, B.; Lu, Y.; Yuan, X.; Wang, X.; Bu, K.; Chen, M.; Jiang, S.; et al. Well-Dispersed Ruthenium in Mesoporous Crystal TiO_2 as an Advanced Electrocatalyst for Hydrogen Evolution Reaction. *J. Am. Chem. Soc.* **2018**, *140*, 5719–5727, doi:10.1021/jacs.7b13736

104. Wang, S.; Zhu, J.; Carabineiro, S.A.C.; Xiao, P.; Zhu, Y. Selective Etching of In-Situ Formed La_2O_3 Particles to Prepare Porous $LaCoO_3$ Perovskite for Catalytic Combustion of Ethyl Acetate. *Appl. Catal., A Gen* **2022**, *635*, doi:10.1016/j.apcata.2022.118554

105. Ao, R.; Ma, L.; Dai, Q.; Guo, Z.; Liu, H.; Li, W. Promotional Effect of Acetic Acid on Simultaneous NO and Hg^0 Oxidation over $LaCoO_3$ Perovskite. *Int. J. Hydrog. Energy* **2022**, *47*, 3741–3751, doi:10.1016/j.ijhydene.2021.10.264

106. Zong, R.Q.; Fang, Y.G.; Zhu, C.; Zhang, X.; Wu, L.; Hou, X.; Tao, Y.K.; Shao, J. Surface Defect Engineering on Perovskite Oxides as Efficient Bifunctional Electrocatalysts for Water Splitting. *ACS Appl. Mater. Interfaces* **2021**, *13*, 42852–42860, doi:10.1021/acsami.1c11895

107. Weng, X.; Meng, Q.; Liu, J.; Jiang, W.; Pattisson, S.; Wu, Z. Catalytic Oxidation of Chlorinated Organics over Lanthanide Perovskites: Effects of Phosphoric Acid Etching and Water Vapor on Chlorine Desorption Behavior. *Environ. Sci. Technol* **2019**, *53*, 884–893, doi:10.1021/acs.est.8b04582

108. Tang, W.; Xiao, W.; Wang, S.; Ren, Z.; Ding, J.; Gao, P.X. Boosting Catalytic Propane Oxidation over PGM-Free Co_3O_4 Nanocrystal Aggregates through Chemical Leaching: A Comparative Study with Pt and Pd Based Catalysts. *Appl. Catal., B* **2018**, *226*, 585–595, doi:10.1016/j.apcatb.2017.12.075

109. Liu, H.; Yang, J.; Jia, Y.; Wang, Z.; Jiang, M.; Shen, K.; Zhao, H.; Guo, Y.; Guo, Y.; Wang, L.; et al. Significant Improvement of Catalytic Performance for Chlorinated Volatile Organic Compound Oxidation over RuO_x Supported on Acid-Etched Co_3O_4. *Environ. Sci. Technol.* **2021**, *55*, 10734–10743, doi:10.1021/acs.est.1c02970

2. Results and Discussions (Scientific Publications)

2.1 Publication 1: Unveiling the self-activation of exsolved $LaFe_{0.9}Ru_{0.1}O_3$ perovskite during the catalytic total oxidation of propane

In this paper we find that the hydrogen reduction of LFRO ($LaFe_{0.9}Ru_{0.1}O_3$) at 800 °C leads to the formation of socketed ruthenium particles whose low-temperature activity in the total propane oxidation reaction at 210 °C is substantially lower than that of the original LFRO. Upon increasing the reaction temperature once to 400 °C, the exsolved catalyst undergoes self-activation so that the activity at 210 °C turns out to be five times higher than that of the original LFRO. A variety characterization reveals that after reduction at 800 °C the exsolved Ru particles are slightly alloyed with Fe and encapsulated by an inert and protecting LaOx layer. Mild oxidative treatment at 400 °C leads to the removal of the conforming LaOx layer so that the active Ru species is exposed, explaining the enhancement of the catalytic activity for propane combustion reaction.

The concept and experiment of this publication were designed by H. Over and I. I prepared the Ru-based perovskites and evaluated the catalytic performance. P. Timmer conducted CO-DRIFTS measurement, T. Weber and L. Glatthaar conducted the XPS measurement. W. Wei, A. Spriewald-Luciano, M. Ding contributed to the data analysis and scientific discussion. I wrote the draft and H. Over, B. M. Smarsly, Y. Guo and J. Gallego revised and polished the manuscript.

Reprinted with permissions from Wang, Y.; Gallego, J.; Wang, W.; Timmer, P.; Ding, M.; Spriewald-Luciano, A.; Weber, T.; Glatthaar, L.; Guo, Y.; Smarsly, B. M.; Over, H. Unveiling the Self-Activation of Exsolved $LaFe_{0.9}Ru_{0.1}O_3$ Perovskite during the Catalytic Total Oxidation of Propane. *Chin. J. Catal.* **2023**, 54, 250– 264,

DOI: 10.1016/S1872-2067(23)64547-4.

Copyright © 2023 Dalian Institute of Chemical Physics, the Chinese Academy of Sciences. Published by Elsevier

Chinese Journal of Catalysis 54 (2023) 250–264

available at www.sciencedirect.com

ScienceDirect

journal homepage: www.sciencedirect.com/journal/chinese-journal-of-catalysis

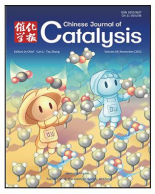

Article

Unveiling the self-activation of exsolved $LaFe_{0.9}Ru_{0.1}O_3$ perovskite during the catalytic total oxidation of propane

Yu Wang [a,b], Jaime Gallego [b,c], Wei Wang [a,b], Phillip Timmer [b], Min Ding [a], Alexander Spriewald Luciano [b], Tim Weber [b], Lorena Glatthaar [b], Yanglong Guo [a,*], Bernd M. Smarsly [b,*], Herbert Over [b,*]

[a] *State Key Laboratory of Green Chemical Engineering and Industrial Catalysis, Research Institute of Industrial Catalysis, School of Chemistry and Molecular Engineering, East China University of Science and Technology, Shanghai 200237, China*

[b] *Institute of Physical Chemistry, Justus Liebig University, Heinrich-Buff-Ring 17, D-35392 Giessen, Germany*

[c] *Center for Materials Research, Justus Liebig University, Heinrich-Buff-Ring 16, D-35392 Giessen, Germany*

ARTICLE INFO

Article history:
Received 30 August 2023
Accepted 19 October 2023
Available online 15 November 2023

Keywords:
$LaFe_{0.9}Ru_{0.1}O_3$ perovskite
Exsolution
Redox treatment
RuO_2
Catalytic total oxidation of propane

ABSTRACT

The exsolution process enables to produce and control the formation of stable and catalytically active nano particles via reductive extraction of uniformly incorporated precious metal ions from a solid oxide solution. Here we consider the simple and stable perovskite $LaFeO_3$ (LFO) where 10% of Fe on B sites are substituted by ruthenium (LFRO). Hydrogen reduction of LFRO at 800 °C leads to the formation of socketed ruthenium particles whose low-temperature activity in the total propane oxidation reaction at 210 °C is substantially lower than that of the original LFRO. Upon increasing the reaction temperature once to 400 °C, the exsolved catalyst undergoes self-activation so that the activity at 210 °C turns out to be five times higher than that of the original LFRO. High-resolution transmission electron microscopy and nanometer-resolved element mapping, together with averaging characterization methods, including X-ray diffraction and X-ray photoelectron spectroscopy, Raman spectroscopy, and diffuse infrared spectroscopy, unveil that after reduction at 800 °C the exsolved Ru particles are slightly alloyed with Fe and encapsulated by an inert and protecting LaO_x layer. Mild oxidative treatment at 400 °C leads to the removal of the conforming LaO_x layer, while the uncovered RuFe alloy particle transforms to catalytically active oxidic Ru species, with no indication of a separate FeO_x phase. We exemplify with our case study of $LaFe_{0.9}Ru_{0.1}O_3$ that careful redox treatment enables to control the exsolution process and to avoid deactivation. This may be of importance for the whole class of exsolvable materials.

© 2023, Dalian Institute of Chemical Physics, Chinese Academy of Sciences.
Published by Elsevier B.V. All rights reserved.

1. Introduction

Catalyst materials with precious metals serving as active component typically consist of small metal nanoparticles (NP) that are supported on a carrier material such as a metal oxide, to increase the active surface area and to stabilize a high dispersion [1]. In order to suppress sintering of the supported NP under reaction condition a strong interaction between the NP

* Corresponding author. E-mail: Herbert.Over@phys.Chemie.uni-giessen.de (H. Over), Bernd.Smarsly@phys.Chemie.uni-giessen.de (B. M. Smarsly), ylguo@ecust.edu.cn (Y. Guo).

This work was supported by the National Key Research and Development Program of China (2022YFB3504200), the National Natural Science Foundation of China (22076047, 21976057, U21A20326), the 111 Project (B08021) and the Fundamental Research Funds for the Central Universities.
https://doi.org/10.1016/S1872-2067(23)64547-4

and the carrier material is considered beneficial.

Supported metal NP catalysts can be prepared by a variety of different methods, including physical mixing, physical or chemical vapor deposition, the deposition-precipitation method, and wet-chemical impregnation [2,3]. Two decades ago, the exsolution process was introduced to produce and control the formation of stable and catalytically active nano particles at the surface via reductive extraction of uniformly incorporated precious metal ions from a solid oxide solution [4,5]. The exsolution strategy allows for a delicate control of the metal particle size and distribution. Exsolved NP are frequently socketed (anchoring effect) into the parent matrix [6,7], thereby enhancing the thermal stability and lifetime of the catalyst in a high-temperature reaction such as reforming reaction or the anode reaction of solid oxide fuel cells [8–10]. Under oxidizing reaction conditions at high temperature the exsolved NP is able to dissolve back into the backbone support [4]. This reversibility of exsolution and dissolution of nanoparticles can be utilized to reactivate the catalys in case the catalyst has undergone severe coking or sintering (so-called self-regeneration) [11]. Several recent reviews have summarized our present understanding of the exsolution process [12–14].

Frequently, ABO_3 perovskite oxides (cation A, coordinated to 12 O anions, is of larger size than the cation B, coordinated to 6 O anions) serve as the parent matrix for the exsolution process due to their flexibility to accommodate a variety of different defects and to substitute partially the B sites by the target metal ion, while retaining structural integrity [15,16]. In general, the less oxygen-affine element on B site is preferentially exsolved, a process that is mediated by tensile strain of the lattice, O-defects, and B-site defects [17,18]. However, the exsolution of the target precious element is sometimes accompanied by the co-exsolution of the other B site element leading to exsolved alloy particles such as PtNi, PdNi, and RuFe [19–22]. Hou *et al.* [23] reported that the exsolved alloy will form an oxide shell covering metallic core structure where the thickness of the shell is closely related to the partial pressure of O_2 in the reducing atmosphere. For the case of RuFe, a covering FeO_x layer forms on Ru particles that can only be removed by brief oxidation at 800 °C where concomitantly the Ru particles start to dissolve [22]. In another study, the exsolved metallic Ru from A-site deficient perovskite is oxidized to RuO_2 nanoparticle instead of dissolving back to the parent matrix when operating as an oxygen electrode in oxidizing atmosphere at 750 °C [24]. Sometimes even the co-segregation of the A-site element is reported to occur, yielding the formation of SrO_x, LaO_x, and BaO_x accompanied by the disintegration of the perovskite structure [25–28]. For the case of $LaNiO_3$ the exsolved Ni particles were reported to be covered by a thick LaO_x layer, accompanied by the total collapse of the perovskite structure [27]. It was found that oxygen vacancies and induced electrostatic interactions play here an important role in the A-site cation segregation toward the surface [29].

In this study we focus on $LaFeO_3$ (LFO), a particularly stable perovskite structure. LFO and substituted derivatives have already been employed as catalysts in the total oxidation reactions of volatile organic compounds [30,31]. The application of LFO as catalyst or catalyst support is motivated by its high oxygen mobility, coupled with high stability, which are instrumental properties in designing catalysts for oxidation reactions.

Here we perform an in-depth study of LFO with the B-sites being partially substituted by Ru^{3+} (LFRO), which is subsequently reduced to achieve exsolution of Ru particles. We deliberately select LFO as a relatively simple perovskite for several reasons. La on A-site in LFO occurs only in the 3+ oxidation state, thus forcing Fe on the B sites to be in the same oxidation state. The investigation of the material's transformation in the course of reduction and catalytic reaction, as well as the interpretation of corresponding analytical data, benefits from a small number of involved elements in LFRO. Ru and RuO_2 are well-known catalytic species possessing high activity for the total oxidation of hydrocarbons, but feature also stability issues [32]. Here, the B-sites of LFO are partially substituted by Ru (LFRO) and are subsequently reduced to achieve exsolution of stable (socketed) Ru particles.

The LFRO materials are catalytically tested in the total oxidation of propane, being a representative of light alkane contained in liquid petroleum gas (LPG). LPG is employed to propel internal combustion engines and thereby constitutes the third most widely used engine fuel world-wide [33]. LPG is employed also as feedstock in chemical industry for synthesis of other olefins. The release of propane and other short-chain alkanes to the atmosphere is of environmental concern, since the photochemical reaction with NO_x and other air-borne chemicals cause chemical smog. Therefore, the slip of propane and other short-chain alkanes to the atmosphere needs to be prevented by catalytic combustion.

The exsolution process is followed by powder X-ray diffraction (XRD), X-ray photoelectron spectroscopy (XPS), infrared and Raman spectroscopy, high-resolution transmission electron microscopy (HRTEM) and nanometer-resolved element mapping to gain microscopic insight into the material's transformation. The exsolution process of LFRO at 800 °C in a reductive environment is shown to form socketed ruthenium particles that are slightly alloyed with Fe, but surprisingly are covered by a passivating ultrathin LaO_x layer. Therefore, the low-temperature activity at 210 °C of exsolved LFRO in the total propane oxidation reaction turns out to be substantially lower than that of the original LFRO. Upon increasing the reaction temperature once to 400 °C, self-activation of the exsolved catalyst is observed to occur. We provide compelling experimental evidence that mild oxidative treatment during the self-activation process at 400 °C causes the selective removal of the LaO_x overlayer, exposing the active oxidic Ru species for the total oxidation of propane. This peeling process is reminiscent of the classic SMSI, such as encountered for Au/TiO_2 [34], Ru/MoO_3 [35] in which the coating layer on the metal in supported catalyst can be selectively removed in the oxidative atmosphere.

2. Experimental

2.1. Materials preparations

Used Materials: Lanthanum (III) nitrate hexahydrate ($La(NO_3)_3{\cdot}6H_2O$, > 99%, Alfa Aesar), iron(III) nitrate nonahydrate ($Fe(NO_3)_3{\cdot}9H_2O$, ≥ 99.95%, Sigma-Aldrich), ruthenium(III) nitrosyl nitrate solution ($Ru(NO)(NO_3)_x(OH)_y$, $x+y = 3$, Sigma-Aldrich), citric acid ($C_6H_8O_7$, ≥ 99.5%, Sigma-Aldrich), and ethylene glycol ($(CH_2OH)_2$, Sigma-Aldrich, ≥ 99.5%) are purchased and directly used without further purification.

To uniformly dope the Ru into the perovskite structure, $LaFe_{0.9}Ru_{0.1}O_3$ nominal mixed oxide is prepared by a sol-gel method following a reported procedure [36]. Typically, 0.004 mol of $La(NO_3)_3{\cdot}6H_2O$, 0.0036 mol of $Fe(NO_3)_3{\cdot}9H_2O$, 0.0004 mol of $Ru(NO)(NO_3)_x(OH)_y$ ((Fe+Ru)/La = 1), and 0.012 mol of citric acid (CA) are dissolved in 50 mL distilled water and mixed with 0.024 mol of ethylene glycol. The solution is stirred at 80 °C until a brown gel is formed. After drying at 120 °C overnight in an oven, the solid material is ground, and the obtained powder is calcined in a muffle furnace under static air at 300 °C for 1 h and subsequently at 750 °C for 3 h with a heating rate of 3 °C·min^{-1}. The resulting black powder (nominal $LaFe_{0.9}Ru_{0.1}O_3$) is denoted as LFRO. For comparison reasons, LFO stoichiometric perovskite oxide, and doped perovskite ($LaFe_{1-x}Ru_xO_3$) are prepared with varying concentrations x (x = 0–0.5) of Ru by the same procedure. Exsolution of ruthenium from the parent perovskite oxide is accomplished as follows. The Ru/LFO catalyst with the Ru loading of 5 mol% is prepared by deposition-precipitation method. 1.0 g of LFO and desired amount of $Ru(NO)(NO_3)_x(OH)_y$ are suspended in 100 mL water, followed by the addition of diluted NaOH solution to adjust the PH to 9. The residual powder is collected by centrifugation and washed with distilled water. After drying overnight, the sample is calcined at 400 °C for 3h.

As-prepared LFRO is reduced under 100 mL·min^{-1} of 4 vol% H_2/Ar gas flow while heating to 800 °C with a heating rate of 3 °C·min^{-1}. The obtained powder is denoted as LFRO_800R. After characterization and catalytic test, the reduced sample LFRO_800R is re-oxidized under 100 mL·min^{-1} of 10 vol% O_2/Ar at different temperatures (200, 300, and 400 °C) for 0.5 h, and the resultant samples are labelled as LFRO_800R_TO, where T stands for the re-oxidation temperature. For example, LFRO_800R_400O is obtained after calcination at 750 °C for 3 h, reduction at 800 °C for 3 h, and re-oxidation at 400 °C for 0.5 h.

2.2. Catalyst characterization

Structural information of the differently processed materials is gained by XRD using a Panalytical X'Pert PRO diffractometer equipped with a Cu-K_α radiation (λ = 1.5418 Å) lamp operated at 40 kV and 40 mA. XRD patterns in the 2θ range of 20°–60° are collected with a step size of 0.013° and an integrated counting time of 2 s per step. Occasionally, LaB_6 is added as a reference to calibrate the 2-theta axis. The averaged particle sizes and micro strain of the samples are determined by using the Williamson-Hall plot method.

The samples are pretreated at 120 °C for 12 h in vacuum before performing N_2 physisorption experiments with an Autosorb 6 instrument (Quantachrome). The Brunauer-Emmett-Teller (BET) method is used to determine the specific surface area.

Raman spectra are collected using a Senterra spectrometer of Bruker Optics with a laser wavelength of 632.8 nm and a power of 2 mW. All samples are measured with a spectral resolution of 5 cm^{-1}, 200 co-additions, and 8 seconds of integration time. The Raman spectra are recorded in backscattering geometry at room temperature and analyzed using the OPUS 7.5 software.

Scanning electron microscopy (SEM) is conducted on a MERLIN instrument (Carl Zeiss AG, Germany) with an acceleration voltage of 3 kV to obtain the morphology of all the prepared samples. Especially, the average size and the size distribution of the exsolved particles are determined by SEM. The elemental compositions of the materials are quantified by energy-dispersive X-ray (EDS) with a X-Max 50 detector (Oxford Instruments, U.K.) employing an acceleration voltage of 10 kV.

HR-TEM is carried out using a Thermo Fisher Talos F200X at 200 kV accelerating voltage. EDS is conducted using 4 in-column Super-X detectors. The powder is suspended in ethanol by sonication and a drop is deposited on a lacey carbon TEM grid.

XPS measurements are conducted on a PHI 5000 VersaProbe II instrument (Physical Electronics GmbH) using Al-K_α radiation (1486.7 eV). Before the XPS measurement, all the samples are degassed overnight in a vacuum oven at 50 °C. Survey spectra (average over three cycles) are acquired in energy steps of 0.8 eV, while high-resolution spectra (average over ten cycles) are taken with a step size of 0.2 eV. All recorded spectra are calibrated to the binding energy of adventitious carbon (C 1*s*) at 284.8 eV. The high-resolution XP spectra are analyzed with Casa XPS version 2.3.17.

In situ diffuse-reflectance infrared Fourier transform spectra (DRIFTS) of CO adsorption are conducted on Bruker Vertex 70V with a resolution of 4 cm^{-1} at room temperature [37]. Before the introduction of CO, LFRO_800R is pretreated with 4 vol% H_2/Ar at 300 °C for 30 min. To prepare the re-oxidized samples, LFRO_800R is pretreated in 10 vol% O_2/Ar at 200, 300, 400 °C for 30 min to obtain LFRO_800R_200O, LFRO_800R_300O, LFRO_800R_400O, respectively. DRIFTS results are collected under the stream of 2 vol% CO/Ar at a flow rate of 20 mL min^{-1}.

2.3. Catalyst activity tests

Propane combustion activity is evaluated in a home-built flow reactor coupled with a nondispersive infrared (NDIR) sensor (Saxon Junkalor INFRALYT 80) running at atmospheric pressure [38]. The characteristic absorption bands of propane and CO_2 are at ~2960 and ~2349 cm^{-1}, respectively, so that their concentrations can be quantified by using the Lambert-Beer law. The purity of reaction gases propane (Nippon Gases), oxygen (Linde) and nitrogen (Linde) are 3.5, 5.0, and 5.0, respectively.

For the catalytic activity measurement, 20 mg of catalyst material is diluted with 40 mg of inert quartz sand and placed in a quartz tubular fixed-bed reactor [39,40]. Argon-balanced feed gas consisting of 1% C_3H_8 and 10% O_2 (volumetric frac-

tion) is admitted to the reactor at a flow rate of 100 mL·min^{-1} (at standard temperature and pressure) that corresponds to a gas hourly space velocity (GSHV) of 345,000 mL·g^{-1}·h^{-1}. The catalytic activity is measured from room temperature to 400 °C with a linear heating rate of 1 °C·min^{-1} and held at 400 °C for 30 min. To determine the conversion, the volumetric concentrations of CO_2 and C_3H_8 during the whole reaction are monitored by an online NDIR sensor. The conversion (X) is evaluated according to

$$X = c(CO_2)/c_{max}(CO_2)$$

where $c(CO_2)$ and $c_{max}(CO_2)$ stand for the measured CO_2 volumetric concentration and the maximum CO_2 volumetric concentration in the outlet gas, respectively. In order to countercheck, the conversion based on propane concentration is determined by

$$X = (c_{in}(C_3H_8) - c_{out}(C_3H_8))/c_{in}(C_3H_8)$$

where $c_{in}(C_3H_8)$ and $c_{out}(C_3H_8)$ stand for the C_3H_8 volumetric concentration in the inlet and outlet stream, respectively. We notice that the light-off curves of the studied samples based on CO_2 and C_3H_8 detection are practically identical. In addition, the concentration of CO_2 in the outlet gas is three times that of propane in the inlet gas when propane is fully converted.

The kinetic data for the propane combustion reaction are obtained under the same testing condition mentioned above, but the conversion is kept below 15%, where heat transfer limitation is excluded according to Mears criterion (C_M) [41]; further details are provided in the ESI. The STY (space time yield) is defined as the molar amount of product per time and per mass of catalyst (mol_{CO2}·h^{-1}·kg_{cat}^{-1}).

3. Results and discussion

3.1. Results

The XRD patterns of the perovskite samples are depicted in Fig. 1(a). For the as-synthesized LFO sample, the internal standard LaB_6 (JCPDS card NO. 34-0427 with reflections at 2θ = 21.3°, 30.4°, 37.4°, 43.5°, and 48.9°) is used as the reference to calibrate the 2-theta axis of the XRD patterns. The other detected diffraction signals are characteristic of the orthorhombic perovskite $LaFeO_3$ (JCPDS NO. 88-0641). By comparing the magnified (121) diffraction peak in Fig. 1(b), no pronounced peak shift can be detected when 10% of Fe in B-site is substituted by Ru (LFRO after calcination) compared to LFO. With increasing Ru/(Fe+Ru) atomic ratio above 10%, the (121) diffraction peak gradually shifts to lower angles (Fig. S1(b)), which can be traced to the slightly larger ionic radius of Ru^{3+} (0.68 Å) compared to Fe^{3+} (0.645 Å). The diffraction peaks of the RuO_2 phase start to be discernible in the sample with a Ru/(Ru + Fe) atomic ratio of 40% (Fig. S1(a)). For in depth investigation, we choose the sample $LaFe_{0.9}Ru_{0.1}O_3$ (LFRO) with low Ru doping (5 mol%) to avoid the RuO_2 phase segregation and to economize the precious element.

Upon Ru substitution the micro strain of LFRO increased to 0.27% that is significantly higher than that of the undoped LFO sample (0.17%) (using the Williamson-Hall plot, Fig. S2). The higher micro strain is indicative of increased structural disorder which results from the introduction of a dopant (Ru in this case) with a slightly larger ionic radius [42]. After reduction under H_2 at 800 °C for 3 h, the XRD pattern of the Ru-doped sample LFRO_800R does not alter, thus evidencing the high stability of this Fe-based perovskite in a strongly reducing atmosphere. The micro strain of the exsolved sample LFRO_800R is calculated to be 0.21%. The decrease in micro strain after high temperature reduction is caused by Ru exsolution that in turn is compensated by oxygen vacancy formation. The (121) reflection of LFRO_800R shifts slightly towards a lower 2-theta value (see the enlarged plot in Fig. 1(b)). This lattice expansion may point to a partial reduction of Fe^{3+} (ionic radius: 0.645 Å) to Fe^{2+} (ionic radius: 0.780 Å) that has likely been triggered by oxygen vacancy formation [43].

Fig. S3(a) presents Raman spectra of the perovskite in the spectral range of 300–800 cm^{-1}. There are three spectral features centered at 416, 434, and 643 cm^{-1}, which are consistent with reported wave numbers of lanthanum ferrite, evidencing the formation of the $LaFeO_3$ perovskite oxide (LFO) [44]. The first two maxima are related to the scissor-like bending mode of O–Fe–O bond (A_g) and the stretching mode of Fe–O bond (B_g), respectively. However, the assignment of the peak centered at 643 cm^{-1} (peak C) is ambiguous. Some authors assigned this peak as a Jahn-Teller like mode [45], while others ascribed this peak to Fe–O stretching mode or to impurities in the structure [44,46].

When 10% of Fe is substituted by Ru (LFRO), a significant broadening of A_g and B_g modes occurs that can be ascribed to the distortion of the FeO_6 octahedra and a loss of symmetry. Concomitantly the third peak (643 cm^{-1}) shifts to higher wavenumber (671 cm^{-1}). Since the only difference between LFO and LFRO is the incorporation of Ru, we can infer that this signal shift results from Ru doping. After thermal reduction in H_2 at 800 °C for 3 h (LFRO_800R), part of the incorporated Ru in the perovskite structure is exsolved to the surface, leading to a redshift of the third mode to 658 cm^{-1}.

There is a clear correlation between micro strain and the Raman shift (peak C) of the studied samples as summarized in Fig. S3(b). Substitution of Fe by Ru in the LFO perovskite structure increases the micro strain and decreases the crystal symmetry, while the Raman feature C is blue-shifted. When LFRO is treated in a reducing atmosphere at 800 °C for 3 h, the

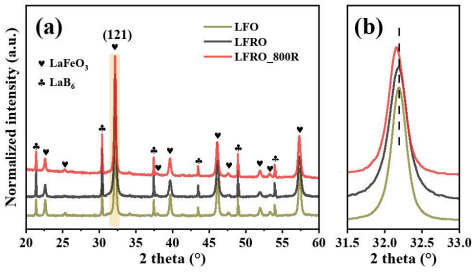

Fig. 1. XRD patterns (a) and enlarged ones (b) of the LFO, LFRO, and LFRO_800R. LaB_6 was used as internal standard to calibrate the 2-theta axis.

Table 1
Physicochemical properties of the studied perovskite samples. Pure LFO, LFRO, and LFRO_800R.

Sample	Ru/La+Fe+Ru (mol%) [a]	A_{BET} ($m^2 \cdot g^{-1}$)	Micro strain [b] (%)	Atomic ratio [c] (mol%)			$Ru^{\alpha/\beta}$ [c] (mol%)		
				Ru	La	Fe	Ru^{α}	Ru^{β}	Ru^{0}
LFO	—	9	0.17	0	55	45	—	—	—
LFRO	5.1	12	0.27	8	54	38	79	21	0
LFRO_800R	5.0	11	0.21	13	55	32	0	12	88

[a] Determined by SEM-EDS. [b] Calculated by Williamson-Hall Plot. [c] Derived by XPS.

observed redshift of the Raman peak C and the decrease of micro strain may indicate Ru exsolution.

In the SEM images (cf. Fig. S4), both the LFO and LFRO samples show a similar coral-like morphology with a smooth surface assembled by grains possessing a size of several hundreds of nanometers. After thermal reduction at 800 °C for 3 h, nanoparticles with a size distribution of around 10 ± 2 nm uniformly decorate the parent perovskite oxide surface. The appearance of the nanoparticles in SEM verifies the exsolution of the metal from the parent perovskite oxide matrix, which could also be verified by the TEM results in Fig. S5. The bulk elemental compositions in the Ru-containing oxides are analyzed using SEM-EDS. As listed in Table 1, the Ru-doped LFRO and the exsolved sample LFRO_800R have Ru contents of 5.1 mol% and 5.0 mol% (Ru/Ru+Fe+La), respectively, which are both close to the nominal value of 5 mol%. The BET surface area slightly increases from the original 9 $m^2 \cdot g^{-1}$ (LFO) to 12 $m^2 \cdot g^{-1}$ after Ru incorporation (LFRO) and keeps constant (11 $m^2 \cdot g^{-1}$) after thermal reduction (LFRO_800R).

XPS spectra are acquired to gain information on the elemental composition and the oxidation state of Ru species (Fig. 2) in the near-surface region of the catalyst. For LFO, two spectral features at ~284.8 and ~288.7 eV are assigned to adventitious carbon (C–C) and carbonates (CO_3^{2-}), respectively. The CO_3^{2-} species originates from the adsorption of CO_2 on the lanthanum surface species [47]. This is attributed to the high basicity character of the lanthanum oxide compounds.

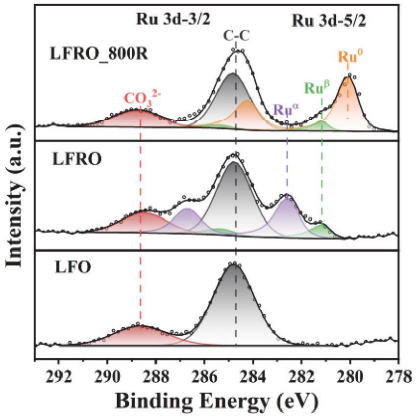

Fig. 2. Ru 3*d* + C 1*s* XPS spectra for LFO, LFRO, and LFRO_800R. The Ru 3*d* spectra are decomposed into Ru^{α} (purple), Ru^{β} (green), and metallic Ru (Ru^0, orange).

For the Ru-containing sample, several Ru features can be observed in XPS after the deconvolution of the overlapping peaks. Ru^{α} at ~282.4 eV can be assigned to the Ru^{3+} [48] in the perovskite structure, but its binding energy also overlaps with the satellite feature of Ru^{4+} in RuO_2 [49]. Ru^{3+} is an unusual oxidation state in Ru-containing solid oxides that is only found for Ru in B-sites of perovskite oxides due to the unique ionic-coordination environment and electroneutrality [24]. Moreover, Ru^{3+} can form in LFRO a high-spin state in the octahedral ligand field that may lead to further stabilization of the Ru^{3+}. Ru^{β} at a lower binding energy (~281 eV) indicates a less oxidative environment compared to Ru^{α}. The binding energy position of Ru^{β} is identical to that of Ru^{4+} [48,49] and Ru^{2+} [48]. However, under such reducing reaction conditions Ru^{β} needs to be Ru in a lower oxidation, i.e., Ru^{2+} that can be associated with low-coordinated Ru surrounded by oxygen vacancies into the perovskite. With this assignment, the Ru^{α} of LRFO species is uniquely assigned to Ru^{3+}. The feature at the lowest binding energy of 280 eV is unambiguously ascribed to metallic Ru in the oxidation state 0 (Ru^0) [48,49]. In the following, we keep with Ru^{α} and Ru^{β} to emphasize the remaining ambiguity in assigning the true oxidation state of the other two Ru 3*d* features.

When 10% Fe is substituted by Ru, all of Ru is successfully incorporated into the perovskite structure, namely 79% Ru^{3+} and 21% Ru^{β}. After reductive treatment at 800 °C, the Ru^{3+} signal vanishes while Ru^0 (metallic Ru) dominates the Ru $3d_{5/2}$ XP spectra. In general, a metal in oxidation state 0, such as Ru^0, is not stable in a perovskite lattice due to its large size, implying that the Ru^0 signal in XPS is due solely to the exsolution of the Ru from the lattice to the surface within the XPS probing depth. On the other hand, the near-surface molar fraction of Ru species in LFRO_800R significantly increased from 8% to 13% after high temperature reduction.

The light-off curves for the catalytic propane combustion are depicted in Fig. 3. As expected, the Ru-free sample LFO shows relatively low catalytic activity where only 50% propane conversion is accomplished at 400 °C and the 10% propane conversion temperature (T_{10}) is 336 °C. When 10% of Fe (atomic fraction) in the perovskite oxide is substituted by Ru, the activity is greatly enhanced (LFRO_1st) and propane can be totally converted to CO_2 below 400 °C. The T_{10} value significantly reduces from 336 °C to 247 °C, indicating that surface-bound Ru species act as the active sites for the propane combustion reaction. Ru-doped LFRO was also tested for a second light-off experiment (LFRO_2nd), revealing a T_{10} value of 250 °C and hence a stable behavior of LFRO.

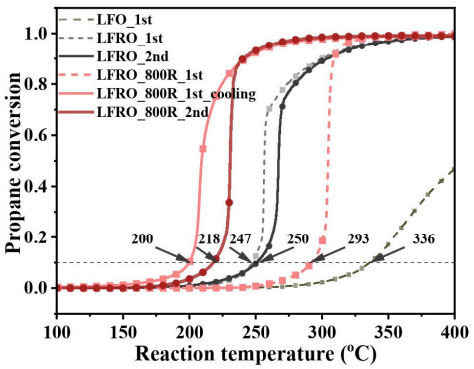

Fig. 3. Two consecutive light-off curves of LFRO and LFRO_800R for propane combustion reaction. The light-off curve of LFO_1st and LFRO_800R_1st_cooling are also provided for comparison.

After thermal reduction of LFRO at 800 °C for 3 h, XPS and SEM evidence the formation of exsolved Ru nanoparticles (size ≈ 10 nm) at the surface that are expected to improve the catalytic activity in the propane combustion reaction. The catalytic activity of LFRO_800R is substantially lower than that of LFRO as evidenced by an increase of T_{10} from 247 to 291 °C. Obviously, the reduction of LFRO leads to deactivation. When the reactor is cooled down under the reaction stream (C_3H_8 + O_2 + Ar), we notice that the propane conversion is significantly enhanced, revealing a T_{10} value of 200 °C (LFRO_800R_1st_cooling in Fig. 3).

To confirm the self-activation of the exsolved sample (LFRO_800R_1st) during the first light-off scan, we conduct a second light-off experiment with the result that the activity of LFRO_800R_2nd is substantially enhanced with a T_{10} value of 218 °C, compared to 291 °C in the first light-off curve. A T_{10} value of 218 °C is even lower than that of LFRO (247 °C), revealing now the expected activity increase of exsolved LFRO. This lowering of the T_{10} value of LFRO_800R_2nd after the first light-off experiment is likely traced to a pronounced change in the catalyst's material.

The temperature treatment in an oxidative reaction environment can be considered to be the determining factor for the self-activation of the exsolved sample LFRO_800R during the first light-off curve (1% C_3H_8 + 10% O_2 + 89% Ar, from room temperature to 400 °C). In order to test this proposition, several LFRO_800R samples are prepared by pretreating them in an oxidative atmosphere (10% O_2 balanced in Ar) at various temperatures ranging from 200 to 400 °C for 30 min prior to conducting the catalytic tests. As displayed in Fig. 4 and summarized in Table 2, with increasing re-oxidation temperature the catalytic performance for the first light-off curve is improved and the hysteresis of consecutive light-off curves narrows down. The T_{10} value of the first light-off curve decreases from 285 °C (LFRO_800R_200O) to 262 °C (LFRO_800R_300O) and finally to 219 °C (LFRO_800R_400O) that is close to that of LFRO_800R_2nd (218 °C). In addition, the LFRO_800R_500O sample is also prepared and tested. The achieved T_{10} value of 223 °C (Fig. S6) is slightly higher than that of LFRO_800R_400O (219 °C), thus indicating that a re-oxidation temperature of 400 °C optimizes the oxidative re-activation process of LFRO_800R. Besides, all re-oxidized samples are subject to a second light-off experiment, revealing now a nearly constant T_{10} value for the three re-oxidized samples (221 ± 3 °C). A series of third light-off experiments for the re-oxidized LFRO_800R (not shown) are identical to those in the second run.

To further evaluate the catalytic performance, the activity of the catalysts in terms of STY at 210 °C and the corresponding Arrhenius plots are measured and shown in Fig. S7 and summarized in Table 2. It can be noticed that LFRO suffers from a severe activity decrease after 800 °C reduction treatment. And for the mildly re-oxidized samples at various temperatures, the STY values at 210 °C for the first light-off experiment are ordered as follows: LFRO_800R_400O (22.3 $mol_{CO2}·h^{-1}·kg_{cat}^{-1}$) > LFRO_800R_300O (3.2 $mol_{CO2}·h^{-1}·kg_{cat}^{-1}$) > LFRO_800R_200O (0.35 $mol_{CO2}·h^{-1}·kg_{cat}^{-1}$) > LFRO_800R (0.27 $mol_{CO2}·h^{-1}·kg_{cat}^{-1}$), while the apparent activation energies E_a values follow a reversed sequence LFRO_800R (146 kJ·mol^{-1}) > LFRO_800R_200O (125 kJ·mol^{-1}) > LFRO_800R_300O (111 kJ·mol^{-1}) > LFRO_800R_400O (97 kJ·mol^{-1}). For the second

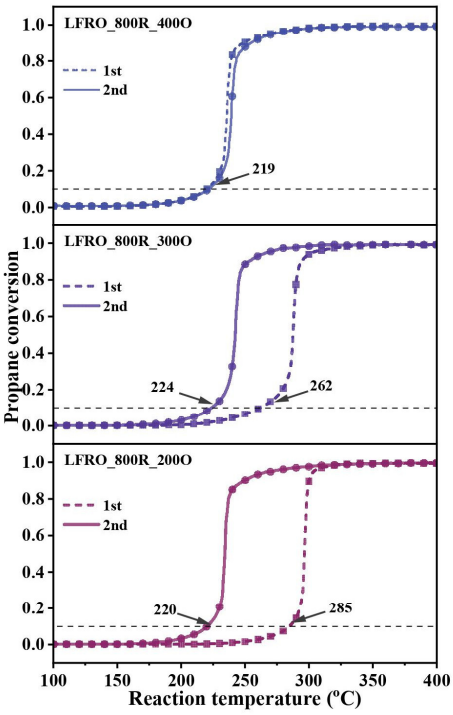

Fig. 4. Self - activation identified with two consecutive propane combustion light-off curves (1st and 2nd) of LFRO_800R_200O, LFRO_800R_300O and LFRO_800R_400O.

Table 2
Catalytic behavior and kinetic parameters of the investigated samples during the first and second catalytic activity test.

Sample	1st					2nd				
	T_{10} (°C)	T_{50} (°C)	T_{90} (°C)	STY [a]	E_a (kJ/mol)	T_{10} (°C)	T_{50} (°C)	T_{90} (°C)	STY [a]	E_a (kJ·mol^{-1})
LFRO	247	257	302	4.96	118	250	267	305	4.0	94
LFRO_800R	293	304	308	0.27	146	218	230	240	23.5	109
LFRO_800R_200O	285	297	300	0.35	125	220	234	249	20.6	106
LFRO_800R_300O	262	287	294	3.2	111	224	243	254	19.8	95
LFRO_800R_400O	219	235	248	22.3	97	219	235	250	23.0	98

[a] Calculated at 210 °C and given in $mol_{CO2}·h^{-1}·kg_{cat}^{-1}$.

light-off experiment the STY values of LFRO_800R, LFRO_800R_200O, LFRO_800R_300O, and LFRO_800R_400 are practically identical (21 ± 2 $mol_{CO2}·h^{-1}·kg_{cat}^{-1}$), while the apparent activation energies are 100 ± 10 kJ·mol^{-1}. For comparison reasons, supported Ru/LFO catalyst with identical Ru loading is measured, revealing a T_{10} of 243 °C (Fig. S8), and the corresponding STY at 210 °C is determined to be 5.5 $mol_{CO2}·h^{-1}·kg_{cat}^{-1}$. The LFRO_800R_400O reveals a high stability in propane oxidation reaction at 255 °C over 10 h (Fig. S9).

To elucidate the de-activation process after high-temperature reduction and the correlation between re-oxidation temperature and self-activation of the catalyst, the reduced sample (LFRO_800R) and three re-oxidized samples (LFRO_800R_200O, LFRO_800R_300O, and LFRO_800R_400O) are fully characterized. XRD and Raman, as bulk-sensitive characterization methods, are carried out, and the results are summarized in Figs. S10, S11. The virtually identical XRD patterns and Raman spectra of the three re-oxidized samples compared to LFRO_800R indicate that no substantial changes in the bulk structure occur during the mild re-oxidation process. From SEM micrographs in Fig. S12, the mean size of exsolved Ru particles in LFRO_800R, LFRO_800R_200O, LFRO_800R_300O, and LFRO_800R_400O are 10, 11, 10, and 12 nm, respectively. Evidently, the size distributions of exsolved particles vary only little with the re-oxidation temperature, thus verifying that the particle size change has a negligible impact on the observed re-activation process.

Propane combustion reaction is a typical heterogeneous reaction where the reactant molecules are firstly adsorbed and activated on the surface. Therefore, the surface structure and composition of the active component are of critical importance for catalytic performance. The morphological evolution of the exsolved particles with increasing re-oxidation temperature is followed by high-resolution TEM (HRTEM) in Fig. 5. Clearly, core-shell structured nanoparticles are discernible on the parent perovskite surface (LFRO_800R). It is possible to distinguish the coating layer from the core phase with a well-defined interface and a shell thickness of around 0.8 nm (Fig. 5(a)). The core-shell structured morphology is hardly affected by a 200 °C re-oxidation treatment in 10 vol% O_2/Ar for 30 min (Fig. 5(b)), while the coating layer breaks up when treated at 300 °C in oxygen (Fig. 5(c)). After re-oxidation at 400 °C in 10 vol% O_2/Ar for 30 min, the coating layer on the exsolved particles disappears (Fig. 5(d)).

EDS elemental mappings of an exsolved particle of LFRO_800R and LFRO_800R_400O are presented in Fig. 6. For the reduced sample LFRO_800R, Ru and Fe are homogeneously distributed in the core of the particle, while La is enriched in the shell around the particle (Fig. 6(c)). Since the line scan of La is wider (by about 1nm on each side) than that of Ru and Fe in Fig. 6(d), the 1nm thick shell of the exsolved particle is evidenced to be mainly composed of La, while Ru and Fe are evenly distributed in the core part. As shown in Table 3, the atomic ratios of La, Fe, and Ru are determined to be 11%, 14%, and 75% in the selected area of the particle (Fig. 6(c)), suggesting that Ru is markedly enriched in the alloy.

Combining these results with the HR-TEM image in Fig. 5(a), we conclude that the structure of exsolved core-shell particle consists of a Ru-enriched RuFe alloy core that is encapsulated by an ultrathin La-based layer (0.8–1.0 nm thick). After mild oxidation treatment at 400 °C for 30 min, the atomic contents of La, Fe and Ru in the exsolved particle (Fig. 6(g)) are measured to be 3%, 17% and 80% (Table 3), respectively. The concentration of La in the exsolved particle is substantially reduced after re-oxidation at 400 °C from 11% to 3%, which is also supported by the faintly visible La mapping in Fig. 6(f). Very likely, most of La moves back to the surface of the perovskite structure. All three elements are simultaneously detected

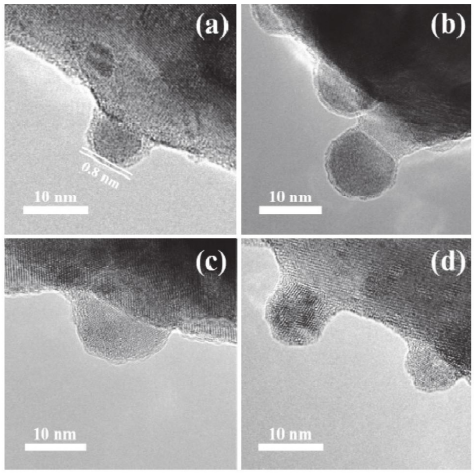

Fig. 5. HRTEM micrographs of the "self-activation" process: LFRO_800R (a), LFRO_800R_200O (b), LFRO_800R_300O (c) and LFRO_800R_400O (d). The reduced sample (LFRO_800R) exhibits core-shell structured particles partially socketed into the parent matrix.

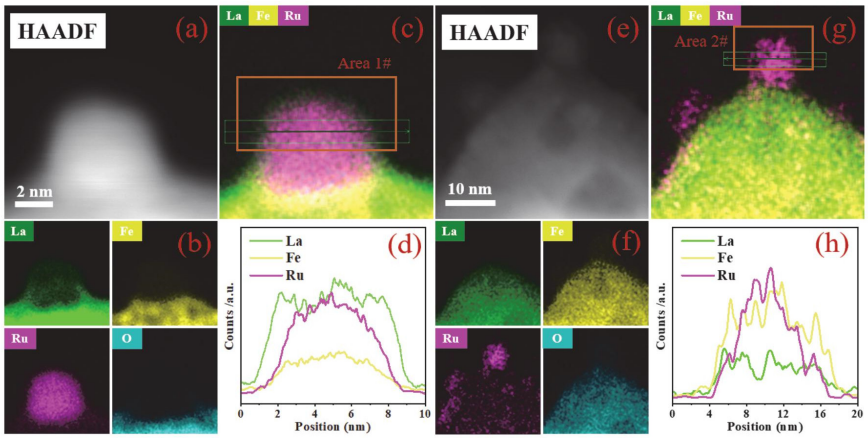

Fig. 6. HAADF-STEM image, EDS elemental mapping image and corresponding line scan results of LFRO_800R (a–d) and LFRO_800R_400O (e–h). The positions for the compositional analysis (orange frame) and line scan measurement (green frame with an arrow) are presented in (c) and (g).

in the line scan profile in Fig. 6(h), indicating that residual La is homogenously mixed with Ru and Fe in the exsolved particle.

With XPS, the evolution of the surface composition and the oxidation state of Ru of the exsolved LFRO_800R can be followed during the "activation" process depending on the re-oxidation temperature (cf. Fig. 7 and results are summarized in Table 4). Upon varying the re-oxidation temperature from 200 to 400 °C, the concentration of Ru is found to be not altered, while its distribution among the oxidation states varies considerably. As indicated in Table 1, 84% of Ru in LFRO_800R is detected to be Ru^0 that is assigned to metallic Ru in the RuFe alloy. The remaining fraction of 16% is attributed to Ru^{β}, while no Ru^{α} species is detected. After oxidative treatment at 200 °C, half of the metallic Ru is oxidized to form 14% Ru^{α} and 41% Ru^{β}. When the re-oxidation temperature is increased to 300 °C, the oxidation of Ru^0 to Ru^{β} and Ru^{α} continues and only 11% Ru^0 is left. When LFRO_800R is re-oxidized at 400 °C, the missing Ru^0 signal demonstrates that Ru within the XPS probe depth is now completely transformed to the oxidized states, namely to 58% Ru^{β} and 42% Ru^{α}.

Table 3
Elemental composition of the exsolved particles of LFRO_800R and LFRO_800R_400O.

Sample	La/at%	Fe/at%	Ru/at%
LFRO_800R	11	14	75
LFRO_800R_400O	3	17	80

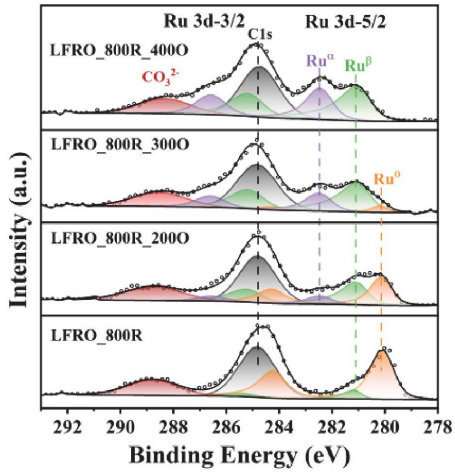

Fig. 7. Ru 3*d* XPS spectra of the reduced sample LFRO_800R and after re-oxidation LFRO_800R_200O, LFRO_800R_300O, and LFRO_800R_400O.

Assuming for a rough estimate that the fraction of Ru^{β} for LFRO_800R are assigned to low-coordinated Ru surrounded by oxygen vacancies into the perovskite and this fraction of 16% remains constant during mild oxidation treatment, then the increase of Ru^{β} upon mild re-oxidation is ascribed to the formation of RuO_2 (Ru^{4+}) with an overlapping satellite feature at the Ru^{α} binding energy position. For the oxidation at 200, 300 and 400 °C the increase in Ru^{β} is due to the increasing Ru^{4+} fraction of 25%, 39%, and 43%, respectively. As the corresponding satellite feature has about 50% of the intensity of that of Ru^{4+} [48], the fraction Ru^{3+} can be determined from the Ru^{α} signal: For the oxidation at 200, 300, and 400 °C the fraction of Ru^{3+} increases to 2%, 14%, and 21%, respectively. The reappearance of Ru^{3+} evidences the partial re-incorporation of the exsolved Ru into the perovskite structure occurring already at a temperature of as low as 300 °C.

The increase in Ru^{3+} concentration is supplied from the exsolved Ru particle and should decrease the particle size. For the re-oxidation at 400 °C, this loss of 21% accounts for a decrease of mean diameter by 7.5%. Since the transformation of

Table 4
Physicochemical properties of the re-oxidized LFRO_800R samples.

Sample	Ru/La+Fe+Ru [a] (mol%)	A_{BET} ($m^2 \cdot g^{-1}$)	$d_{(particle\ size)}$ [b] (nm)	Atomic ratio [c] (mol%)			Ru^{α} (mol%) [c]		
				Ru	La	Fe	Ru^{3+}	Ru^{β}	Ru^{0}
LFRO_800R_200O	5.1	10	11 ± 3	12	55	33	14	41	44
LFRO_800R_300O	4.9	9	10 ± 2	12	54	34	34	55	11
LFRO_800R_400O	5.0	10	12 ± 3	13	53	34	42	58	0

[a] Determined by SEM-EDS.
[b] Exsolved particle size distribution derived based on SEM results.
[c] Derived by XPS.

metallic Ru towards RuO_2 is accompanied by an increase of 30 % in volume, the averages particle size should slightly increase as reconciled in the particle size distributions derived from SEM micrographs (cf. Fig. S12 and Table 4).

In-situ CO-DRIFTS data is collected at room temperature to elucidate the self-activation process under the oxidative atmosphere, which is related to the formation and removal of the La-based covering layer. CO-DRIFTS is surface sensitive and provides a global view on the re-activation process; note that HR-TEM provides only a local view on the self-activation process. Employing a probe molecule, such as CO, infrared spectroscopy can be used to probe the status and chemical nature of the active phase of the catalyst [50,51].

As depicted in Fig. 8, the almost identical CO adsorption behavior before (LFRO) and after reduction (LFRO_800R) suggests that the exsolved particles suppress CO adsorption at room temperature being fully consistent with a passivating La-based layer on the exsolved Ru particle as evidenced by HRTEM and elemental mapping. The observed CO band at 2060 cm^{-1} is assigned to terminal CO both on cationic and neutral Ru species [52,53]. When treated at 200 °C in 10 vol% O_2 for 30 min, a broad CO adsorption features emerge in the range of 1970–2030 cm^{-1} whose intensities slightly increase after an oxidic treatment at 300 °C, indicating the exposure of additional Ru species. These additional CO bands are assigned to terminal and bridging CO species adsorbed on partially reduced RuO_2 [54]. As the re-oxidation temperature increases to 400 °C, the range of the overlapping CO peaks extends from 1940–2040 cm^{-1} concomitantly with an overall enhancement in the intensity. These findings corroborate clearly the removal of the inert La-based coating layer and CO adsorption on the exsolved oxidized Ru particles for the entire sample and not just for an individual particle studied by HRTEM.

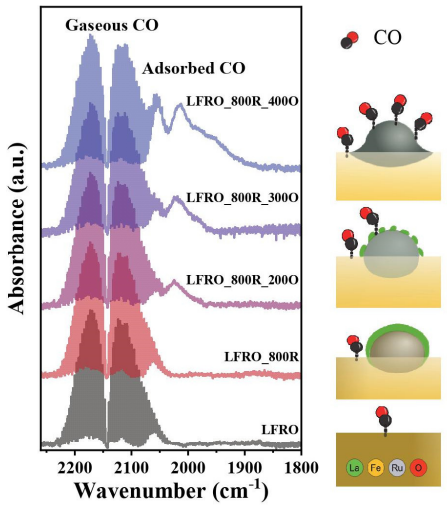

Fig. 8. *In-situ* CO-adsorption infrared spectra of LFRO, LFRO_800R, LFRO_800R_200O, LFRO_800R_300O and LFRO_800R_400O. The spectral intensities are normalized according to the gaseous CO with its pronounced rotational vibrational bands. The assignment of the spectral features of adsorbed CO are pictorially shown on the right side.

3.2. Discussion

3.2.1. Structure evolution

We choose $LaFeO_3$ (LFO) as the parent oxide, since La in A-site in combination with Fe in B-site forms highly stable perovskite structures where both La and Fe of $LaFeO_3$ are in 3+ oxidation state. Substituting part of Fe by Ru (LFRO) will force Ru in LFRO also into the 3+ oxidation state that can easily be discriminated from Ru^0, the oxidation states of metallic Ru of the exsolved particles.

Ru-substituted $LaFeO_3$ perovskite oxide (LFRO) is prepared by employing the simple sol-gel method. The appearance of the dominating Ru^{3+} species in XPS (Fig. 2) in the as-synthesized LFRO sample demonstrates the successful incorporation of Ru into the perovskite structure. The structural evolution of LFRO during the exsolution (reduction) and re-oxidation (under oxygen or propane reaction stream) process is schematically summarized in Fig. 9. During the thermal reduction treatment (at 800 °C for 3 h) of LFRO (LFRO_800R) virtually all ruthenium located in the near-surface region (within the XPS probing depth) is exsolved, as evidenced by the vanishing Ru^{3+} signal and the appearance of the strong Ru^0 signal in Ru 3d spectra (cf. Fig. 2). XPS indicates that the total amount of Ru in the surface region is enriched from 8 at% to 13 at% due likely to migration of Ru from the bulk towards the surface. The exsolution process of Ru from the bulk is fully compatible with the decrease of micro strain as determined by XRD and corroborated by a redshift of a Raman signal (cf. Fig. S3).

In general, the exsolution propensity of Fe in LFO is thermodynamically and kinetically limited due to the high segregation energy and high reduction potential of Fe [17]. However,

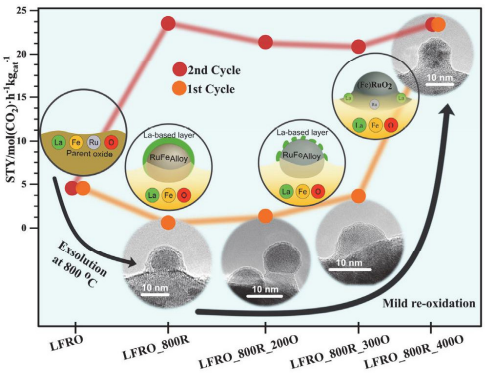

Fig. 9. Structure-activity correlation (STY *vs.* HRTEM) during propane combustion reaction over studied samples. The schematic model of surface reconstruction of LFRO in reducing atmosphere and oxidizing atmosphere are indicated. LFRO is the as-prepared sample after calcination at 750 °C. LFRO_800R, is the LFRO sample with exsolved particles after reduction at 800 °C for 3 h, LFRO_800R_TO, denote the samples after an oxidative (under 10% O_2/Ar) restoration of LFRO_800R at different temperatures *T* (200 to 400 °C). The activity data are given as STY for a reaction mixture of C_3H_8: O_2: Ar = 1: 9: 90 and a flow rate of 100 mL·min^{-1}, 20 mg of catalyst and a reaction temperature of 210 °C. Orange dots indicate the STY values at 210°C during the first light-off experiment up to 400 °C, while the red dots refer to STY values at 210 °C during the second light-off experiment.

when Fe in the B-sites of the perovskite oxide are partially substituted by another element with lower segregation energy and lower reduction potential, such as Ni, Co, or Ru, Fe can partially co-exsolve [55–57]. Combining *in-situ* STEM observations and DFT calculations, Lv et al. demonstrated that Fe migrates into the exsolved Ru^0 particle and forms a RuFe alloy instead of a separate metallic Fe particle [22]. In this study here we observe also the formation of exsolved RuFe alloy particles, however, covered by La-based layer.

For LFRO_800R, the core-shell structured nanoparticle decorating the parent matrix is unveiled by HRTEM in Fig. 5(a). With EDS mapping and the corresponding line scan results in Fig. 6(d), the coating layer is shown to be composed of La, while Fe and Ru are homogeneously distributed in the core of the exsolved particle. The composition of the exsolved particle determined by EDS (75 at% Ru, 14 at% Fe and 11 at% La) evidences that Ru is the majority species in the RuFe alloy core. The starting material LFRO is a perovskite oxide with nominal composition La/(Fe+Ru) = 1. However, after partial exsolution of B-site elements, the support transforms to an A-site enriched perovskite oxide (La/(Fe+Ru) > 1) [58]. In our case, the excess of La is likely to be dissolved in the exsolved particle similar to Fe. Since even minute concentrations of oxygen in the reducing atmosphere are able to oxidize La, and the covering layer is likely to be LaO_x that reduces substantially the surface energy of the metallic RuFe nanoparticle.

The formation of the core-shell structure is at first glance reminiscent to the classical strong metal support interaction (SMSI) state of the supported catalyst prepared by conventional deposition methods where the metal nanoparticle is covered by a (partially reduced) support oxide layer [59–61]. However, if we take the term SMSI, i.e. strong metal support interaction, literally, then the observed LaO_x layer on Ru does not belong to the classic SMSI, because the coating layer is a consequence of the exsolution process and not due to strong Ru-support interaction. But also the underlying process in the formation of the LaO_x covering layer is very different from SMSI. The formation of the LaO_x layer is not just an add-on to the exsolution process, but rather the formation of the LaO_x layer is induced by the exsolution process, a novel phenomenon. Without exsolution, the covering LaO_x is not formed, even if Ru particles are present on the surface. For this reason, we designed an additional experiment for Ru particles that are deposited on $LaFeO_3$ and carried out the very same high temperature reduction (at 800 °C) treatment as in the exsolution process (see Fig. S13). The activity in the propane oxidation reaction turns out to be not affected by this reduction step. CO-DRIFTS of Ru/LFO_800R in Fig. S14(a) reveals overlapping bands in the range of 1900–2050 cm^{-1} due to CO adsorption on the Ru particles. After mild oxidative treatment at 400 °C, a noticeable shift is observed in the positions of the adsorbed CO features in Fig. S14(b), with no discernible change in the intensity. This observation is further corroborated by the nearly identical light-off curves of Ru/LFO_800R in two reaction cycles in Fig. S13, collectively excluding self-activation and the presence of a surface covering layer on the Ru particle in the supported sample.

Fig. S15 provides a typical SEM micrograph of the supported Ru/LFO_800R and the size distribution of Ru particles. The wide size distribution of Ru nanoparticles with a mean size of 34 nm suggests that the supported Ru has undergone severe agglomeration during the preparation. This explains also why the activity of Ru/LFO is lower than that of exsolved Ru sample (LFRO_800R_400O).

Different from the classic SMSI in the supported catalysts such as Au/TiO_2 [34] or Ru/MoO_3 [35], the removal of the covering LaO_x layer by mild oxidation is accompanied by the partial dissolution of the exsolved particle during the "self-activation" process, meaning that the self-activation is not only a kind of surface cleaning, but is also accompanied by the reconstruction of the exsolved particle. To the best of our knowledge, the removal of the covering layer of exsolved particles has not been reported in the literature since more attention has been paid to investigating the reversibility of exsolved particles at high oxidation temperatures.

When treating the LFRO_800R sample with 10% O_2/Ar at various temperatures ranging from 200 to 400 °C, the support retains its perovskite structure, as evidenced by XRD and Raman results in Figs. S10 and S11. However, HRTEM reveals the deformation and partial removal of the LaO_x coating layer depending on the re-oxidation temperature (Figs. 5 and 6), while element mapping signifies a pronounced decrease in the La concentration of the exsolved particle from 11% to 3%. These findings suggest that most of La moves to the support. The resulting oxidized particles, as proven by XPS, are a mixture composed of oxidic Ru, Fe and residual La (80 at% Ru, 17 at% Fe, and 3 at% La). Metallic Ru is fully transformed, at least in

the escape depth of the photoelectrons.

The re-activated LFRO_800R_400O catalyst exposes uncovered Ru particles so that we can now check for the classic SMSI by conducting a second reduction treatment at 800 °C for 3 h (LFRO_800R_400O_800R) and studying the propane oxidation activity and surface properties of the Ru particles by CO-DRIFTS. The catalytic activity of the activated sample LFRO_800R_400O decreases after another 800R treatment, revealing a T10 value of 261 °C (Fig. S16), although its catalytic performance is still substantially higher than that of LFRO_800R. The broad feature of adsorbed CO of LFRO_800R_400O_800R in DRIFTS (Fig. S17) verifies the existence of accessible CO adsorption active sites in the form of exposed Ru sites. The activity of LFRO_800R_400O_800R is increased in the second reaction cycle (cf. Fig. S16), indicating activation of this sample as a result of partial removal of the covering layer. However, its activity is lower when compared with LFRO_800R_400O, which is paralleled by lower intensity of the CO adsorption band of LFRO_800R_400O_800R_400O in CO-DRIFTS in Fig. S17.

These experiments of LFRO_800R_400O_800R can be summarized as follows. The exsolution of Ru from LFRO (LFRO_800R) produces Ru nanoparticles that are fully covered by a La-based layer. The covering layer can be fully removed by a 400O treatment (LFRO_800R_400O: self-activation) producing Ru particles on LFRO. In a second reduction treatment (LFRO_800R_400O_800R) the uncovered Ru particles of LFRO_800R_400O are only partly covered by a layer that is partly removed during the second reaction cycle. This latter process is closer to the *classical* SMSI, but different from the self-activation process (LFRO_800R → LFRO_800R_400O).

Recently, it was reported that a RuFe alloy can be exsolved from the A-site deficient perovskite $(Pr_{0.5}Sr_{0.5})_{0.9}Fe_{0.8}Ru_{0.1}Nb_{0.1}O_{3-\delta}$ when reduced at 900 °C, and Fe further segregates from the exsolved particles to form a FeO_x shell on a RuFe core [62]. Due to the strong oxygen affinity of Fe, even small traces of oxygen in the reducing atmosphere are sufficient to drive Fe diffusion towards the surface of the alloy particle and its oxidation [63,64]. The selective removal of the FeO_x layer was not reported. Instead, the whole exsolved particles was dissolved by a high temperature O_2 treatment. In our study, Ru and Fe also co-segregate into the exsolved particle, but both species stay in the metallic state due to protection by the LaO_x layer. But even if the LaO_x capping layer is removed by mild re-oxidation at 400 °C, Fe stays in the exsolved particles and is not forming a covering FeO_x layer, as expected from its higher oxygen affinity. Instead, ruthenium oxidizes to RuO_2 at 400°C and prevents the formation of a FeO_x layer. Here, the LaO_x layer protects the Ru particles from FeO_x passivation, a novel process that may allow to form oxidized Ru particles even in the presence of dissolved Fe in the Ru particle.

We need to bear in mind that HRTEM provides only local information of some selected exsolved particles. Therefore, averaging characterization methods are mandatory to generalize the observed local changes of the exsolved particle to the entire sample. *In-situ* DRIFTS is such a method, where CO is employed as probe molecule to study the state of the catalyst surface. As revealed in Fig. 8, the CO adsorption bands do not alter from LFO to LFRO during the high temperature reduction treatment. This result is compatible with the presence of an inert coating layer LaO_x. Quite in contrast, new CO absorption bands emerge with enhanced CO intensity after re-oxidation at 400 °C, corroborating the removal of the coating layer. This conclusion is supported by the reappearance of the Ru^{3+} and a prevailing Ru^{β} signal combined with the disappearance of Ru^0 in the Ru 3*d* XPS spectra after oxidation at 400 °C, evidencing that part of Ru is re-incorporated into the perovskite structure, while most of the Ru is transformed into the 4+ oxidation state, forming (partially) RuO_2, the active phase in the catalytic propane oxidation reaction.

3.2.2. Propane combustion: Structure-performance relationships

According to Fig. 4, the Ru-free LFO sample reveals poor activity and no propane conversion is detected below 210 °C. When Ru substitutes part of the Fe in the perovskite oxide $LaFeO_3$, the catalytic performance is considerably improved and reaches a STY of 4.96 $mol_{CO2}\cdot h^{-1}\cdot kg^{-1}$ cat at 210 °C. Obviously, oxidic Ru species at the surface are the active sites of LFRO for the propane combustion reaction.

The approximately homogeneous distribution of Ru in the several hundred nanometers-sized particles of LFRO results in a low atom efficiency for Ru. With the exsolution strategy, the overall concentration of Ru in the near-surface region derived from XPS (Table 1) can be enhanced from 8% to 13%. However, the activity of the surface Ru-enriched sample LFRO_800R is surprisingly low with a STY value of 0.27 $mol_{CO2}\cdot h^{-1}\cdot kg_{cat}^{-1}$ at 210 °C. The activity is even lower than that of the original LFRO, meaning that the surface concentration of accessible Ru sites is significantly reduced.

The reason for the deactivation of LFRO after reduction at 800 °C is unveiled by HRTEM (Fig. 5(a)) and elemental mapping (Fig. 6). After high temperature reduction, mixed RuFe nanoparticles are exsolved and encapsulated by an inert LaO_x layer, so that adsorption of reactant molecules to catalytically active ruthenium sites is efficiently suppressed. This finding on the local scale is confirmed by XPS and DRIFTS experiments for the entire sample (Figs. 2 and 8). During the second light-off experiment, the STY reaches 23.5 $mol_{CO2}\cdot h^{-1}\cdot kg_{cat}^{-1}$ cat at 210 °C, manifesting a pronounced effect of self-activation of LFRO_800R catalyst.

The observed structure-activity correlation is summarized in Fig. 9. When the LFRO_800R is re-oxidized at 200 to 400 °C, the activity increases with rising re-oxidation temperature and reaches virtually always the same STY value in the second light-off experiment, independent of the applied re-oxidation temperature. From HRTEM the self-activation process of LFRO_800R can be understood on the microscopic scale. The LaO_x coating layer on exsolved RuFe particles persists in LFRO_800R_200O (0.35 $mol_{CO2}\cdot h^{-1}\cdot kg_{cat}^{-1}$) with the consequence that a similar STY value is measured as LFRO_800R (0.27 $mol_{CO2}\cdot h^{-1}\cdot kg_{cat}^{-1}$). After an oxidative treatment at 300 °C, the deformation and partial removal of the LaO_x coating layer becomes evident in HRTEM, while the activity is increased by a

Table 5
Comparison of the catalytic activity of LFRO_800R_400O for propane oxidation with those reported catalysts.

Catalyst	The feed gas	WHSV (mL·h^{-1}·kg$_{cat}^{-1}$)	Reaction temperature (°C)	STY (mol$_{CO2}$·h^{-1}·kg$_{cat}^{-1}$)	Ref.
LFRO_800R_400O	1 vol% C_3H_8, 10 vol% O_2, 89 vol% N_2	345000	210	22.3	This Work
Ru/LFO		345000	210	5.5	This Work
Ru/ZrO_2		345000	210	20	[65]
Ru/CeO_2		345000	210	23	[65]
Ru/Al_2O_3		345000	210	17	[65]
Ru/CeO_2-1	0.8 vol% C_3H_8, 2 vol% O_2, 97.8 vol% Ar	150000	170	19	[66]
Pd/CeO_2-R	0.2 vol% C_3H_8, 2 vol% O_2, 97.8 vol% Ar	300000	300	2.1	[67]
Pd/CeO_2-C		300000	300	5.0	[67]
Pd/CeO_2-O		300000	300	43.6	[67]
Pt/ Nb_2O_5		150000	200	19.2	[68]
Pt/ZrO_2		150000	200	5.2	[68]
Pt/ZnO_2		150000	200	1.3	[68]
Pt/SnO_2		150000	200	0.2	[69]
Pt//CeO_2		120000	220	2.0	[69]
Pt//CeO_2-0.5PO_x		120000	220	5.1	[69]
Pt/TiO_2	0.8 vol% C_3H_8, 9.9 vol% O_2, 89.3 vol% N_2	180000	250	39.9	[70]
1Pt/BN	0.2 vol% C_3H_8, 2 vol% O_2, 97.8 vol% N_2	80000	220	7.0	[41]
2Pt-10V/SiO_2		80000	200	30.1	[71]

factor 10 as quantified by a STY value of 3.2 mol$_{CO2}$·h^{-1}·kg$_{cat}^{-1}$ at 210 °C. Obviously, the active Ru sites of the RuFe particles start to be exposed and are accessible for reactants after re-oxidation at 300 °C. When LFRO_800R is re-oxidized at 400 °C, the inert LaO_x layer disappears in HRTEM (Fig. 5(d)), and the highest STY of 22.3 mol$_{CO2}$·h^{-1}·kg$_{cat}^{-1}$ is achieved. All re-oxidized samples reveal similar STY values at 210 °C when performing the second light-off curve as that of LFRO_800R_400O, suggesting that a treatment at 400 °C is necessary for the re-activation of the reduced sample LFRO_800R, either under an oxidative atmosphere or under propane combustion conditions. A re-oxidation temperature of 500 °C leads to a catalyst with slightly lower STY at 210 °C of 18.7 mol$_{CO2}$·h^{-1}·kg$_{cat}^{-1}$, indicating that an oxidation treatment at 400 °C is at the optimum.

The catalytically active phase of LFRO_800R_400O consists of exsolved RuFe particles (with 80% Ru, EDS: Fig. 6) that are not covered by a passivating LaO_x layer (HRTEM, Fig. 5) and that further oxidize (XPS, Fig. 7). The catalytic activity of LFRO_800R_400O is five times higher than that of LFRO since the surface concentration of accessible Ru species is increased. It is also compared with other reported catalysts in Table 5 [42,65–71], the benchmark catalysts for 5 mol% Ru supported on CeO_2 (30 m^2·g^{-1}), γ-Al_2O_3 (100 m^2·g^{-1}) and ZrO_2 (35 m^2·g^{-1}) reporting STY values of 23, 20 and 17 mol$_{CO2}$·h^{-1}·kg$_{cat}^{-1}$ at 210 °C for the same reaction conditions, respectively [65]. A similar catalytic performance is achieved with LFRO_800R_400O at 210 °C (22.3 mol$_{CO2}$·h^{-1}·kg$_{cat}^{-1}$), although the BET surface area of 10 m^2·g^{-1} is significantly lower than those of the benchmark catalysts. In general, the catalytic combustion of short-chain alkane is conducted with Pd and Pt-based catalysts. However, Ru-based catalysts have demonstrated to be a promising and less expensive alternative to Pt and Pd for the elimination of propane.

4. Conclusions

Careful redox treatment of LFRO allows us to control the exsolution process of Ru, forming highly dispersed, socketed Ru-based oxide particles that can be highly active in the total propane oxidation. The exsolution process is scrutinized by employing a variety of dedicated experimental techniques. With HRTEM and elemental mapping the details of the transformation process of single exsolved particles are studied, while with averaging methods including XRD, XPS, Raman and DRIFTS the conclusions drawn on local scale can be transferred to the entire sample. High temperature reduction at 800 °C of LFRO results in the formation of mixed RuFe nanoparticles that are covered and hence de-activated by a conforming LaO_x overlayer. Under mild oxidizing reaction conditions at temperatures of 400 °C the LaO_x layer can be selectively removed likely by re-dissolution of La back into LFRO in the surface-near region. During this mild oxidation process the peeled RuFe particles transform into RuO_2 with no indication of a separate FeO_x phase. These oxidized exsolved RuFe particles are shown to be highly active in the catalytic propane combustion with activities exceeding those of benchmark catalysts and 5 mol% Ru supported on LFO.

Notes

The authors declare no competing financial interest.

Supporting Information

Supporting information is available in the online version of this article.

Acknowledgment

Yu Wang acknowledges the China Scholarship Council for the Joint-Ph.D. program with the Institute of Physical Chemistry of the Justus-Liebig-University Giessen. We acknowledge support from the Center for Materials Research at the JLU. H.O. and L.G. acknowledge funding by the German Research Foundation (DFG, Deutsche Forschungsgemeinschaft - 493681475).

References

[1] R. Schlögl, *Angew. Chem. Int. Ed.,* **2015**, 54, 3465–3520.
[2] B. C. Gates, *Chem. Rev.,* **1995**, 95, 511–522.
[3] N. Zheng, G. D. Stucky, *J. Am. Chem. Soc.,* **2006**, 128, 14278–14280.
[4] Y. Nishihata, J. Mizuki, T. Akao, H.Tanaka, M. Uenishi, M. Kimura, T. Okamoto, N. Hamada, *Nature,* **2002**, 418, 164–167.
[5] K. Kousi, C. Tang, I. S. Metcalfe, D. Neagu, *Small,* **2021**, 17, 2006479.
[6] D. Neagu, T. S. Oh, D. N. Miller, H. Menard, S. M. Bukhari, S. R. Gamble, R. J. Gorte, J. M. Vohs, J. T. S. Irvine, *Nat. Commun.,* **2015**, 6, 8120.
[7] T. S. Oh, E. K. Rahani, D. Neagu, J. T. S. Irvine, V. B. Shenoy, R. J. Gorte, J. M. Vohs, *J. Phys. Chem. Lett.,* **2015**, 6, 5106–5110.
[8] M. A. Naeem, P. M. Abdala, A. Armutlulu, S. M. Kim, A. Fedorov, C. R. Muller, *ACS Catal.,* **2020**, 10, 1923–1937.
[9] Y. Song, H. Li, M. Xu, G. Yang, W. Wang, R. Ran, W. Zhou, Z. Shao, *Small,* **2020**, 16, 2001859.
[10] B. Hua, N. Yan, M. Li, Y. Zhang, Y. Sun, J. Li, T. Etsell, P. Sarkar, K. Chuang, J. Luo, *Energy Environ. Sci.,* **2016,** 9, 207–215.
[11] M. B. Katz, G. W. Graham, Y. Duan, H. Liu, C. Adamo, D. G. Schlom, X. Pan, *J. Am. Chem. Soc.,* **2011**, 133, 18090–18093.
[12] J. Zhang, M. R. Gao, J. L. Luo, *Chem. Mater.,* **2020**, 32, 5424–5441.
[13] J. K. Kim, S. Kim, S. Kim, H. J. Kim, K. Kim, W. Jung, J. W. Han, *Adv. Mater.,* **2023**, 35, 2203370.
[14] Y. Yang, J. Li, Y. Sun, *Chem. Eng. J.,* **2022**, 440, 135868.
[15] M. A. Pena, J. L. G. Fierro, *Chem. Rev.,* **2001**, 101, 1981–2018.
[16] S. She, Y. Zhu, X. Wu, Z. Hu, A. Shelke, W. Pong, Y. Chen, Y. Song, M. Liang, C. Chen, H. Wang, W. Zhou, Z. Shao, *Adv. Funct. Mater.,* **2022**, 32, 2111091.
[17] C. Tang, K. Kousi, D. Neagu, I. S. Metcalfe, *Chem. Eur. J.,* **2021**, 27, 6666–6675.
[18] O. Kwon, S. Joo, S. Choi, S. Sengodan, G. Kim, *J. Phys. Energy*, **2020**, 2, 032001.
[19] Y. Gao, J. Wang, Y. Lyu, K. Lam, F. Ciucci, *J. Mater. Chem. A,* **2017**, 5, 6399–6404.
[20] B. Zhao, B. Yan, Z. Jiang, S. Yao, Z. Liu, Q. Wu, R. Ran, S. D. Senanayake, D. Weng, J. G. Chen, *Chem. Commun.,* **2018**, 54, 7354–7357.
[21] R. Glaser, T. Zhu, H. Troiani, A. Caneiro, L. Mogni, S. Barnett, *J. Mater. Chem. A,* **2018**, 6, 5193–5201.
[22] H. Lv, L. Lin, X. Zhang, R. Li, Y. Song, H. Matsumoto, N. Ta, C. Zeng, Q. Fu, G. Wang, X. Bao, *Nat. Commun.,* **2021**, 12, 5665.
[23] N. Hou, T. Yao, P. Li, X. Yao, T. Gan, L. Fan, J. Wang, X. Zhi, Y. Zhao, Y. Li, *ACS Appl. Mater. Interfaces,* **2019**, 11, 6995–7005.
[24] J. Wang, L. Fu, J. Yang, Z. Liu, J. Myung, K. Wu, *Energy Fuels,* **2022**, 36, 12236–12244.
[25] B. Koo, K. Kim, J. K. Kim, H. Kwon, J. W. Han, W. Jung, *Joule,* **2018**, 2, 1476–1499.
[26] Z. Teng, Z. Xiao, G. Yang, L. Guo, X. Yang, R. Ran, W. Wang, W. Zhou, Z. Shao, *Mater. Today Energy,* **2020**, 17, 100458.
[27] J. Liu, W. Su, J. Rick, S. Yang, C. Pan, J. Lee, J. Chen, B. Hwang, *Catal. Sci. Technol.,* **2016**, 6, 3449–3456.
[28] X. Cao, L. Ke, K. Zhao, X. Yan, X. Wu, N. Yan, *Chem. Mater.,* **2022**, 34, 10484–10494.
[29] W. Lee, J. W. Han, Y. Chen, Z. Cai, B. Yildiz, *J. Am. Chem. Soc.,* **2013**, 135, 7909–7925.
[30] B. P. Barbero, J. A. Gamboa, L. E. Cadus, *Appl. Catal. B,* **2006**, 65,

Graphical Abstract

Chin. J. Catal., 2023, 54: 250–264 doi: 10.1016/S1872-2067(23)64547-4

Unveiling the self-activation of exsolved $LaFe_{0.9}Ru_{0.1}O_3$ perovskite during the catalytic total oxidation of propane

Yu Wang, Jaime Gallego, Wei Wang, Phillip Timmer, Min Ding, Alexander Spriewald Luciano, Tim Weber, Lorena Glatthaar, Yanglong Guo *, Bernd M. Smarsly *, Herbert Over *
East China University of Science and Technology, China; Justus Liebig University, Germany

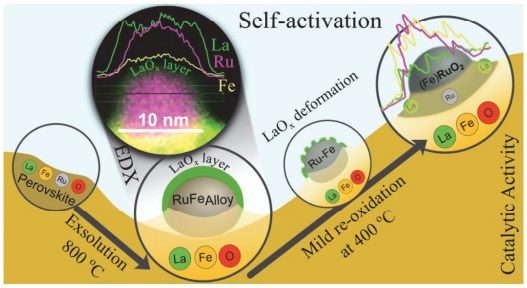

High temperature reduction at 800 °C of $LaFe_{0.9}Ru_{0.1}O_3$ (LFRO) results in the formation of exsolved RuFe nanoparticles that are passivated by a conforming La-based layer and that can be activated by a mild oxidative treatment at 400 °C.

21–30.
[31] Y. Yang, L. Zhang, H. Guo, Z. Ding, W. Wang, J. Li, L. Zhou, X. Tu, Y. Qiu, G. Chen, Y. Sun, *ACS Appl. Mater. Interfaces,* **2022**, 14, 30704–30713.
[32] Z. Wang, Z. Huang, J. T. Brosnhan, S. Zhang, Y. Guo, Y. Guo, L. Wang, W. Zhan, *Environ. Sci. Technol.,* **2019**, 53, 5349–5358.
[33] H. Hao, Z. Liu, F. Zhao, W. Li, *Renewable Sustain. Energy Rev.,* **2016**, 62, 521–533.
[34] H. Xin, L. Lin, R. Li, D. Li, T. Song, R. Wu, Q. Fu, X. Bao. *J. Am. Chem. Soc.,* **2022**, 144, 4874–4882.
[35] H. Tang, Y. Su, B. Zhang, A. F. Lee, M. A. Isaacs, K. Wilson, L. Li, Y. Ren, J. Huang, M. Haruta, B. Qiao, X. Lin, C. Jin, D. Su, J. Wang, T. Zhang, *Sci. Adv.,* **2017**, 3, e1700231.
[36] Y. Jiang, Z. Geng, L. Yuan, Y. Sun, Y. Cong, K. Huang, L. Wang, W. Zhang, *ACS Sustainable Chem. Eng.*, **2018**, 6, 11999–12005.
[37] P. Timmer, T. Weber, L. Glatthaar, H. Over, *Inorganics,* **2023**, 11, 102.
[38] O. Khalid, A. Spriewald Luciano G. Drazic, H. Over, *ChemCatChem,* **2021**, 13, 3983–3994.
[39] Y. Chin, C. Buda, M. Neurock, E. Iglesia, *J. Am. Chem. Soc.,* **2011**, 133, 15958–15978.
[40] Y. Chin, C. Buda, M. Neurock, E. Iglesia, *J. Am. Chem. Soc.,* **2013**, 135, 15425–15442.
[41] Y. Liu, X. Li, W. Liao, A. Jia, Y. Wang, M. Luo, J. Lu, *ACS Catal.,* **2019**, 9, 2, 1472–1481.
[42] E. G. Rini, A. Paul, M. Nasir, R. Amin, M. K. Gupta, R. Mittal, S. Sen, *J. Alloys Compd.,* **2020**, 830, 154594.
[43] H. Chen, C. Lim, M. Zhou, Z. He, X. Sun, X. Li, Y. Ye, T. Tan, H. Zhang, C. Yang, J. W. Han, Y. Chen, *Adv. Sci.,* **2021**, 8, 2102713.
[44] M. C. Weber, M. Guennou, H. J. Zhao, J. Iniguez, R. Vilarinho, A. Almeida, J. A. Moreira, J. Kreisel, *Phys. Rev. B,* **2016**, 94, 214103.
[45] K. Sultan, M. Ikram, K. Asokan, *Vacuum,* **2014**, 99, 251–258.
[46] W. Y. Lee, H. J. Yun, J. W. Yoon, *J. Alloys Compd.,* **2014**, 583, 320–324.
[47] W. Gu, J. Liu, M. Hu, F. Wang, Y. Song, *ACS Appl. Mater. Interfaces,* **2015**, 7, 26914–26922.
[48] D. J. Morgan, *Surf. Interface Anal.,* **2015**, 47, 1072–1079.
[49] H. Over, *Chem. Rev.,* **2012**, 112, 3356–3426.
[50] F. Zaera, *ChemCatChem,* **2012**, 4, 1525–1533.
[51] F. C. Meunier, *J. Phys. Chem. C,* **2021**, 125, 21810–21823.
[52] S. Y. Chin, C. T. Williams, M. D. Amiridis, *J. Phys. Chem. B,* **2006**, 110, 871–882.
[53] J. T. Kiss, R. D. Gonzalez, *J. Phys. Chem.,* **1984**, 88, 892–897.
[54] A. Farkas, G. C. Mellau, H. Over, *J. Phys. Chem. C,* **2009**, 113, 14341–14355.
[55] T. Tan, Z. Wang, M. Qin, W. Zhong, J. Hu, C. Yang, M. Liu, *Adv. Funct. Mater.,* **2022**, 32, 2202878.
[56] Y. Cong, Z. Geng, Q. Zhu, H. Hou, X. Wu, X. Wang, K. Huang, S. Feng, *Angew. Chem. Int. Ed.,* **2021**, 60, 23380–23387.
[57] Y. Liang, Y. Cui, Y. Chao, N. Han, J. Sunarso, P. Liang, X. He, C. Zhang, S. Liu, *Nano Res.,* **2022**, 15, 6977–6986.
[58] J. Wang, A. Kumar, J. L. Wardini, Z. Zhang, H. Zhou, E. J. Crumlin, J. T. Sadowski, K. B. Woller, W. J. Bowman, J. M. LeBeau, B. Yildiz, *Nano Lett.,* **2022**, 22, 5401–5408.
[59] S. J. Tauster, S. C. Fung, R. T. K. Baker, J. Horsley, *Science,* **1981**, 211, 1121–1125.
[60] A. Beck, X. Huang, L. Artiglia, M. Zabilskiy, X. Wang, P. Rzepka, D. Palagin, M. G. Willinger, J. A. van Bokhoven, *Nat. Commun.,* **2020**, 11, 3220.
[61] T. Pu, W. Zhang, M. Zhu, *Angew. Chem. Int. Ed.,* **2023**, 62, e202212278.
[62] M. Qin, Y. Xiao, H. Yang, T. Tan, Z. Wang, X. Fan, C. Yang, *Appl. Catal. B,* **2021**, 299, 120613.
[63] S. Prabhudev, M. Bugnet, G. Z. Zhu, C. Bock, G. A. Botton, *ChemCatChem,* **2015**, 7, 3655–3664.
[64] H. Zhu, Z. Wu, D. Su, G. M. Veith, H. Lu, P. Zhang, S. Chai, S. Dai, *J. Am. Chem. Soc.*, **2015**, 137, 10156–10159.
[65] Z. Wang, W. Wang, O. Khalid, T. Weber, A. Spriewald Luciano, W. Zhan, B. M. Smarsly, H. Over, *ChemCatChem,* **2022**, 14, e202200149.
[66] Z. Hu, Z. Wang, Y. Guo, L. Wang, Y. Guo, J. Zhang, W. Zhan, *Environ. Sci. Technol.,* **2018**, 52, 9531–9541.
[67] Z. Hu, X. Liu, D. Meng, Y. Guo, Y. Guo, G. Lu, *ACS Catal.,* **2016**, 6, 2265–2279.
[68] Z. Huang, J. Ding, X. Yang, H. Liu, P. Song, Y. Guo, Y. Guo, L. Wang, W. Zhan, *Environ. Sci. Technol.,* **2022**, 56, 17278–17287.
[69] Z. Huang, S. Cao, J. Yu, X. Tang, Y. Guo, Y. Guo, L. Wang, S. Dai, W. Zhan, *Environ. Sci. Technol.,* **2022**, 56, 9661–9671.
[70] M. S. Avila, C. I. Vignatti, C. R. Apesteguia, T. F. Garetto, *Chem. Eng. J.,* **2014**, 241, 52-59.
[71] W. Liao, Y. Liu, P. Zhao, B. Cen, C. Tang, A. Jia, J. Lu, M. Luo, *Appl. Catal. A,* **2020**, 590, 117337.

析出型$LaFe_{0.9}Ru_{0.1}O_3$钙钛矿催化剂在丙烷催化氧化反应中的自活化现象

王　宇[a,b], Jaime Gallego [b,c], 汪　炜[a,b], Phillip Timmer [b], 丁　敏[a], Alexander Spriewald Luciano [b], Tim Weber [b], Lorena Glatthaar [b], 郭杨龙[a,*], Bernd M. Smarsly [b,*], Herbert Over [b,*]

[a]华东理工大学化学与分子工程学院, 工业催化研究所, 绿色化工与工业催化全国重点实验室, 上海200237, 中国
[b]尤斯图斯-李比希大学物理化学研究所, 吉森, 德国
[c]尤斯图斯-李比希大学材料研究中心, 吉森, 德国

摘要: 负载型贵金属催化剂在能源转化和环境污染控制等领域有广泛应用. 相对于采用传统方法制备负载型贵金属催化剂, 还原析出策略在控制贵金属的粒径, 增强贵金属与载体相互作用方面具有独特的优势. 但是在高温还原气氛下, 贵金属析出的同时往往伴随着母体结构中其它元素的析出, 这会对催化剂的性能产生较大影响. 因此, 理解催化剂在还原气氛下以及后续反应条件下的结构演变, 对于催化剂的设计及制备具有重要意义.

本文通过800 °C还原Ru掺杂的$LaFe_{0.9}Ru_{0.1}O_3$ (LFRO)钙钛矿前驱体制备了贵金属析出的LFRO催化剂(LFRO_800R), 并用于丙烷催化氧化反应. 活性测试结果表明, 析出Ru催化剂的丙烷氧化性能远远低于原始的LFRO. 当第一次反应结束, 催化剂床层温度降至室温后再次评价其性能, LFRO_800R催化剂会发生“自活化”现象, 在210 °C下催化丙烷反应速率达到

了22.3 $mol_{CO2}·h^{-1}·kg_{cat}^{-1}$, 是该温度下贵金属未析出LFRO催化剂的5倍, 反应10 h后仍表现出较高的稳定性. 为进一步研究LFRO_800R在丙烷氧化反应中发生“自活化”的原因, 在不同温度对LFRO_800R进行氧化处理, 发现经过400 °C氧化后得到的LFRO_800R_400O表现出最佳的丙烷催化活性. 采用高分辨透射电镜、能量散射谱、漫反射红外傅立叶变换光谱、扫描电镜、X射线衍射、Raman光谱和X射线光电子能谱等方法对催化剂进行了表征. 结果表明, 经过800 °C还原预处理, 伴随着Ru从LFRO钙钛矿结构的体相中析出到表面, 钙钛矿A位元素La也会析出并在RuFe(Ru占据主导)颗粒表面形成一层LaO_x覆盖层, 阻碍了反应物分子在活性位点Ru上的吸附与活化, 导致LFRO_800R在丙烷完全氧化反应中的低温区间表现出失活的现象. 而在400 °C的氧化气氛处理下, 该LaO_x包裹层会从析出颗粒的表面完全去除, 伴随着少部分界面处的Ru重新进入钙钛矿结构, 大量有活性的Ru物种被暴露出来, 因此催化剂表现出较好的丙烷催化氧化性能. 活化后的LFRO_800R_400O催化剂中Ru的平均粒径为12 nm, 远远小于负载型Ru/LFO_800R_400O催化剂的34 nm, 说明还原析出策略在控制贵金属粒径方面有优势.

综上, 本文揭示了还原析出策略制备的Ru基钙钛矿催化剂的失活原因以及后续的氧化气氛中“自活化”的原因, 为理性设计与制备高效的析出型贵金属催化剂提供了借鉴.

关键词: $LaFe_{0.9}Ru_{0.1}O_3$钙钛矿; 溶出; 氧化还原预处理; RuO_2; 丙烷完全催化氧化

收稿日期: 2023-08-30. 接受日期: 2023-10-19. 上网时间: 2023-11-15.

*通讯联系人. 电子信箱: Herbert.Over@phys.Chemie.uni-giessen.de (H. Over), Bernd.Smarsly@phys.Chemie.uni-giessen.de (B. M. Smarsly), ylguo@ecust.edu.cn (郭杨龙).

基金来源: 国家重点研发计划(2022YFB3504200); 国家自然科学基金(22076047, 21976057, U21A20326); 111工程(B08021); 中央高校基本科研业务费专项资金.

2.2 Publication 2: Microscopic Insight into Ruthenium Exsolution from $LaFe_{0.9}Ru_{0.1}O_3$ Perovskite

As demonstrated in publication 1, the high temperature reduction at 800 ℃ exsolves the Ru from LFRO ($LaFe_{0.9}Ru_{0.1}O_3$), encapsulated by a confirming LaO_x coating layer that can be selectively removed by oxidative treatment at 400 ℃. However, there are still some interesting questions left. For instance, At which temperature Ru exsolved? At which temperature La coating layer formed? Are there any correlations between Ru exsolution and La segregation? In order to answer these questions, LFRO reduced at different temperature range from 300 – 800 ℃ are systematically investigated in this publication. The *in-situ* and *ex-situ* XPS results confirm that the Ru exsolved already at a reduction temperature of 400 ℃. When temperature lower the 600 ℃, Ru exsolution is strictly confined in the near-surface zone (XPS detection region, about 2 – 3 nm in depth) while further increase the reduction temperature triggers the exsolution of Ru from bulk as well as the co-segregation of LaO_x. At reduction temperatures of 700 ℃ or higher, the co-segregated LaO_x totally covering the exsolved Ru nanoparticles. Meanwhile, Ru exsolution is revealed to proceeds the sequence of $Ru^{3+} \rightarrow Ru^{\beta} \rightarrow Ru^0$ where Ru^{β} serves as a reaction intermediate with an oxidation state lower than +3.

I designed the concept and performed the experiment under the supervision of H. Over and J. Gallego. P. Paciok performed the *in-situ* TEM. L. Pielsticker and W. Hetaba measured the *in-situ* XPS. L. Glatthaar carried out the *ex-situ* XPS measurement. W. Wang, A. Spriewald-Luciano, M. Ding helped in the data analysis and scientific discussion. I wrote the draft and H. Over, J. Gallego, Y. Guo and B. M. Smarsly revised and polished the manuscript.

Reprinted with permissions from Wang, Y.; Paciok, P.; Pielsticker, L.; Wang, W.; Spriewald-Luciano, A.; Ding, M.; Glatthaar, L.; Hetaba, W.; Guo, Y.; Gallego, J.; Smarsly, B. M.; Over, H. Microscopic Insight into Ruthenium Exsolution from $LaFe_{0.9}Ru_{0.1}O_3$ Perovskite, *Chem. Mater.* **2024**, XXXX, XXX–XXX. Copyright 2024 American Chemical Society

Doi: 10.1021/acs.chemmater.4c01084

CHEMISTRY OF MATERIALS

pubs.acs.org/cm Article

Microscopic Insight into Ruthenium Exsolution from $LaFe_{0.9}Ru_{0.1}O_3$ Perovskite

Yu Wang, Paul Paciok, Lukas Pielsticker, Wei Wang, Alexander Spriewald Luciano, Min Ding, Lorena Glatthaar, Walid Hetaba, Yanglong Guo,* Jaime Gallego,* Bernd M. Smarsly,* and Herbert Over*

Cite This: https://doi.org/10.1021/acs.chemmater.4c01084 Read Online

ACCESS | Metrics & More | Article Recommendations | Supporting Information

Downloaded via UNIV GIESSEN on June 12, 2024 at 17:25:59 (UTC).
See https://pubs.acs.org/sharingguidelines for options on how to legitimately share published articles.

ABSTRACT: Metal exsolution is a smart strategy that allows modification and enrichment of a material's surface with highly active catalytic phases, thus offering the possibility to fine-tune the surface chemical composition. We study the exsolution of Ru from a perovskite solid solution $LaFe_{0.9}Ru_{0.1}O_3$ (LFRO) to form Ru nanoparticles and their passivation by a conforming LaO_x layer by applying a variety of *in situ* techniques, including TEM and XPS, in combination with *ex situ* infrared and Raman spectroscopy, but most notably by utilizing the catalytic propane combustion to probe the formation of the passivating LaO_x layer. During the Ru exsolution process, Ru^{3+} in LFRO is reduced first to the Ru^{β} species and subsequently into a Ru^0 species, evidencing the exsolution of Ru particle. The transformation of $Ru^{3+} \rightarrow Ru^{\beta}$ proceeds already below 300 °C and is correlated with the formation of oxygen vacancies under a reductive atmosphere. The subsequent transformation of Ru^{β} toward Ru^0 needs at least a reduction temperature of 400 °C that is likely to be determined by the diffusion of Ru^{3+} from the near-surface region of LFRO toward the surface. Only above 600 °C ruthenium cations from the bulk of LFRO are exsolved, leading to the further growth of Ru particles. Around 600 °C, the exsolution of Ru particles is accompanied by the formation of a covering LaO_x layer. We propose that La segregation and precipitation as surface LaO_x are driven by the overstoichiometry of La in LFRO after Ru exsolution.

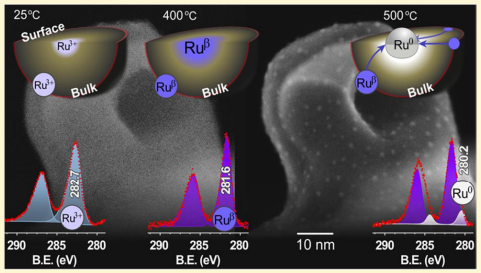

1. INTRODUCTION

The exsolution process of precious metal ions from a solid oxide solution is a promising approach to stabilize catalytically active nanoparticles (NPs) at the surface via reductive treatment at high temperatures.[1−4] Exsolution is able to control the size distribution of metal nanoparticles (NPs) that are stabilized against sintering by anchoring the NP into the parent matrix[5,6] so that catalyst's lifetime can be significantly extended in high-temperature reactions, including catalytic reforming reactions or the anode reaction of solid oxide fuel cells.[7−10] Sometimes, the exsolution process of the target element is accompanied by the coexsolution of another element, forming bimetallic particles on the surface with unique properties.[11,12] Upon high-temperature oxidation, the exsolved NP is able to dissolve back into the solid oxide solution, a process that can be utilized in the self-regeneration of the catalyst.[13,14]

High-temperature reduction in 4 vol % H_2 at 800 °C of $LaFe_{0.9}Ru_{0.1}O_3$ (LFRO, LFRO_800R) has shown to lead to the exsolution of ruthenium particles that are passivated by a conforming LaO_x layer.[15] The covering LaO_x layer leads to a substantial activity loss in catalytic propane combustion with respect to LFRO. After reoxidation treatment at 400 °C or a second reaction cycle in the conversion of propane combustion up to 400 °C, the LaO_x layer is removed (so-called self-activation) so that the activity of exsolved Ru in catalytic propane combustion is substantially enhanced.[15]

There are still some important open questions left: At which temperature does the exsolution of Ru set in, and at which temperature does the covering passivation layer form? In order to answer these questions, a series of LFRO samples are prepared by reducing LFRO at various temperatures ranging from 300 to 800 °C, and the catalytic activity, together with other structural and morphological properties, are studied before and after reoxidation at 400 °C. We employ a variety of experimental characterization methods to follow the surface evolution and development of exsolved Ru particles and the

Received: April 12, 2024
Revised: May 31, 2024
Accepted: June 3, 2024

ACS Publications
© XXXX The Authors. Published by American Chemical Society

https://doi.org/10.1021/acs.chemmater.4c01084
Chem. Mater. XXXX, XXX, XXX−XXX

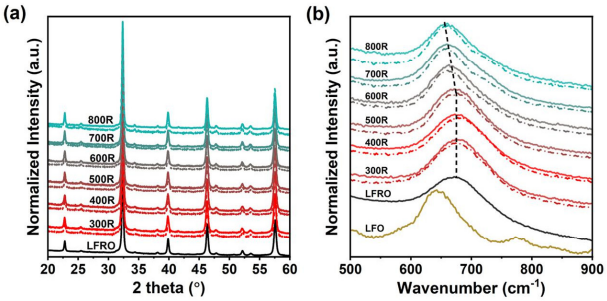

Figure 1. (a) XRD and (b) Raman results of LFO, as-synthesized, and different temperature-reduced LFRO perovskites (solid lines). Each of the reduced LFRO samples is subsequently oxidized at 400°C (dashed lines).

formation/removal of the passivating covering LaO_x layer, including *in situ* TEM, *in situ* XPS, *in situ* DRIFTS, and most notably the catalytic activity in propane combustion serving as a test reaction. The formation and removal of the passivating LaO_x layer from the exsolved Ru particles lead to pronounced hysteresis in the repeadly taken propane conversion curves.

From this study, we conclude that reduction of Ru^{3+} in LFRO perovskites to Ru^0 commences at 400 °C under reducing conditions. The Ru exsolution is restricted in the near-surface zone when reduced at 500 °C, while the bulk exsolution and LaO_x segregation start at 600 °C.

2. MATERIALS AND METHODS

2.1. Sample Preparation. LFRO, a perovskite oxide powder with a nominal chemical composition of $La_1Fe_{0.9}Ru_{0.1}O_3$, is prepared by using the citric sol−gel method. The following steps are employed for the synthesis. 4 mmol of $La(NO_3)_3{\cdot}6H_2O$, 3.6 mmol of $Fe(NO_3)_3{\cdot}9H_2O$, and 0.4 mmol of $Ru(NO)(NO_3)_3$ are dissolved in 50 mL of distilled water. Subsequently, 12 mmol of citric acid and 24 mmol ethylene glycol are added to the solution under continuous stirring at 80 °C. The gel containing the LFRO precursor gradually forms during water evaporation. After drying at 120 °C overnight, the material is ground and calcined with a heating rate of 3 °C·min^{-1} at 750 °C for 3 h in a muffle oven to obtain the perovskite LFRO.

To evaluate the effect of exsolution temperature on the properties of LFRO, we produce a series of samples from the same batch by pretreating the as-synthesized LFRO in 4 vol % H_2 balanced by an Ar atmosphere at various temperatures ranging from 300 to 800 °C for 3 h. The resulting samples are designated as LFRO_TR, where T represents the specific reduction temperature. For example, LFRO_300R means LFRO perovskite is reduced at 300 °C for 3 h. With various characterization methods (Section 2.2), the exsolution process of Ru and the formation of the passivating LaO_x layer are studied. After thorough characterization, all LFRO_TR samples are mildly reoxidized at 400 °C in 10 vol % O_2 balanced by Ar for 30 min, denoted as LFRO_TR_400O, to remove the LaO_x layer.

2.2. Sample Characterization. The powder XRD measurement is performed using an X-ray diffractometer (Panalytical X'Pert PRO) with a step size of 0.013° using a PIXcel2D 1 × 1 detector. The diffraction patterns are collected in the 2θ range of 20−60° with a Cu−K_α radiation source (λ = 1.5418 Å). Raman spectra of the investigated perovskite are measured with a Senterra spectrometer of Bruker Optics with a laser wavelength of 632.8 nm at the power of 2 mW. The spectra are collected with 200 coadditions and 8 s of integration time.

In-situ near-ambient pressure X-ray photoelectron spectroscopy (XPS) experiments are conducted in an ultrahigh vacuum system (Specs GmbH) equipped with a Phoibos NAP-150 hemispherical analyzer and with a monochromatic Al−Kα source. The perovskite oxide is pretreated in 0.5 mbar O_2 at 600 °C for 30 min to eliminate the adventitious carbon. During the reduction process, H_2 is introduced into the sample chamber with mass flow control, and the pressure is controlled at 1 mbar during the measurement. The sample is kept at each temperature (300, 400, 500, 600, and 700 °C) for 1 h after which the XP spectra are collected.

Ex situ XPS spectra of the as-prepared LFRO samples, different temperature-reduced ones, and corresponding reoxidized samples are collected by a PHI 5000 VersaProbe II instrument (Physical Electronics GmbH) with Al−Kα radiation (1486.7 eV). During the data analysis, all of the spectra are calibrated by the adventitious carbon at a binding energy of 284.8 eV, employing Casa XPS version 2.3.17 software.

Morphological information on the investigated samples is revealed by scanning transmission electron microscopy (STEM) using a Thermo Fisher Talos F200X microscope that is equipped with an FEG electron source operated at 200 kV. EDS mapping is conducted using 4 in-column Super-X detectors. The powder is suspended in ethanol by sonication, and a drop is deposited on a lacey carbon TEM grid.

The environmental STEM Hitachi HF5000 used for the *in situ* experiments under reductive gas atmospheres is equipped with an energy dispersive spectroscopy unit (Oxford Instruments Aztec Energy TEM Advanced EDX System Ultrim TLE), a postcolumn energy filter system (CEOS CEFID), and a TVIPS TemCam XF416 camera. A probe-corrected microscope is operated at an acceleration voltage of 200 kV and a semiconvergence angle of 28 mrad is used. After drop-casting a catalyst suspension on *in situ* heating chips (Norcada, HTN 0101H), the chips are mounted in a Hitachi *in situ* heating holder and transferred to the microscope. Before the required temperature is set at a heating rate of 3 °C·s^{-1}, the desired gas is introduced into the microscope column at 3 mL·min^{-1} using a mass flow controller.

In-situ diffuse-reflectance infrared Fourier transform spectra (DRIFTS) of CO adsorption are performed on a Bruker Vertex 70 V, offering a spectral resolution of 4 cm^{-1}.[16] The different temperature-reduced samples are *in-situ* treated in 4 vol % H_2 balanced by Ar at 300 °C for 30 min. After cooling down to room temperature, 2 vol % CO balanced by Ar is admitted to the cell with a total flow of 50 mL·min^{-1} and DRIFT spectra are acquired. The as-synthesized LFRO and the temperature-reduced samples are *in-situ* reoxidized in 10 vol % O_2 balanced by Ar at 300 °C for 30 min. Subsequently, another set of CO-DRIFT spectra is acquired.

2.3. Evaluation of Catalytic Performance. To evaluate the catalytic propane combustion performance of the perovskites, a home-built flow reactor is used that comprises a gas supply, a quartz reactor, a furnace, and a nondispersive infrared sensor (Saxon Junkalor INFRALYT 80).[17] The characteristic absorption bands for C_3H_8 and CO_2 are around 2960 and 2349 cm^{-1}, respectively, so their concentration in the outlet gas can be determined using the Beer−Lambert law. The reactor is fed with a gas mixture containing 89 vol

https://doi.org/10.1021/acs.chemmater.4c01084
Chem. Mater. XXXX, XXX, XXX−XXX

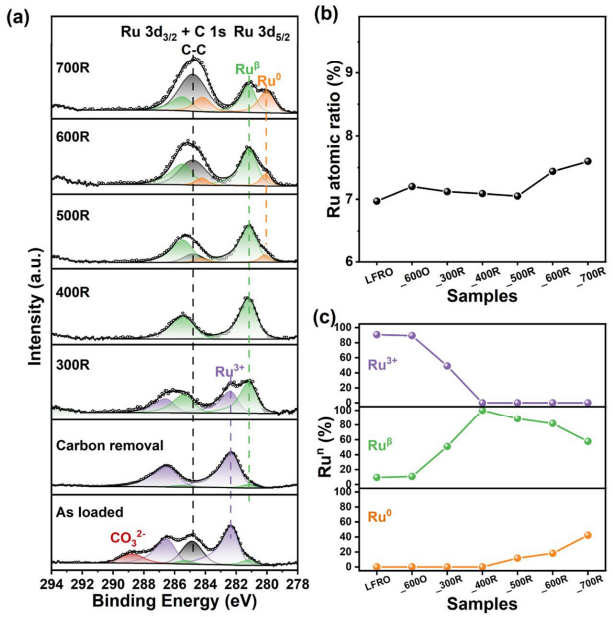

Figure 2. Fitted C 1s + Ru 3d *in-situ* XP spectra of (a) the as-loaded LFRO adventitious carbon removed LFRO_600O (pretreated under 0.5 mbar O_2 at 600 °C for 1 h), different temperature-reduced LFRO (from 300 to 700 °C under 1 mbar H_2 for 1 h). (b) The derived Ru content and (c) Ru state distribution of the corresponding samples.

% N_2 (Linde), 10 vol % O_2 (Linde), and 1 vol % C_3H_8 (Nippon Gases) at a total flow rate of 100 mL·min^{-1} under standard conditions.

Typically, 20 mg of the Ru-containing perovskite oxide is diluted with 40 mg of inert quartz sand, achieving a weight hourly space velocity (WHSV) of 34,500 mL·g^{-1}·h^{-1}. For the light-off curves (conversion curves), the sample is heated from room temperature to 400 °C with a ramping rate of 1 °C·min^{-1}. After naturally cooling to room temperature, the sample is heated again in the reaction environment without removal from the quartz tube; three consecutive reaction cycles are conducted. The propane conversion, denoted as X, is calculated using the formula: $X = 1\text{-}c(C_3H_8)/c_0(C_3H_8)$, where $c(C_3H_8)$ represents the volumetric concentration of propane in the outlet gas and $c_0(C_3H_8)$ represents the maximum volumetric concentration of propane in the gas mixture. To verify complete propane combustion, the volumetric concentration of CO_2 is also monitored to cross-check the calculated conversion.

3. RESULTS AND DISCUSSION

3.1. Experimental Results. The structure evolution of LFRO under reductive treatment at different temperatures (from 300 to 800 °C) is followed by powder XRD (Figure 1a, solid lines). For as-prepared LFRO, the diffraction patterns are consistent with the reported orthorhombic $LaFeO_3$ (JCPDS No. 88-0641), and no other reflections for extra crystalline phases are discernible (cf. Figure S1). When LFRO is treated at different temperatures in 4 vol % H_2 for 3 h, all of the reduced samples show similar XRD patterns to LFRO, and no other crystalline phases are detected, corroborating the high structural stability of the LFRO sample under such reducing atmospheres. The absence of an exsolved Ru-based phase indicates its relatively small crystallite size or low concentration that is below the detection limit of the XRD. In Figure 1a (dash lines), we summarize the XRD patterns of the reduced samples after mild reoxidation treatment at 400 °C (10 vol % O_2 for 3 h). Again, no appreciable changes are observed in the XRD patterns.

Raman spectroscopy (cf. Figure 1b, solid lines) can provide information about the exsolution process and bulk properties of LFRO before and after reduction. The Raman spectrum of LFO ($LaFeO_3$) is consistent with that reported in the literature, confirming the successful synthesis of the perovskite oxide.[18] The incorporation of Ru into $LaFeO_3$ induces lattice strain associated with inhomogeneous distortion of the FeO_6 octahedron, which leads to the blue shift of the spectral feature at 670 cm^{-1} and a substantial broadening of the signals.[19] When the sample is exposed to hydrogen at temperatures up to 500 °C, practically no changes are observed in the Raman spectra. Above a reduction temperature of 500 °C, the Raman peak shifts gradually to lower wavenumbers, indicating that the local distortions of the FeO_6 octahedrons are partially relieved. This experiment suggests that noticeable Ru exsolution from bulk LFRO commences above 500 °C. The Raman spectra of these reduced samples are not affected by mild reoxidation (cf. Figure 1b, dashed lines) regardless of the applied reduction temperature. The reoxidation experiment suggests that the exsolved Ru species do not dissolve back into the bulk of the perovskite structure. The potential formation of a covering LaO_x layer is not observable in the Raman experiments.

In situ XPS is conducted to gain information about the near-surface composition and chemical environment of Ru in LFRO before and after reduction treatment in 1 mbar H_2 at various

https://doi.org/10.1021/acs.chemmater.4c01084
Chem. Mater. XXXX, XXX, XXX−XXX

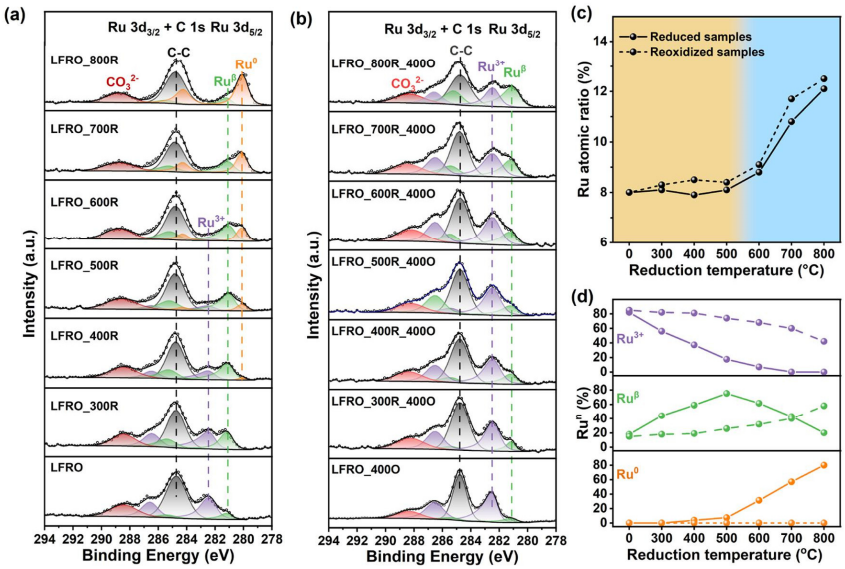

Figure 3. Fitted C 1s + Ru 3d *ex situ* XPS of (a) the as-prepared LFRO, different temperature-reduced samples, and (b) 400 °C reoxidized samples. The atomic ratio of Ru (c) and the distribution among the Ru states (d) are shown as a function of reduction temperature (solid line) and after reoxidation (dash line).

Table 1. *Ex situ* XPS-Derived Near-Surface Composition and Ru Oxidation State Distribution of LFRO, after Reduction (4 vol % H_2 Balanced by Ar) at Different Temperatures and after Oxidation (400 °C in 10 vol% O_2 Balanced by Ar) Ones

	reduced samples						oxidized samples					
	atomic ratio (%)[a]			Ru^n (%)			atomic ratio (%)[a]			Ru^n (%)		
samples	Ru	La	Fe	Ru^{3+}	Ru^{β}	Ru^0	Ru	La	Fe	Ru^{3+}	Ru^{β}	Ru^0
LFRO	8.0	54.3	37.7	82	18	0	8.0	54.5	37.5	85	15	0
LFRO_300R	8.1	53.9	38.0	54	46	0	8.3	52.4	39.3	82	18	0
LFRO_400R	7.9	54.4	37.6	37	59	4	8.5	52.5	39.0	81	19	0
LFRO_500R	8.1	53.3	38.5	17	72	11	8.4	53.1	38.5	74	26	0
LFRO_600R	8.8	55.1	36.1	7	62	31	9.1	52.8	38.0	78	22	0
LFRO_700R	10.8	56.1	33.1	0	46	54	11.7	52.9	35.3	60	40	0
LFRO_800R	12.1	55.7	32.2	0	16	84	12.5	53.3	34.2	42	58	0

[a]Determined by *ex situ* XPS.

temperatures for 1 h (cf. Figures 2 and S2). The adventitious carbon is eliminated from the calcined LFRO through an *in situ* oxidation treatment in 0.5 mbar O_2 at 600 °C. Three major signals are apparent in the Ru $3d_{5/2}$ spectrum at binding energies of ~282.5, ~281.2, and ~280.1 eV that are assigned to Ru^{3+}, Ru^{β}, and Ru^0, respectively; we have to keep in mind that the spectral feature of Ru $3d_{3/2}$ partially overlaps with C 1s (fitting parameters are provided in Table S1).[20,21] The Ru^{3+} represents the Ru species in the perovskite structure occupying the center of the BO_6 octahedron (replacing Fe that is in the 3+ oxidation state), while Ru^0 is ascribed to metallic ruthenium. The lower binding energy of Ru^{β} compared to Ru^{3+} is indicative of a less oxidative surrounding and is therefore assigned to a lower oxidation state than 3+. We have to keep in mind that the Ru $3d_{5/2}$ of Ru^{4+} in RuO_2 is reported at a similar binding energy as Ru^{β}.[22] Under such reducing conditions, however, the interpretation of Ru^{β} as being due to Ru^{4+} can be safely ruled out.

Figure 2a indicates that part of Ru^{3+} is transformed to Ru^{β} after reductive treatment in 1 mbar H_2 at 300 °C for 1 h. For a reduction temperature of 400 °C, Ru^{3+} is completely transformed to Ru^{β}, while still no Ru^0 species is formed, thus confirming Ru^{β} as an intermediate species of the reduction treatment. Only when Ru^{3+} is completely transformed to Ru^{β}, a further increase of the reduction temperature leads to the formation of Ru^0 that is assigned to metallic ruthenium and therefore to the formation of exsolved Ru nanoparticles. This series of *in situ* Ru 3d spectra clearly shows that the three different Ru species evolve successively, and Ru slightly accumulates in the near-surface region after a reduction treatment at 600 °C (cf. Figure 2b).

When looking at the Ru $3d_{3/2}$ + C 1s region, we can recognize that the C 1s peak partly returns when the LFRO is

https://doi.org/10.1021/acs.chemmater.4c01084
Chem. Mater. XXXX, XXX, XXX−XXX

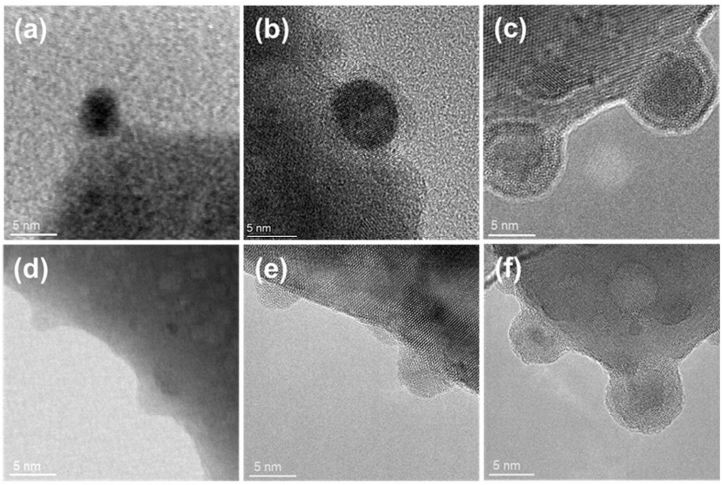

Figure 4. *Ex situ* TEM images of the reduced samples: (a) LFRO_600R, (b) LFRO_700R, and (c) LFRO_800R and reoxidized samples. (d) LFRO_600R_400O, (e) LFRO_700R_400O, and (f) LFRO_800R_400O.

reduced to 500 °C. Likely, carbon segregates from the bulk to the surface or the near-surface region. Figure S2 displays the *in situ* XP spectra for La $3d_{5/2}$, Fe $2p_{3/2}$, and O 1s of LFRO before and after reduction with 1 mbar H_2 at varying temperatures for 1 h and after 400 °C reoxidation of LFRO_700R. No significant changes in the oxidation state are detected for these elements. However, heating the sample under H_2 leads to a noticeable shift of La $3d_{5/2}$, Fe $2p_{3/2}$, and O 1s XP spectra toward higher binding energy. This shift can be attributed to an increase in the concentration of O-vacancies that is linked to the transformation of Ru^{3+} to lower Ru oxidation states.

For the *in situ* XPS experiments, we follow *in situ* the temperature-induced reduction process of a single sample. However, the partial pressure of H_2 (1 mbar instead of 40 mbar) and the reduction time (1 h instead of 3 h) are different from the actual preparation experiments of LFRO and its use in catalytic tests. Therefore, we additionally employed *ex situ* XPS to gain systematic information on the exsolution process under conditions relevant to the activity experiments. We stepwise increase the reduction temperature from 300 to 800 °C, and for each reduction temperature, we compare the Ru 3d spectra before and after reoxidation at 400 °C. With this protocol, the *ex-situ* XPS experiments mimic the catalytic light-off curves later shown in Figure 7. The corresponding results are summarized in Figure 3 and Table 1.

We start with the discussion of the reduction experiments (cf. Figure 3a). Similar to the *in situ* experiments in Figure 2, we identify three different Ru species: Ru^{3+}, Ru^{β}, and Ru^0. For the as-prepared LFRO, 82% (in atomic ratio) well-coordinated Ru (Ru^{3+} in the center of BO_6 octahedron that is coordinated to six oxygen) and 18% Ru^{β} can be derived after the peak fitting of the Ru 3d spectrum (detailed fitting parameters are compiled in Table S2). When LFRO is treated in 4 vol % H_2 at 300 °C for 3 h, 28% of Ru^{3+} is reduced to Ru^{β}. As the reduction temperature goes up to 400 °C, this transformation continues, but it is also accompanied by the emergence of 4% Ru^0 due to the further reduction of Ru^{β}. The Ru^{β} signal dominates the XP spectrum of LFRO_500R and reaches a concentration of 72%, whereas only 17% Ru^{3+} and 11% Ru^0 are left in the near-surface region of the sample. After reductive treatment at 600 °C for 3 h, the Ru distribution changes to 7% Ru^{3+}, 62% Ru^{β}, and 31% Ru^0. For reduction at 700 °C, the Ru^{3+} species vanishes, establishing a distribution of 46% Ru^{β} and 54% Ru^0. The intensity of Ru^0 is enhanced as the reduction temperature increases to 800 °C, accounting for 84% of the area in the Ru 3d spectra of LFRO_800R. All of these numbers clearly indicate that exsolved metallic Ru particles are formed, a process that already starts at about 500 °C.

The XPS-derived fractions of various Ru species are summarized in Figure 3c,d as a function of reduction temperature before and after reoxidation. The total Ru atomic content (Figure 3c) is found to be nearly constant (~8%) up to a reduction temperature of 500 °C, while Ru^{3+} transforms to Ru^{β} and finally to Ru^0. This finding tells us that the exsolution process is mostly restricted to the near surface (region probed by XPS). The total Ru content in the near surface starts to increase above a reduction temperature of 500 °C: 8.8, 10.8, and 12.1% calculated for LFRO_600R, LFRO_700R, and LFRO_800R, respectively (Figure 3b and Table 1). Ru starts to diffuse from the bulk to the surface above 500 °C and leading to the observed enrichment of Ru in the near-surface region.

For all of the reduced samples LFRO_TR, the total Ru content in the near-surface region is preserved upon reoxidation treatment in 10 vol % O_2 at 400 °C (Figure 3c). However, upon mild reoxidation, the Ru^0 component transforms completely to oxidic species, namely, Ru^{3+} and Ru^{β} as displayed in Figure 3b. For LFRO_300R_400O and LFRO_400R_400O, the Ru^{β}/Ru^{3+} intensity ratio remains practically constant, while the ratio of Ru^{β}/Ru^{3+} increases for reduction temperature exceeding 400 °C (cf. dashed lines in Figure 3d).

The morphology evolution of LFRO during the exsolution process is visualized with *ex situ* TEM in Figures 4 and S3. In

https://doi.org/10.1021/acs.chemmater.4c01084
Chem. Mater. XXXX, XXX, XXX−XXX

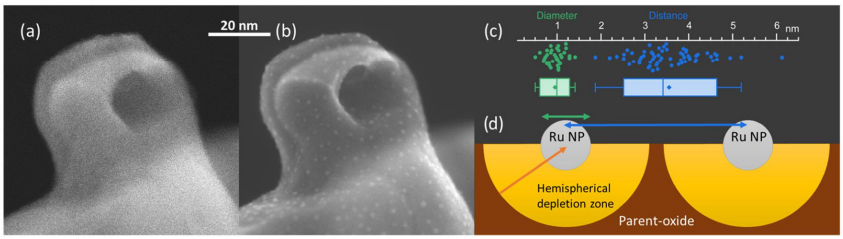

Figure 5. *In-situ* secondary electron (SE)TEM micrographs of LFRO (a) at room temperature and (b) at 500 °C under H_2 after 20 min; (c) the particle diameter and interparticle distance distribution; and (d) schematic illustration of Ru agglomeration from a hemispherical depletion zone below the Ru particle.

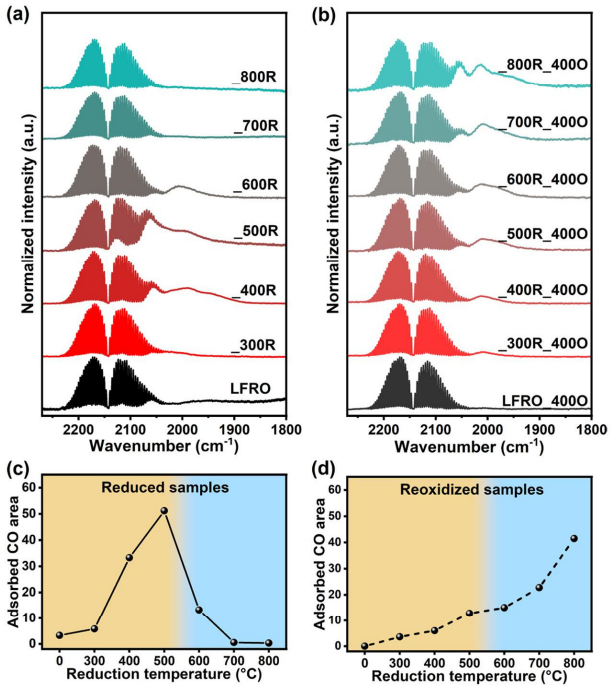

Figure 6. CO-DRIFT spectra using gaseous CO intensity as the reference of (a) LFRO, the different temperature-reduced perovskites, and (b) reoxidized samples. The integrated intensities of adsorbed CO are shown in panel (c, d).

these micrographs, it is possible to observe that part of the Ru already exsolved at 500 °C, as signified by the appearance of about 1 nm small particles in LFRO_500R in Figure 3c. When reduced at elevated temperatures (T > 500 °C), the exsolved particle can be easily distinguished from the parent matrix with a clear boundary in the bright field images in Figure S4 and Figure 4a–c. As the reduction temperature increases, the ongoing exsolution of Ru from the parent perovskite leads to the growth of exsolved particles with mean particle diameters of 2.4, 4.9, and 8.3 nm for LFRO_600R, LFRO_700R, and LFRO_800R, respectively (cf. Figure S4). More interestingly, exsolved particles of LFRO_700R and LFRO_800R are entirely encapsulated by a coating layer with a thickness of ~1 nm (cf. Figure 4b,c), while a covering layer is not discernible for LFRO_500R and LFRO_600R in Figure 4a. Upon reoxidation at 400 °C, the covering layer on the exsolved particles of LFRO_700R and LFRO_800R is removed (Figure 4d–f). The EDS mappings of LFRO_800R in Figure S5 suggest that the exsolved particle is composed of Ru, La, and a low amount of Fe with Ru being the dominant element. Since the line scan on La is wider (about 1 nm on each side) than that of Ru (cf. Figure S5f), the exsolved particle consists mainly of a Ru core, while the particle is covered by a La compound, likely to be LaO_x. Fe is located in the particle core, and there is practically no Fe in the LaO_x layer so that metallic Fe is alloyed with metallic Ru in the core of the exsolved particle. The LaO_x

https://doi.org/10.1021/acs.chemmater.4c01084
Chem. Mater. XXXX, XXX, XXX−XXX

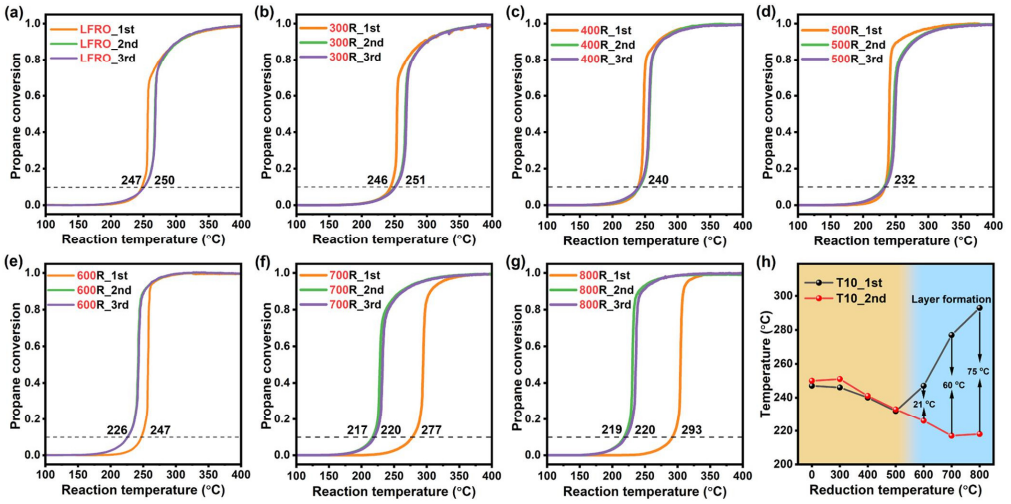

Figure 7. Light-off (conversion) curves of (a–g) as-prepared and LFRO perovskites reduced at various temperatures ranging from 300 to 800 °C in three consecutive reaction cycles. The samples reduced at temperatures within 500 °C reveal a similar T10 temperature while the activation phenomenon can be observed in the samples reduced at temperatures higher than 500 °C. (h) T10 values in the first two successive propane combustion reaction tests of unpretreated LFRO and after thermal reductive treatment at different temperatures (from 300 to 800 °C).

signal in Figure S6 (La in the shell) greatly decreases after mild oxidation at 400 °C, implying that La dissolves back to the support instead of into the exsolved particle.

Using *in situ* TEM with a secondary electron detector, we tracked the exsolution process at 500 °C (LFRO_500R) while analyzing the same spot (cf. Figure 5). This allows us to monitor the growth of Ru nanoparticles and to estimate their size distribution and surface density, particularly at the beginning of the reductive Ru exsolution process (cf. snapshots summarized in Figure S7). The particle on the surface could be observed after reduction at 500 °C for 20 min in Figure 5b, corroborating that the exsolution of Ru starts already at 500 °C. The surface of LFRO is homogeneously decorated by Ru nanoparticles approximately 1 nm in diameter. The average distance between the particles is 3.5 nm (as showcased in Figure 5c). From these values, we can estimate the total amount of exsolved Ru from the particle size and density. Assuming a mean concentration of 5 mol % Ru in LFRO, the exsolution of a 1 nm big Ru NP needs practically all Ru that is present in a 2 nm hemisphere of the LFRO sample centered underneath the Ru particle (cf. Figure 5c). According to our model (cf. Figure S8 for more details), the exsolved particles collect all of the available Ru atoms from a 2 to 3 nm thick slab of LFRO. This model is consistent with *in-situ* XPS experiments, where the Ru concentration is not changed up to 500 °C reduction (cf. Figure 2).

XPS interrogates both the surface and the near-surface region (in a depth of 2 to 3 nm, the escape depth of the photoelectrons).[23] However, the topmost layer exposed to the reaction mixtures determines the catalytic performance. This information is accessible to CO-DRIFTS, where infrared spectroscopy of CO molecules probes the status and chemical nature of the topmost layer of the catalyst, thus providing information about the exsolved Ru particles and on the LaO_x coating layer. The CO-DRIFT spectra in Figure 6a are dominated by the gaseous CO species serving as intensity reference for the spectra, and, in addition, showcase adsorbed CO in the spectral range of 1900 to 2100 cm^{-1}. For LFRO and LFRO_300R, only tiny spectral features of adsorbed CO are observable. When the LFRO sample is reduced at 400 °C, some overlapping bands of the adsorbed CO appear in the range of 1900 to 2100 cm^{-1}, evidencing the presence of additional active sites for CO adsorption. The intensity of adsorbed CO bands increases dramatically for LFRO_500R (cf. Figure 6c), which coincides with the exsolution of Ru. Upon reductive treatment in 4 vol % H_2 at 600 °C for 3 h, the intensity of these features declines (cf. Figure 6c), indicating that the CO adsorption capacity has significantly decreased. This finding can be attributed to the formation of the covering layer. The similarity of the CO-DRIFT spectra of LFRO_550R and LFRO_500R in Figure S9 suggests that the LaO_x covering starts to grow only above 550 °C. For LFRO_700R and LFRO_800R, the CO adsorption signals are almost completely suppressed, suggesting that exsolved Ru particles are now fully covered by a passivating LaO_x layer.

The DRIFTS area of adsorbed CO of LFRO_300R, LFRO_400R, and LFRO_500R is greater than those after mild reoxidation at 400 °C (Figure 6a,b). This behavior is indicative of the oxidation of the Ru particles to RuO_2.[24] For LFRO_600R, where the CO adsorption band decreases with respect to the sample LFRO_500R, reoxidation leads to slightly higher intensities of adsorbed CO bands. DRIFT spectra of LFRO_700R and LFRO_800R indicate no adsorbed CO bands, while mild reoxidation of these samples leads to strong bands of adsorbed CO (cf. Figure 6b,d). This behavior is fully compatible with the removal of the covering LaO_x layer and is reflected by the intensity increase in Figure 6d.

In a previous study,[15] conversion curves (light-off curves) of propane combustion up to 400 °C showed that LFRO_800R is

https://doi.org/10.1021/acs.chemmater.4c01084
Chem. Mater. XXXX, XXX, XXX−XXX

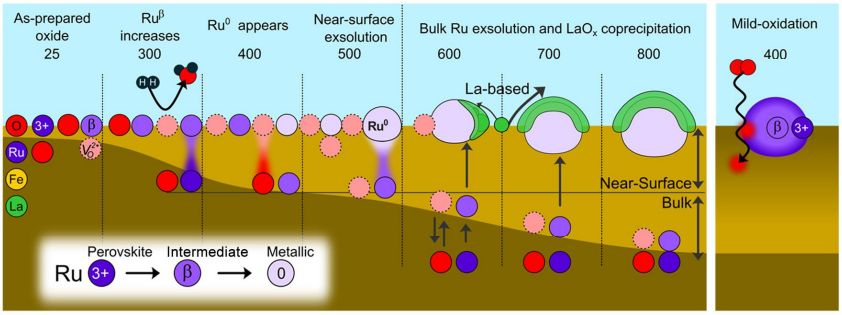

Figure 8. Schematic illustration of structure evolution of LFRO, including the Ru exsolution and LaO_x covering layer evolution during the exsolution process (from 300 to 800 °C). The chemical processes are summarized using Kröger–Vink notation in eqs S1 to S12 in the Supporting Information.

deactivated, while a second conversion curve reveals self-activation of the catalyst (hysteresis). The deactivation was traced to the formation of a LaO_x layer that had been removed during the first conversion curve when reaching 400 °C or alternatively by mild reoxidation at 400 °C. Here, we utilize the hysteresis behavior of conversion curves as a diagnostic tool to identify the formation of the LaO_x layer. In doing so, we prepared LFRO and reduced LFRO at various temperatures. For each of these samples, we measure three consecutive conversion curves for propane combustion from 100 to 400 °C, whose results are summarized in Figure 7a–g. For all of the samples, propane can be fully converted to CO_2 and H_2O when the reaction temperature is increased to 400 °C. Identical light-off curves of the second and third cycles indicate that all samples run stationary after the first cycle.

As a measure of activity, T10 (temperature at which 10% propane conversion is achieved) is extracted for each sample (reduction temperature) and is summarized in Figure 7h. The T10 of LFRO in the first run is 247 °C and slightly increases to 250 °C when this sample is measured for the second and third time. When the reduction temperature increases to 400 °C, improved catalytic activity is observed by a decrease of T10 to 240 °C. The lowest T10 value in the first conversion curve among different reduction temperatures is achieved with LFRO_500R with a T10 value of 232 °C. When the reduction temperature exceeds 500 °C, the catalytic activity in the first cycle decreases with T10 values of 247, 277, and 293 °C for LFRO_600R, LFRO_700R, and LFRO_800R, respectively. This activity trend goes on for LFRO_900R with a T10 value of 310 °C (cf. Figure S10).

The T10 values of the second cycle slightly increase with respect to the first cycle when the reduction temperature is lower than 500 °C. However, for reduction temperatures of 600 °C and higher, the T10 values in the second cycle are lower than those in the first cycle and the decline in the T10 values between the first and second cycle becomes more pronounced with a higher reduction temperature (cf. Figure 7h). Since the catalytic activity is mainly determined by the number of exposed Ru sites, the observed self-activation process is due to the removal of the LaO_x layer, or in other words, the LaO_x covering layer commences to form after reduction at 600 °C.

3.2. Discussion. *3.2.1. Near-Surface Ru Exsolution at Low Temperatures.* In this study, we systematically investigate the physicochemical surface modifications of $LaFe_{0.9}Ru_{0.1}O_3$ (LFRO) during the reductive exsolution process of Ru, whose various elemental processes are summarized by the schematics in Figure 8. Heating the system in the presence of H_2 leads to the formation of oxygen vacancies (eq 1). Simultaneously, the released electrons from this redox reaction are transferred to the most reducible element within the structure, resulting in the partial reduction of Ru^{3+} toward Ru^{β} (eq 2) as experimentally observed by XPS (Figures 2 and 3). Increasing the temperature facilitates the reduction process, finally leading to the complete reduction of Ru^{3+} to zero valence (Ru^0). These reduced Ru atoms agglomerate, creating Ru nanoparticles, as observed using *in situ* TEM (Figure 5), and iron vacancies (eq 3).

$$O_O^x + H_2 \rightarrow V_O^{2\cdot} + 2e^- + H_2O \quad (1)$$

$$Ru_{Fe}^x + (3-\beta)e^- \rightarrow Ru_{Fe}^{(3-\beta)'} \quad (2)$$

$$Ru_{Fe}^{(3-\beta)'} + (\beta)e^- \rightarrow Ru_{Fe}^{3'} \rightarrow Ru_{Ru,particle}^x + V_{Fe}^{3'} \quad (3)$$

During the exsolution process, the cations in B sites are reported to diffuse in the partially reduced form inside the perovskite matrix toward the surface and subsequently being reduced to zero oxidation state.[25−27] Similarly, the migration of Ru takes place probably in the form of Ru^{β}. During the extraction of oxygen and Ru, the parent oxide forms an equivalent amount of oxygen and ruthenium vacancies ($xV_O^{2\cdot}$; $2/3xV_{Ru}^{3'}$). The formation of these vacancies couples, so-called Schottky defects, provides potential diffusion pathways for ions located in the deeper bulk, as reported by Han et al.[28]

Reduction at 300 °C leads to the partial transformation of Ru^{3+} to Ru^{β}, while further reduction at 400 °C initiates the transformation Ru^{β} toward Ru^0 (*ex situ* XPS, Figure 3), although neither *in situ* nor with *ex situ* STEM (Figures 4 and 5) is able to image exsolved Ru particles. However, DRIFTS experiments in Figure 6 showcase a steep increase of the concentration of active Ru sites for CO adsorption already at 400 °C. Conversion curves for propane combustion indicate an increase in activity for LFRO that is reduced at 400 °C. All of the experimental evidence therefore suggests that reductive Ru exsolution at the surface begins at approximately 400 °C under 4 vol % H_2 for 3 h. This finding indicates that the Ru^{β} species

https://doi.org/10.1021/acs.chemmater.4c01084
Chem. Mater. XXXX, XXX, XXX−XXX

is more stable than Ru^{4+} in RuO_2 in a reductive environment. Ru^{4+} can easily reduce to Ru^0 at 200 °C in H_2.[29]

Upon reaching a reduction temperature of 500 °C, a significant fraction of Ru^{β} undergoes transformation to the zero oxidation state, with nanoparticles appearing on the LFRO surface (*in situ* TEM, Figure 5) and a clear spectral feature of Ru^0 in the Ru 3d XP spectrum (*in situ* and *ex situ*, Figures 2a and 3a). From quantitative analysis of Ru 3d XP spectra, no discernible changes in the total amount of Ru in the near-surface region are observed for LFRO up to a reduction temperature of 500 °C, which is in good agreement with the Raman results in Figure 1. This means that for reduction temperature up to 500 °C, Ru from bulk LFRO is not able to diffuse toward the surface. Evaluation of *in situ* STEM of LFRO indicates that the total amount of exsolved Ru by reduction under H_2 at 500 °C is equivalent to the Ru content from a 2 to 3 nm thick surface layer of LFRO as outlined in Figure 5d. After 20 min, both the number and the size of exsolved Ru particles (cf. Figure S7) are stable. Therefore, we conclude that the near-surface region of LFRO is maximum depleted in Ru that cannot be (partially) restored by bulk diffusion of Ru. Note that deactivation is not observed for LFRO reduced at 500 °C, whereas CO-DRIFTS reveals the strongest bands of adsorbed CO for LFRO_500R. Both observations exclude deactivation of the exsolved Ru particles due to a covering LaO_x layer for reduction temperatures up to 500 °C.

3.2.2. Ru Exsolution from the Bulk and La Precipitation. From the hysteresis observed in the conversion curves of propane combustion (cf. Figure 7), deactivation of the Ru particles is concluded to commence at a reduction temperature of 600 °C. A similar conclusion can be drawn from the CO-DRIFTS experiments shown in Figure 6. Vibrational bands of adsorbed CO decrease substantially for LFRO reduced at 600 °C compared to those of LFRO 500R and LFRO 550R (Figure S9). Altogether, these findings support the deactivation of Ru particles by a partially covering LaO_x layer. At the same temperature of 600 °C, XPS (cf. Figure 3c) evidences that the total Ru content within the probing depth of XPS starts to increase due to diffusion of Ru from the bulk toward the surface and the exsolved Ru particles undergo further growth.

The process of Ru exsolution leads to an A-site enriched surface-near region of LFRO with La/Fe > 1 (eq S10) that may not be stable and may transform to a thermodynamically more stable state via segregation of excess La as LaO_x while restoring the ABO_3 stoichiometry (eq S12). The high degree of disorder (cationic and anionic vacancies) facilitates diffusion required for the La segregation process.[30] Recently, it was reported that $La_{1-x}Fe_{1-y}O_{3-3x/2-3y/2}$ leads to either Fe oxide (when La/Fe is less than one) or La_2O_3 (when La/Fe is greater than one) segregation at high temperatures.[31,32] Similar results were reported for the supported $Ni/La_{0.6}Sr_{0.4}FeO_{3-\delta}$ catalyst, where Sr was shown to segregate from the perovskite structure toward the surface forming SrO_x nanorods on the Ni particles in a static hydrogen atmosphere.[33]

In the case of LFRO, the amount of precipitated LaO_x is correlated with the amount of exsolved Ru, which in turn depends sensitively on the reduction temperature. Once La segregates to the surface of LFRO, it can migrate onto the surface of the exsolved Ru particles to reach a stable state by decreasing the surface energy of the exsolved Ru. This is reported as the classical strong metal support interaction (SMSI).[34,35] In a previous study, we demonstrated that a LaO_x layer covers the Ru particles, thereby reducing their reactivity for propane oxidation after reduction at 800 °C.[15] In the present work, employing surface-chemically sensitive techniques, such as CO-DRIFTS, together with operando propane total oxidation reaction and comprehensive physicochemical characterization, we observe that Ru undergoes exsolution already at a reduction temperature of 400 °C, whereas La precipitates as LaO_x on the surface of LFRO only above 600 °C and covers (partly) the exsolved Ru particle. At temperatures higher than 700 °C, exsolved Ru nanoparticles are fully encapsulated by a LaO_x layer as visualized by high-resolution TEM (cf. Figure 4).

4. CONCLUSIONS

When the perovskite solid solution $LaFe_{0.9}Ru_{0.1}O_3$ (LFRO) is reduced in hydrogen at elevated temperatures, ruthenium is extracted and forms anchored nanoparticles on the LFRO surface. From a recent study, it was reported that this exsolution process is accompanied by the formation of a passivating covering LaO_x layer.[15] Employing various experimental techniques, including *in situ* XPS, environmental TEM, and online activity experiments for the catalytic propane combustion reaction in combination with *ex situ* characterization (DRIFTS, XPS, Raman), we gain a detailed atomistic view on the exsolution mechanism of $LaFe_{0.9}Ru_{0.1}O_3$ (LFRO). Most importantly, the hysteresis in repeated conversion curves of propane combustion turns out to be a powerful diagnostic tool to identify the reduction temperature at which the passivating LaO_x starts to cover the exsolved Ru particles. The exsolution process of Ru proceeds sequentially $Ru^{3+} \rightarrow Ru^{\beta} \rightarrow Ru^0$, where Ru^{β} serves as a reaction intermediate with an oxidation state lower than +3. The Ru^{β} species is formed by hydrogen-induced O-vacancy formation, while the formation of Ru^0 indicates the exsolution of Ru. The exsolution of Ru commences at a reduction temperature of 400 °C, where Ru stems exclusively from the near-surface region of LFRO. At reduction temperatures higher than 600 °C, the bulk Ru of LFRO segregates toward the surface and participates in the ongoing growth of exsolved Ru particles. Only at a reduction temperature of 600 °C and higher, passivation of exsolved Ru particles by a covering LaO_x layer is observed. La segregation is thermodynamically driven by the over stoichiometric concentration of La/(Fe+Ru) > 1 of LFRO in the surface-near region after Ru exsolution, whereas a temperature of 600 °C is required to surmount the activation barrier for La segregation. The observed evolution of the La−Fe−Ru perovskite surface structure/morphology during reductive Ru exsolution can aid the design of materials with tailored physicochemical properties, specifically for catalytic applications.

■ ASSOCIATED CONTENT

Supporting Information

The Supporting Information is available free of charge at https://pubs.acs.org/doi/10.1021/acs.chemmater.4c01084.

XRD patterns, XPS spectra, HAADF images, TEM images, including particle distributions, EDS mapping images, *in situ* TEM snapshots of Ru dissolution at 500 °C, schematic models, CO-DRIFTS, light-off curves, fitting parameters for the *in situ* and ex situ XPS and the chemical reactions occurring during reductive ruthenium exsolution using Kröger−Vink notation (PDF)

https://doi.org/10.1021/acs.chemmater.4c01084
Chem. Mater. XXXX, XXX, XXX−XXX

AUTHOR INFORMATION

Corresponding Authors

Yanglong Guo − *State Key Laboratory of Green Chemical Engineering and Industrial Catalysis, Research Institute of Industrial Catalysis, School of Chemistry and Molecular Engineering, East China University of Science and Technology, Shanghai 200237, P. R. China;* orcid.org/0000-0003-0021-9128; Email: ylguo@ecust.edu.cn

Jaime Gallego − *Institute of Physical Chemistry, Justus Liebig University, D-35392 Giessen, Germany; Center for Materials Research, Justus Liebig University, D-35392 Giessen, Germany;* orcid.org/0000-0003-0349-2170; Email: Jaime.Gallego-Marin@phys.chemie.uni-giessen.de

Bernd M. Smarsly − *Institute of Physical Chemistry, Justus Liebig University, D-35392 Giessen, Germany; Center for Materials Research, Justus Liebig University, D-35392 Giessen, Germany;* orcid.org/0000-0001-8452-2663; Email: Bernd.Smarsly@phys.Chemie.uni-giessen.de

Herbert Over − *Institute of Physical Chemistry, Justus Liebig University, D-35392 Giessen, Germany; Center for Materials Research, Justus Liebig University, D-35392 Giessen, Germany;* orcid.org/0000-0001-7689-7385; Email: Herbert.Over@phys.Chemie.uni-giessen.de

Authors

Yu Wang − *State Key Laboratory of Green Chemical Engineering and Industrial Catalysis, Research Institute of Industrial Catalysis, School of Chemistry and Molecular Engineering, East China University of Science and Technology, Shanghai 200237, P. R. China; Institute of Physical Chemistry, Justus Liebig University, D-35392 Giessen, Germany*

Paul Paciok − *Ernst Ruska-Centre for Microscopy and Spectroscopy with Electrons and Peter Grünberg Institute, Forschungszentrum Jülich GmbH, Jülich 52425, Germany;* orcid.org/0000-0002-3432-3321

Lukas Pielsticker − *Department of Heterogeneous Reactions, Max Planck Institute for Chemical Energy Conversion, 45470 Mühlheim an der Ruhr, Germany*

Wei Wang − *State Key Laboratory of Green Chemical Engineering and Industrial Catalysis, Research Institute of Industrial Catalysis, School of Chemistry and Molecular Engineering, East China University of Science and Technology, Shanghai 200237, P. R. China; Institute of Physical Chemistry, Justus Liebig University, D-35392 Giessen, Germany*

Alexander Spriewald Luciano − *Institute of Physical Chemistry, Justus Liebig University, D-35392 Giessen, Germany;* orcid.org/0000-0002-6375-4809

Min Ding − *State Key Laboratory of Green Chemical Engineering and Industrial Catalysis, Research Institute of Industrial Catalysis, School of Chemistry and Molecular Engineering, East China University of Science and Technology, Shanghai 200237, P. R. China*

Lorena Glatthaar − *Institute of Physical Chemistry, Justus Liebig University, D-35392 Giessen, Germany*

Walid Hetaba − *Department of Heterogeneous Reactions, Max Planck Institute for Chemical Energy Conversion, 45470 Mühlheim an der Ruhr, Germany;* orcid.org/0000-0003-4728-0786

Complete contact information is available at: https://pubs.acs.org/10.1021/acs.chemmater.4c01084

Notes

The authors declare no competing financial interest.

ACKNOWLEDGMENTS

This work was supported by the National Key Research and Development Program of China (2022YFB3504200), the National Natural Science Foundation of China (22076047, 21976057, U21A20326), the 111 Project (B08021), and the Fundamental Research Funds for the Central Universities and the PPP-DAAD (57655782). Y.W. acknowledges the China Scholarship Council for the Joint-Ph.D. program with the Institute of Physical Chemistry of the Justus-Liebig-University Giessen. P.P. acknowledges the Federal Ministry for Economic Affairs and Energy (BMWi) of Germany in the framework of POREForm (project number 03ETB027H) for funding. W.H. and L.P. thank the Max Planck Society for the Advancement of Science, Germany, for financial support. H.O. and L.G. acknowledge funding by the German Research Foundation (DFG, Deutsche Forschungsgemeinschaft-493681475). We acknowledge support from the Center for Materials Research at the JLU.

REFERENCES

(1) Zhang, J.; Gao, M. R.; Luo, J. L. *In Situ* Exsolved Metal Nanoparticles: A Smart Approach for Optimization of Catalysts. *Chem. Mater.* **2020**, *32*, 5424−5441.

(2) Kim, J. K.; Kim, S.; Kim, S.; Kim, H. J.; Kim, K.; Jung, W.; Han, J. W. Dynamic Surface Evolution of Metal Oxides for Autonomous Adaptation to Catalytic Reaction Environments. *Adv. Mater.* **2023**, *35*, No. 2203370.

(3) Yang, Y.; Li, J.; Sun, Y. The Metal/oxide Heterointerface Delivered by Solid-based Exsolution Strategy: A review. *Chem. Eng. J.* **2022**, *440*, No. 135868.

(4) Kousi, K.; Tang, C.; Metcalfe, I. S.; Neagu, D. Emergence and Future of Exsolved Materials. *Small* **2021**, *17*, No. 2006479.

(5) Neagu, D.; Oh, T. S.; Miller, D. N.; Menard, H.; Bukhari, S. M.; Gamble, S. R.; Gorte, R. J.; Vohs, J. M.; Irvine, J. T. S. Nano-socketed Nickel Particles with Enhanced Coking Resistance Grown in situ by Redox Exsolution. *Nat. Commun.* **2015**, *6*, No. 8120.

(6) Oh, T. S.; Rahani, E. K.; Neagu, D. J.; Irvine, T. S.; Shenoy, V. B.; Gorte, R. J.; Vohs, J. M. Evidence and Model for Strain-Driven Release of Metal Nanocatalysts from Perovskites during Exsolution. *J. Phys. Chem. Lett.* **2015**, *6*, 5106−5110.

(7) Naeem, M. A.; Abdala, P. M.; Armutlulu, A.; Kim, S. M.; Fedorov, A.; Muller, C. R. Exsolution of Metallic Ru Nanoparticles from Defective, Fluorite-Type Solid Solutions $Sm_2Ru_xCe_{2-x}O_7$ To Impart Stability on Dry Reforming Catalysts. *ACS Catal.* **2020**, *10*, 1923−1937.

(8) Song, Y.; Li, H.; Xu, M.; Yang, G.; Wang, W.; Ran, R.; Zhou, W.; Shao, Z. Infiltrated NiCo Alloy Nanoparticle Decorated Perovskite Oxide: A Highly Active, Stable, and Antisintering Anode for Direct-Ammonia Solid Oxide Fuel Cells. *Small* **2020**, *16*, No. 2001859.

(9) Hua, B.; Yan, N.; Li, M.; Zhang, Y.; Sun, Y.; Li, J.; Etsell, T.; Sakar, P.; Chuang, K.; Luo, J. Novel layered solid oxide fuel cells with multiple-twinned $Ni_{0.8}Co_{0.2}$ nanoparticles: the key to thermally independent CO_2 utilization and power-chemical cogeneration. *Energy Environ. Sci.* **2016**, *9*, 207−215, DOI: 10.1039/C5EE03017J.

(10) Marasi, M.; Duranti, L.; Luisetto, I.; Fabbri, E.; Licoccia, S.; Di Bartolomeo, E. Ru-Doped Lanthanum Ferrite as a Stable and Versatile Electrode for Reversible Symmetric Solid Oxide Cells (r-SSOCs). *J. Power Sources* **2023**, *555*, No. 232399.

(11) Tang, C.; Kousi, K.; Neagu, D.; Metcalfe, I. S. Trends and Prospects of Bimetallic Exsolution. *Chem. - Eur. J.* **2021**, *27*, 6666−6675.

(12) Tsiotsias, A. I.; Ehrhardt, B.; Rudolph, B.; Nodari, L.; Kim, S.; Jung, W. C.; Charisiou, N. D.; Goula, M. A.; Mascotto, S. Bimetallic

https://doi.org/10.1021/acs.chemmater.4c01084
Chem. Mater. XXXX, XXX, XXX−XXX

Exsolved Heterostructures of Controlled Composition with Tunable Catalytic Properties. *ACS Nano* **2022**, *16*, 8904−8916.
(13) Nishihata, Y.; Mizuki, J.; Akao, T.; Tanaka, H.; Uenishi, M.; Kimura, M.; Okamoto, T.; Hamada, N. Self-regeneration of a Pd-perovskite Catalyst for Automotive Emissions Control. *Nature* **2002**, *418*, 164−167.
(14) Katz, M. B.; Graham, G. W.; Duan, Y.; Liu, H.; Adamo, C.; Schlom, D. G.; Pan, X. Self-Regeneration of Pd−$LaFeO_3$ Catalysts: New Insight from Atomic-Resolution Electron Microscopy. *J. Am. Chem. Soc.* **2011**, *133*, 18090−18093.
(15) Wang, Y.; Gallego, J.; Wang, W.; Timmer, P.; Ding, M.; Spriewald Luciano, A.; Weber, T.; Glatthaar, L.; Guo, Y.; Smarsly, B. M.; Over, H. Unveiling the Self-activation of Exsolved $LaFe_{0.9}Ru_{0.1}O_3$ Perovskite during the Catalytic Total Oxidation of Propane. *Chin. J. Catal.* **2023**, *54*, 250−264.
(16) Timmer, P.; Weber, T.; Glatthaar, L.; Over, H. Operando CO Infrared Spectroscopy and On-Line Mass Spectrometry for Studying the Active Phase of IrO_2 in the Catalytic CO Oxidation Reaction. *Inorganics* **2023**, *11*, 102.
(17) Khalid, O.; Weber, T.; Drazic, G.; Djerdj, I.; Over, H. Mixed $Ru_xIr_{1-x}O_2$ Oxide Catalyst with Well-Defined and Varying Composition Applied to CO Oxidation. *J. Phys. Chem. C* **2020**, *124*, 18670−18683.
(18) Lee, W. Y.; Yun, H. J.; Yoon, J. W. Characterization and magnetic properties of LaFeO3 nanofibers synthesized by electrospinning. *J. Alloys Compd.* **2014**, *583*, 320−324.
(19) Sultan, K.; Ikram, M.; Asokan, K. Structural, optical and dielectric study of Mn doped $PrFeO_3$ ceramics. *Vacuum* **2014**, *99*, 251−258.
(20) Morgan, D. J. Resolving ruthenium: XPS studies of common ruthenium materials. *Surf. Interface Anal.* **2015**, *47*, 1072−1079.
(21) Wang, J.; Zhou, J.; Yang, J.; Neagu, D.; Fu, L.; Lian, Z.; Shin, T.-H.; Wu, K. Tailoring the Surface of Perovskite through In Situ Growth of Ru/RuO_2 Nanoparticles as Robust Symmetrical Electrodes for Reversible Solid Oxide Cells. *Adv. Mater. Interfaces* **2020**, *7*, No. 2000828.
(22) Over, H.; Seitsonen, A. P.; Lundgren, E.; Wiklund, M.; Andersen, J. N. Spectroscopic Characterization of Catalytically active Surface Sites of a metallic oxide. *Chem. Phys. Lett.* **2001**, *342*, 467−472.
(23) Powell, C. J.; Jablonski, A. Evaluation of Calculated and Measured Electron Inelastic Mean Free Paths Near Solid Surfaces. *J. Phys. Chem. Ref. Data* **1999**, *28*, 19−62.
(24) Timmer, P.; Glatthaar, L.; Weber, T.; Over, H. Identifying the Active Phase of RuO_2 in the Catalytic CO Oxidation Reaction, Employing Operando CO Infrared Spectroscopy and Online Mass Spectrometry. *Catalysts* **2023**, *13*, 1178.
(25) Calì, E.; Thomas, M. P.; Vasudevan, R.; Wu, J.; Gavalda-Diaz, O.; Marquardt, K.; Saiz, E.; Neagu, D.; Unocic, R. R.; Parker, S. C.; Guiton, B. S.; Payne, D. J. Real-Time Insight into the Multistage Mechanism of Nanoparticle Exsolution from a Perovskite Host Surface. *Nat. Commun.* **2023**, *14*, No. 1754.
(26) Gao, Y.; Chen, D.; Saccoccio, M.; Lu, Z.; Ciucci, F. From Material Design to Mechanism Study: Nanoscale Ni Exsolution on a Highly Active A-Site Deficient Anode Material for Solid Oxide Fuel Cells. *Nano Energy* **2016**, *27*, 499−508.
(27) Kwon, O.; Joo, S.; Choi, S.; Sengodan, S.; Kim, G. Review on Exsolution and its Driving Forces in Perovskites. *J. Phys.: Energy* **2020**, *2*, No. 032001.
(28) Han, H.; Xing, Y.; Park, B.; Bazhanov, D. I.; Jin, Y.; Irvine, J. T. S.; Lee, J.; Oh, S. H. Anti-phase boundary accelerated exsolution of nanoparticles in non-stoichiometric perovskite thin films. *Nat. Commun.* **2022**, *13*, No. 6682.
(29) Knapp, M.; Crihan, D.; Seitsonen, A. P.; Lundgren, E.; Resta, A.; Andersen, J. N.; Over, H. Complex Interaction of Hydrogen with the RuO_2(110) surface. *J. Phys. Chem. C* **2007**, *111*, 5363−5373.
(30) Neagu, D.; Tsekouras, D.; Muller, N. M.; Ménard, H.; Irvine, J. T. S. In situ Growth of Nanoparticles through Control of Non-stoichiometry. *Nat. Chem.* **2013**, *5*, 916−923.
(31) Warnhus, I.; Vullum, P. E.; Holmestad, R.; Grande, T.; Wiik, K. Electronic Properties of Polycrystalline LaFeO3. Part I: Experimental Results and the quantitative Role of Schottky Effects. *Solid State Ionics* **2005**, *176*, 2783−2890.
(32) Mutter, D.; Schierholz, R.; Urban, D. F.; Heuer, S. A.; Ohlerth, T.; Kungl, H.; Elsässer, C.; Eichel, R. A. Defects and Phase Formation in Non-Stoichiometric $LaFeO_3$: a Combined Theoretical and Experimental Study. *Chem. Mater.* **2021**, *33*, 9473−9485.
(33) Thalinger, R.; Gocyla, M.; Heggen, M.; Klötzer, B.; Penner, S. Exsolution of Fe and SrO Nanorods and Nanoparticles from Lanthanum Strontium Ferrite $La_{0.6}Sr_{0.4}FeO_{3-\delta}$ Materials by Hydrogen Reduction. *J. Phys. Chem. C* **2015**, *119*, 22050−22056.
(34) Tang, H.; Su, Y.; Zhang, B.; Lee, A. F.; Isaacs, M. A.; Wilson, K.; Li, L.; Ren, Y.; Huang, J.; Haruta, M.; Qiao, B.; Liu, X.; Jin, C.; Su, D.; Wang, J.; Zhang, T. Classical Strong Metal−support Interactions between Gold Nanoparticles and Titanium Dioxide. *Sci. Adv.* **2017**, 3, No. e1700231.
(35) Xin, H.; Lin, L.; Li, R.; Li, D.; Song, T.; Mu, R.; Fu, Q.; Bao, X. Overturning CO_2 Hydrogenation Selectivity with High Activity via Reaction-Induced Strong Metal−Support Interactions. *J. Am. Chem. Soc.* **2022**, *144*, 4874−4882, DOI: 10.1021/jacs.1c12603.

https://doi.org/10.1021/acs.chemmater.4c01084
Chem. Mater. XXXX, XXX, XXX−XXX

3. Conclusions and Outlook

This thesis presents studies the surface structure evolution of Ru exsolved LFRO perovskites (LFRO_800R) in the oxidative atmosphere and the microscopic structure evolution during the Ru exsolution process.

LFRO, where Ru is fully incorporated into the perovskite structure, is chosen as the starting material for preparing Ru-exsolved perovskite. As supported by SEM and the quantification results of XPS, Heating LFRO at 800 ℃ in a reducing atmosphere results in the migration of Ru from bulk to the surface in the form of particle. The Ru-exsolved sample initially exhibits low propane activity but can be activated in successive propane oxidation reaction test. High resolution TEM and EDS mappings reveal the exsolved Ru is alloyed with a slight amount of Fe in the core that are encapsulated by an inert LaO_x covering layer, which impedes the adsorption of reactant molecular to the active Ru species. By gradually varying the oxidation temperature from 200 ℃ to 400 ℃, the LaO_x coating layer is observed to break up and disappear at 300 ℃ and 400 ℃, respectively. Meanwhile, the exsolved Ru is totally oxidized to RuO_2 without phase segregation of FeO_x, matching well with the DRIFTS results that using CO as a probe molecular. The correlations between the exsolved particles morphology and its catalytic performance in propane oxidation is established. These activated exsolved RuFe particles are shown to be more active in propane combustion compared to those bench mark supported catalysts.

The mechanism of Ru enriched RuFe-LaO_x core-shell structured nanoparticles formation is systematically studies by varying the exsolution temperature of LFRO from 300 to 800 ℃. The *in-situ* XPS results indicate that the Ru exsolution is processing through $Ru^{3+} \rightarrow Ru^{\beta} \rightarrow Ru^0$, where Ru^{β} serves as a reaction intermediate with an oxidation state lower than +3. The formation of Ru^{β} species is correlated to the reduction induced oxygen vacancies, while the emergency of Ru^0 signifies Ru ex solution. The transformation from Ru^{3+} to Ru^{β} starts already at 300 ℃ while the further reduction to exsolved Ru^0 requires at least 400 ℃. The quantification by *ex situ* XPS results suggests that only the Ru in the near surface region (XPS detection region, in a depth of 2-3 nm) could be exsolved at a reduction temperature of 500 ℃. Further enhancing the reduction temperature, the Ru staying in the bulk will be extracted to the surface, leading to the growth of exsolved particle. The CO-DRIFTS, HR-TEM and consecutive propane combustion reaction test reveal that the LaO_x in the emerges at 600 ℃ and totally encapsulates the Ru particles when reduced at 700 ℃. La segregation is thermodynamically driven by the

over-stoichiometric La/(Fe+Ru) >1 in the near-surface region after Ru exsolution, with a temperature of 600 °C necessary to overcome the activation barrier for La segregation.

Overall, the findings of this thesis offer a detailed microscopic understanding of the structural evolution during Ru exsolution and under propane reaction conditions. According to the above-mentioned investigations on the exsolution of Ru from $LaFe_{0.9}Ru_{0.1}O_3$ and its structure evolution in the oxidation atmosphere, together with the novel feathers of perovskite oxides mentioned in **Chapter 1** (reversibility, surface tunability with acid), some interesting points may deserve further investigation:

1. Ru can be transferred into volatile RuO_3 and RuO_4 when it exposed to oxidizing atmosphere at temperature higher than 600 ℃, which limits the application of Ru-based catalyst in high temperature oxidation reaction. However, with the reversibility of perovskite during the redox treatment, the Ru could be well preserved by dissolving back into the perovskite structure in the form of $LaFe_{1-x}Ru_xO_3$ when exposed to elevated temperature (T > 600 ℃) in the oxidative atmosphere.

2. The amount of exsolved Ru is in parallel with the reduction temperature (T≤800 ℃), while the growth of Ru particle leads to the decrease of the active site. With the reversibility of perovskite structure, Ru could be selectively enriched in the near-surface in the form of $LaFe_{1-x}Ru_xO_3$. In this case, the low reduction temperature is enough to exsolved the Ru due to the relatively short diffusion path. It may be a facile way to prepare high density small exsolved particles by re-exsolving the perovskites at low temperature.

3. For the Ru doped perovskite LFRO, the top-most layer is dominated by the La-O layer, which blocks the active site for propane oxidation reaction. It is reported that acid etching could selectively remove La-O termination while retain the perovskite structure, exposing more active Ru species. It is promising to prepare a good oxidation catalyst by acid etching.

4. The surface of perovskite oxide is relatively low due to the high calcination temperature during the sample preparation and limits the exsolution. It would be interesting to investigate the correlations between the surface area and Ru exsolution behavior.

5. The Ru^{β} which is confirmed as the intermediate species plays an important role in the during the Ru exsolution. Ru^{β} can be induced by heating LFRO in reducing atmosphere at temperature lower than 400 ℃. However, the understanding of this Ru species is not enough. The further investigation on this species with advanced characterization may be interesting.

4. Appendix

4.1 Supporting Information of Publication 1

Supporting information for

Unveiling the Self-Activation of Exsolved $LaFe_{0.9}Ru_{0.1}O_3$ Perovskite During Catalytic Propane Combustion

Yu Wang[a,b], Jaime Gallego[b,c], Wei Wang[a,b], Phillip Timmer[b], Min Ding[a], Alexander Spriewald Luciano[b], Tim Weber[b], Lorena Glatthaar[b], Yanglong Guo[a]*, Bernd M. Smarsly[b]*, Herbert Over [b]*

[a] *Key Laboratory for Advanced Materials, Research Institute of Industrial Catalysis, School of Chemistry and Molecular Engineering, East China University of Science and Technology, Shanghai 200237, PR China*
[b] *Institute of Physical Chemistry, Justus Liebig University, Heinrich-Buff-Ring 17, D-35392 Giessen, Germany*
[c] *Center for Materials Research, Justus Liebig University, Heinrich-Buff-Ring 16, D-35392 Giessen, Germany*

* Corresponding authors: email

Herbert.Over@phys.Chemie.uni-giessen.de;

Bernd.Smarsly@phys.Chemie.uni-giessen.de;

ylguo@ecust.edu.cn

1. Absence of heat transfer within the low propane conversion region.

The heat transfer effect for propane with conversion below 15% can safely be neglected if $C_M = \frac{-\Delta H r \rho_b R E}{h T^2 R_g}$<0.15, the Mears' criterion, which is actually fulfilled:

$$C_M = \frac{-\Delta H r_{obs} \rho_b R E}{h T^2 R_g} = \frac{-(-2217.8)\times(2.176\times10^{-3})\times(5.12\times10^{3})\times(1\times10^{-7})\times109}{(6.5\times10^{-2})\times(483^2)\times(8.314\times10^{-3})}$$

$=2.13\times 10^{-3} << 0.15$

Parameters used in Mears Criterion for estimating mass transfer limitation in the propane combustion reaction.

Symbol	**Parameters, unit**	**value**
ΔH	Reaction heat, kJ/mol	-2217.8
r	Reaction rate, mol/(kg_{cat}·s)	2.176×10^{-3}
ρ_b	Bulk density of catalyst, kg/m^3	~5.12×10^{3}
R	Catalyst particle radius, m	~10^{-7}
E	Activation energy, kJ/mol	109
h	Heat transfer coefficient, kJ/(m^2·s·K)	6.5×10^{-2}
Rg	Gas constant, kJ/(mol·K)	8.314×10^{-3}
T	Reaction temperature, K	483

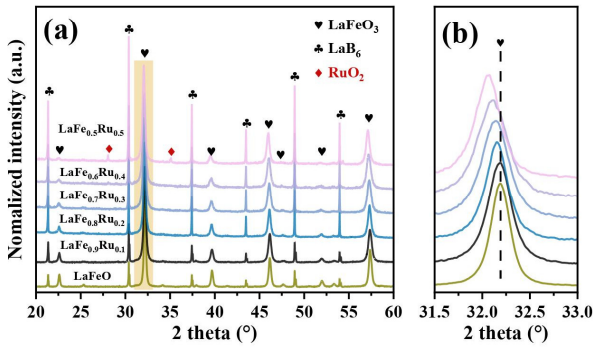

Figure S1. (a) XRD patterns and (b) magnified XRD patterns of the $LaFe_{1-x}Ru_xO_3$ (x=0–0.5) perovskites.

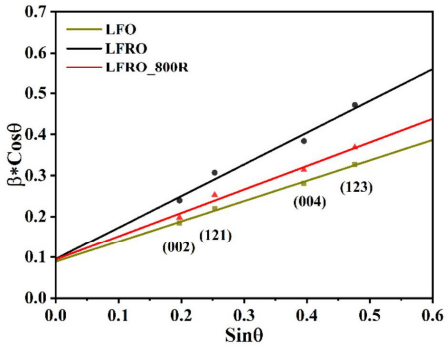

Figure S2. Williamson-Hall plots of Ru free sample (LFO), Ru doped sample (LFRO), and exsolved sample (LFRO_800R) obtained from the separable (002), (121), (004), and (123) reflections.

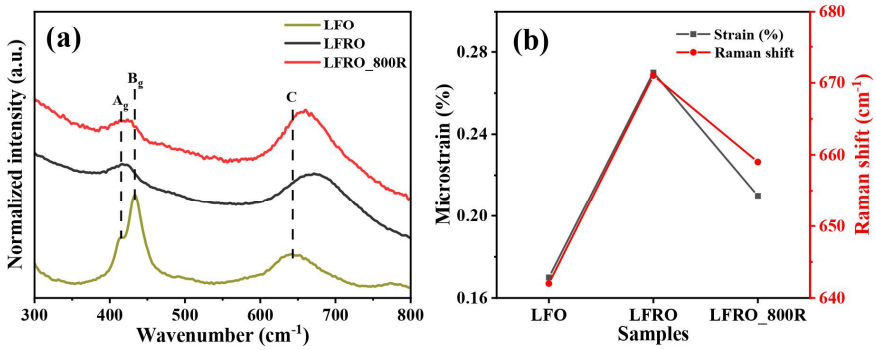

Figure S3. (a) Raman spectra of LFO, 10% Fe is substituted per Ru (LFRO) after calcination at 750 °C, and LRFO after reduction at 800 °C in 4% H_2 (LFRO_800R). (b) Correlations between micro strain and the Raman shift of peak C for these samples.

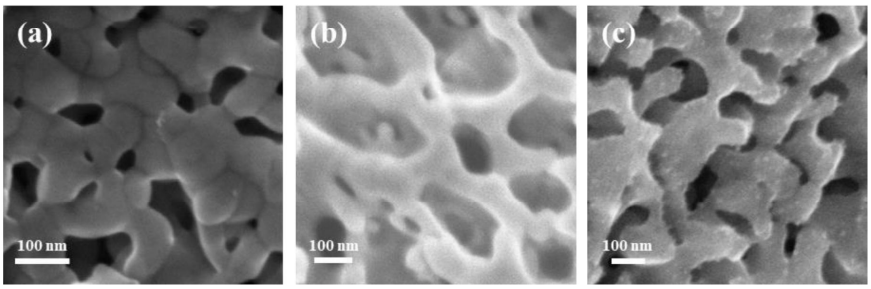

Figure S4. SEM micrographs of (a) LFO, (b) LFRO, and (c) LFRO_800R.

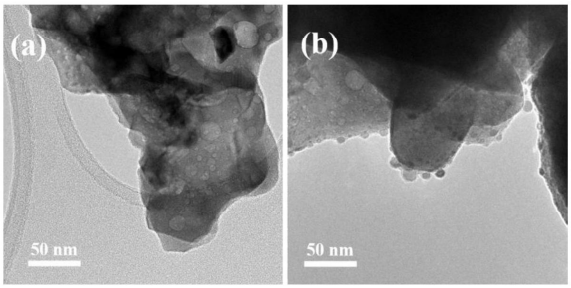

Figure S5. TEM pictures of (a) LFRO and (b) LFRO_800R.

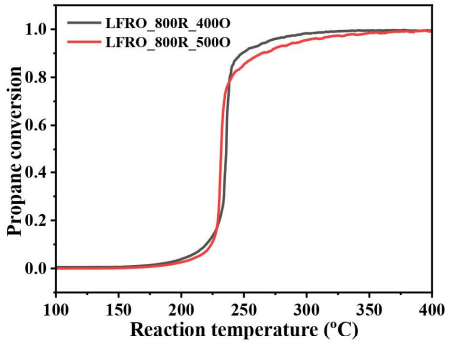

Figure S6. The light-off curve of LFRO_800R_500O. LFRO_800R_400O is presented for comparison reasons.

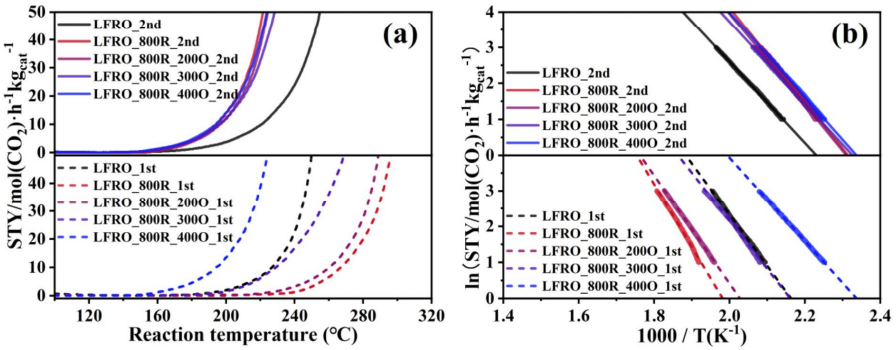

Figure S7. (a) STY and (b) corresponding Arrhenius plots of the studied samples during two reaction cycles. The propane combustion reaction is measured at a reaction mixture of C_3H_8: O_2: Ar = 1:10:89 (in volumetric fraction), at a flow rate of 100 mL/min (standard conditions), and 20 mg of catalyst diluted with 40 mg of inert quartz sand.

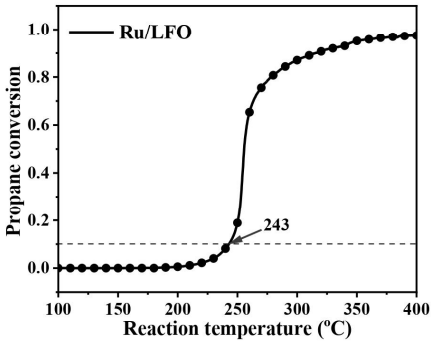

Figure S8. Light-off curve of the supported Ru/LFO catalyst with 5 mol % Ru loading.

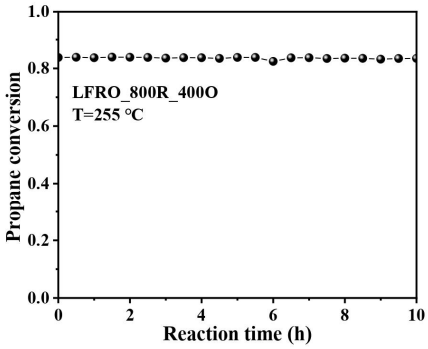

Figure S9. Stability of LFRO_800R_400O in the catalytic propane combustion reaction at 255 °C.

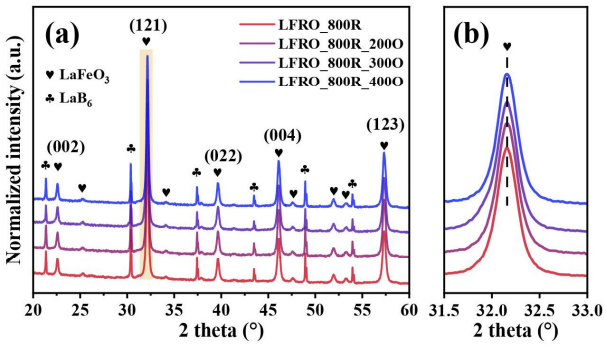

Figure S10. (a) Overview and (b) enlarged XRD patterns of exsolved sample (LFRO_800R), and re-oxidized samples of LFRO_800R_200O, LFRO_800R_300O and LFRO_800R_400O. LaB_6 is applied as an internal standard.

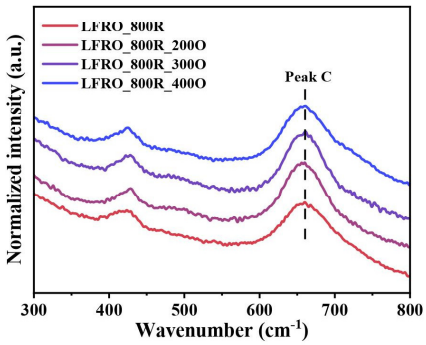

Figure S11. Raman spectra of the reduced sample LFRO_800R and re-oxidized samples LFRO_800R_200O, LFRO_800R_300O and LFRO_800R_400O.

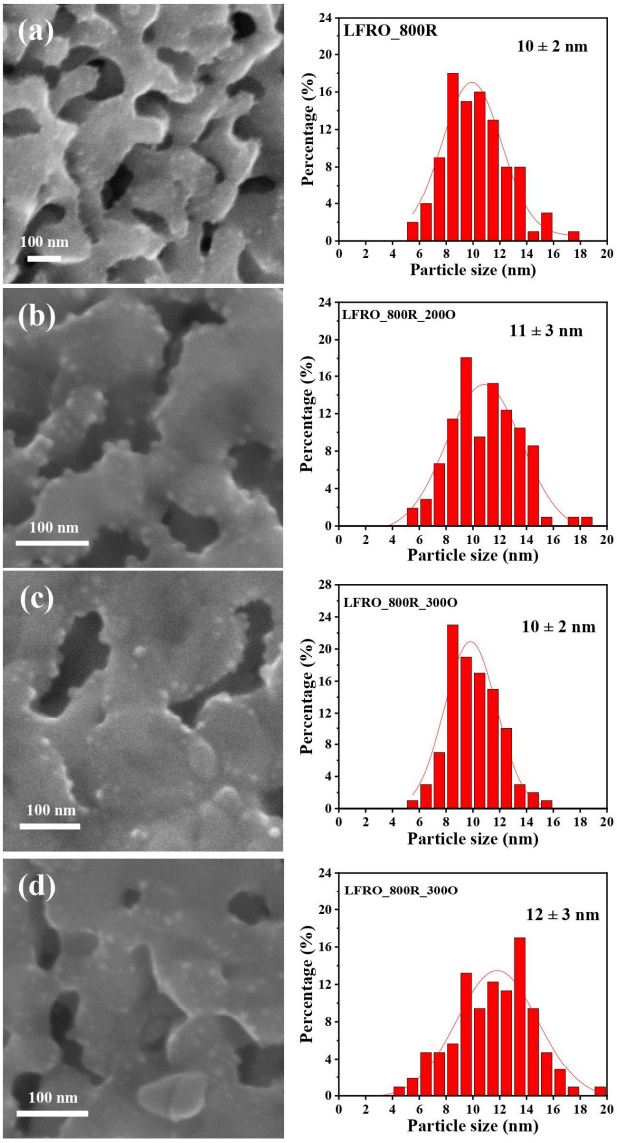

Figure S12. SEM images and corresponding exsolved particle size distributions of (a) LFRO_800R, (b) LFRO_800R_200O, (c) LFRO_800R_300O and (d) LFRO_800R_400O.

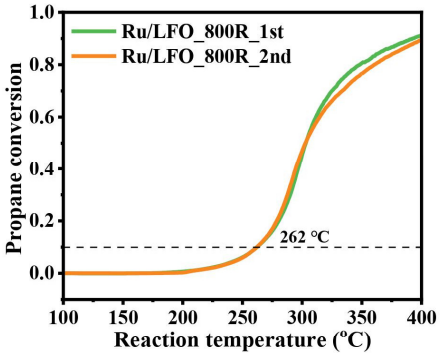

Figure S13. Light-off curves in two reaction cycles of supported Ru/LFO_800R.

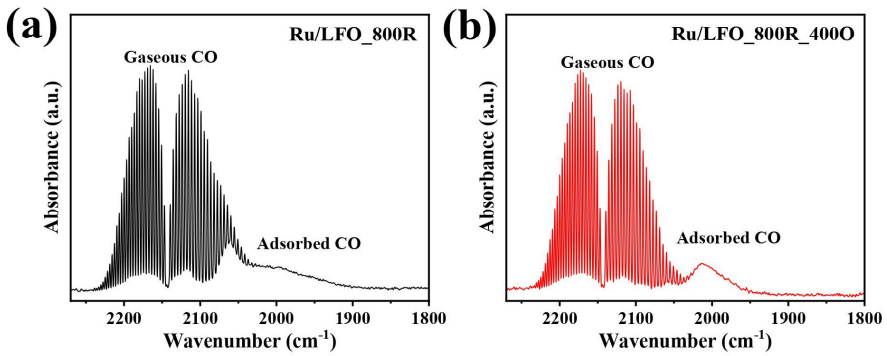

Figure S14. CO-adsorption infrared spectra of (a) Ru/LFO_800R and (b) Ru/LFO_800R_400O.

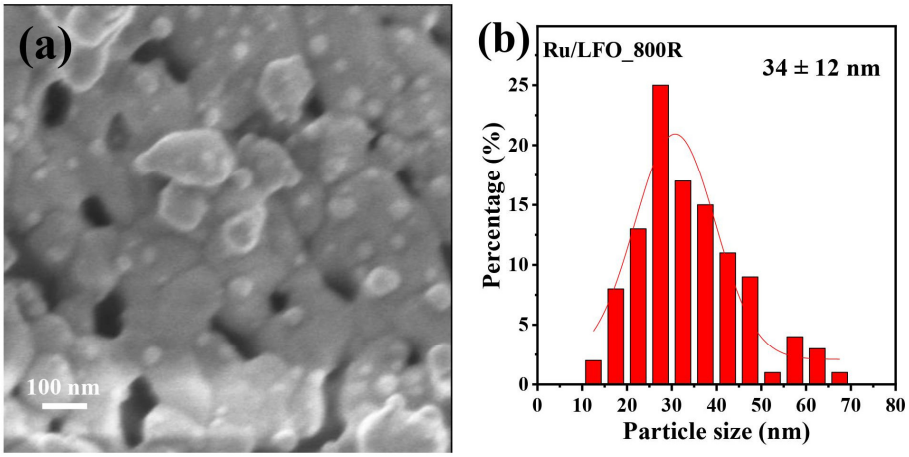

Figure S15. (a) SEM picture of Ru/LFO_800R and **(b)** corresponding particle size distribution.

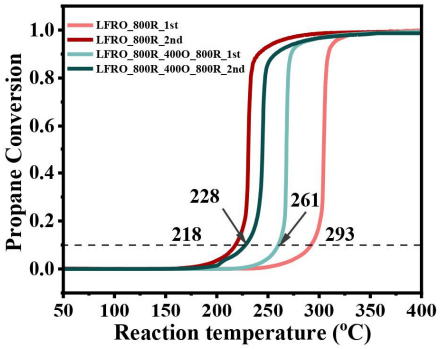

Figure S16. Light-off curves of LFRO_800R_400O_800R in two reaction cycles. The light-off curves for LFR10_800R in two reaction cycles are shown for comparison.

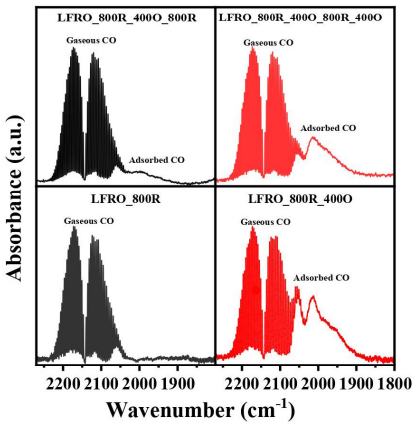

Figure S17. CO-DRIFTS spectra of LFRO_800R_400O_800R and LFRO_800R_400O_800R_400O. The DRIFT spectra of LFRO_800R and LFRO_800R_400O are also provided for comparison.

4.2 Supporting Information of Publication 2

Supporting Information

Microscopic Insight into Ruthenium Exsolution from $LaFe_{0.9}Ru_{0.1}O_3$ Perovskite

Yu Wang[a,b], Paul Paciok[c], Lukas Pielsticker[d] , Wei Wang[a,b], Alexander Spriewald Luciano[b], Min Ding[a], Lorena Glatthaar[b], Walid Hetaba[d], Yanglong Guo[a]*, Jaime Gallego[b,e]*, Bernd M. Smarsly[b,e]*, Herbert Over [b,e]*

[a] *State Key Laboratory of Green Chemical Engineering and Industrial Catalysis, Research Institute of Industrial Catalysis, School of Chemistry and Molecular Engineering, East China University of Science and Technology, Shanghai 200237, PR China*
[b] *Institute of Physical Chemistry, Justus Liebig University, Heinrich-Buff-Ring 17, D-35392 Giessen, Germany*
[c] *Ernst Ruska-Centre for Microscopy and Spectroscopy with Electrons and Peter Grünberg Institute, Forschungszentrum Jülich GmbH, Jülich, 52425, Germany*
[d] *Department of Heterogeneous Reactions, Max Planck Institute for Chemical Energy Conversion, Stiftstr. 34-36, 45470 Mühlheim an der Ruhr, Germany*
[e] *Center for Materials Research, Justus Liebig University, Heinrich-Buff-Ring 17, D-35392 Giessen, Germany*

* Corresponding authors:
Herbert.Over@phys.Chemie.uni-giessen.de;
Bernd.Smarsly@phys.Chemie.uni-giessen.de;
ylguo@ecust.edu.cn;
Jaime.Gallego-Marin@phys.chemie.uni-giessen.de

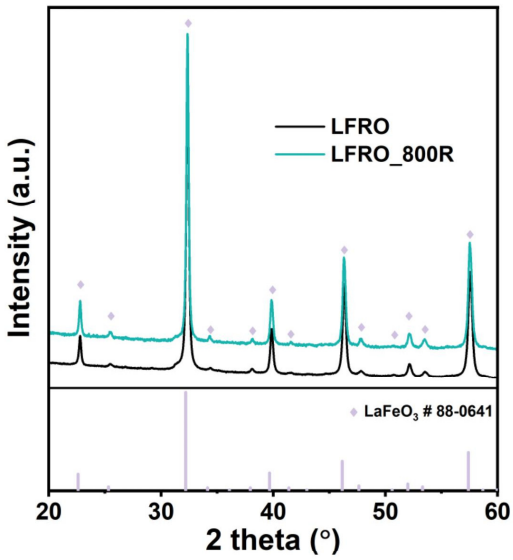

Figure S1. XRD patterns of LFRO, LFRO_800R and standard $LaFeO_3$ (JCPDS NO.88-0641).

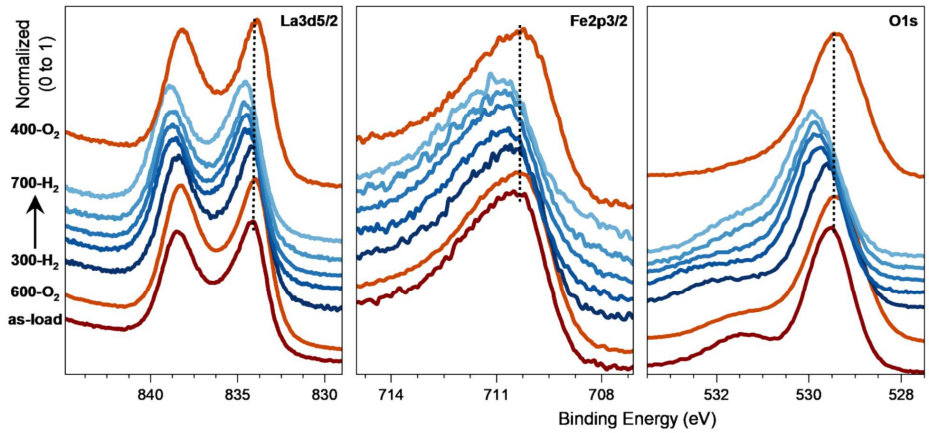

Figure S2. In-situ XPS of La 3d, Fe $2p_{3/2}$, O 1s spectra of the LFRO, LFRO_600O (pretreated under 0.5 mbar O_2 at 600 °C for 1h), different temperature reduced ones (from 300 °C to 700 °C under 1 mbar H_2 for 1 h) and subsequent oxidized LFRO_700R_400O (oxidized at 400 °C under 0.5 mbar O_2 for 1 h).

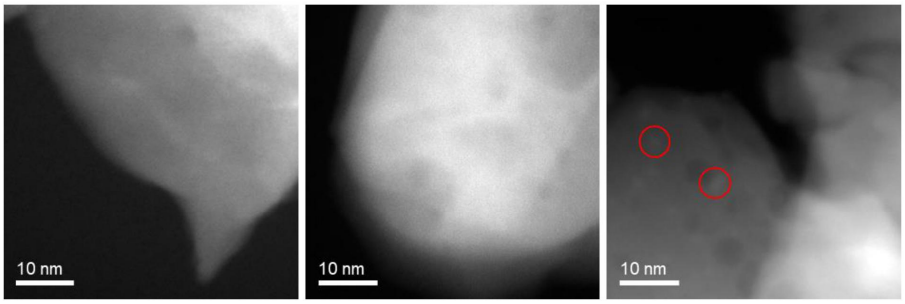

Figure S3. HAADF images of LFR10_300R, LFR10_400R and LFR10_500R.

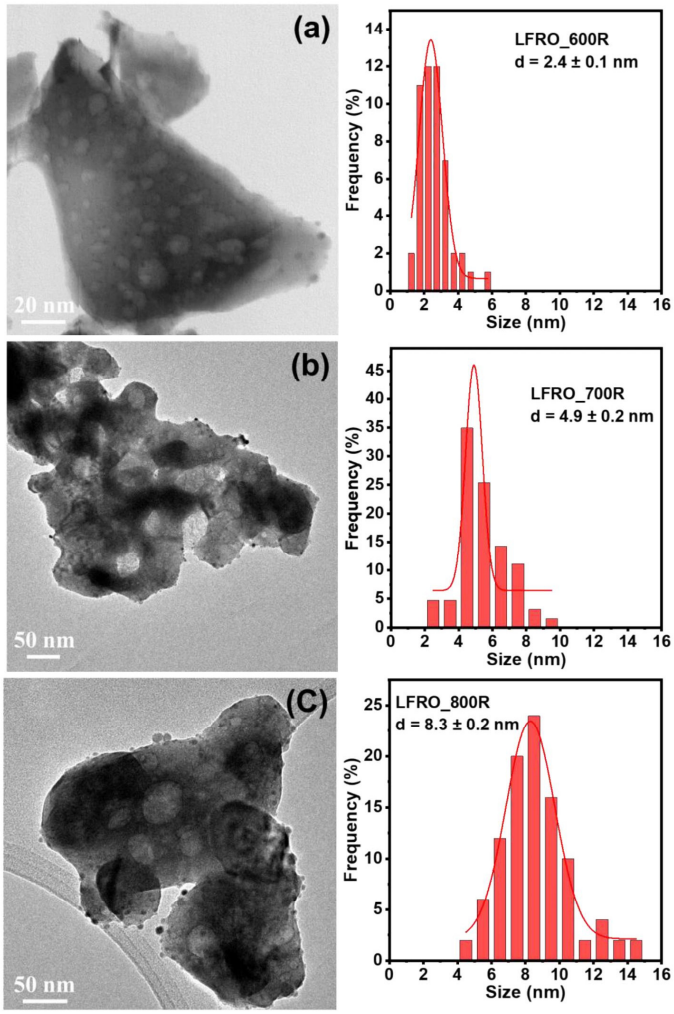

Figure S4. Low magnification TEM images of (a) LFR10_600R, (b) LFR10_700R and (c) LFR10_800R and corresponding size distribution in the right panel.

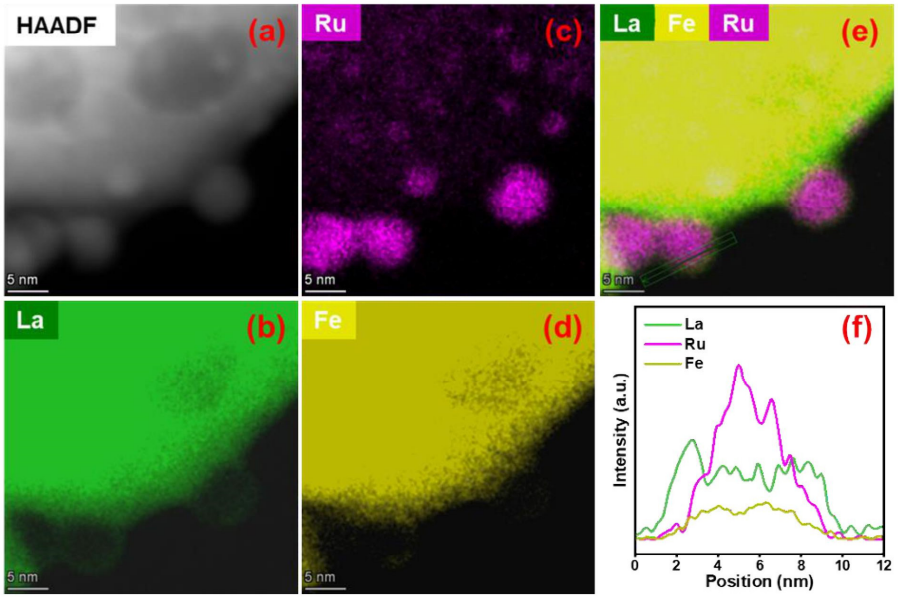

Figure S5. (a) HAADF-STEM image, (b-e) EDS mapping images and (f) the line scan results of LFRO_800R. The position for the line scan is presented in (e) with an arrow confined in a green frame.

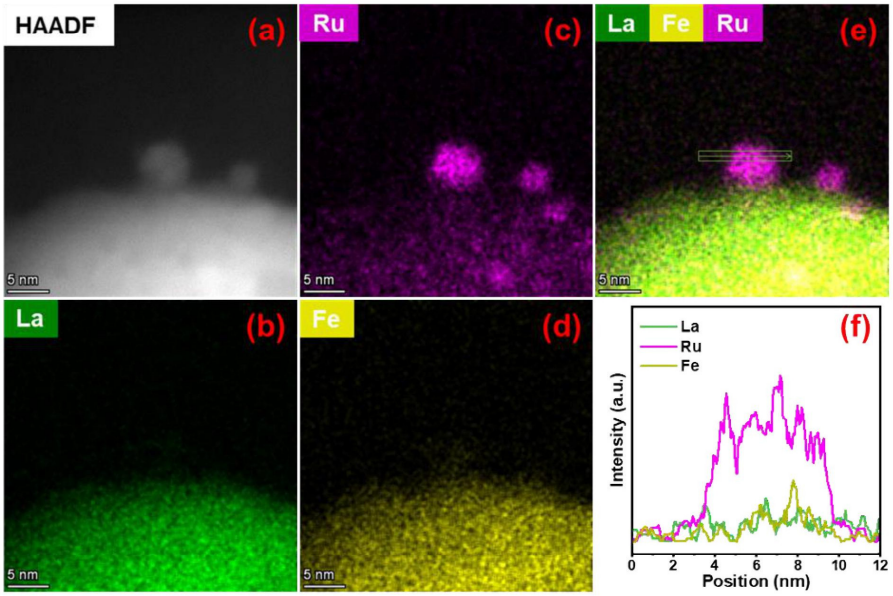

Figure S6. (a) the HAADF-STEM image, (b-e) EDS mapping images and (f) the line scan result of LFRO_800R_400O. The position for the line scan is shown in (e) with an arrow confined in a green frame.

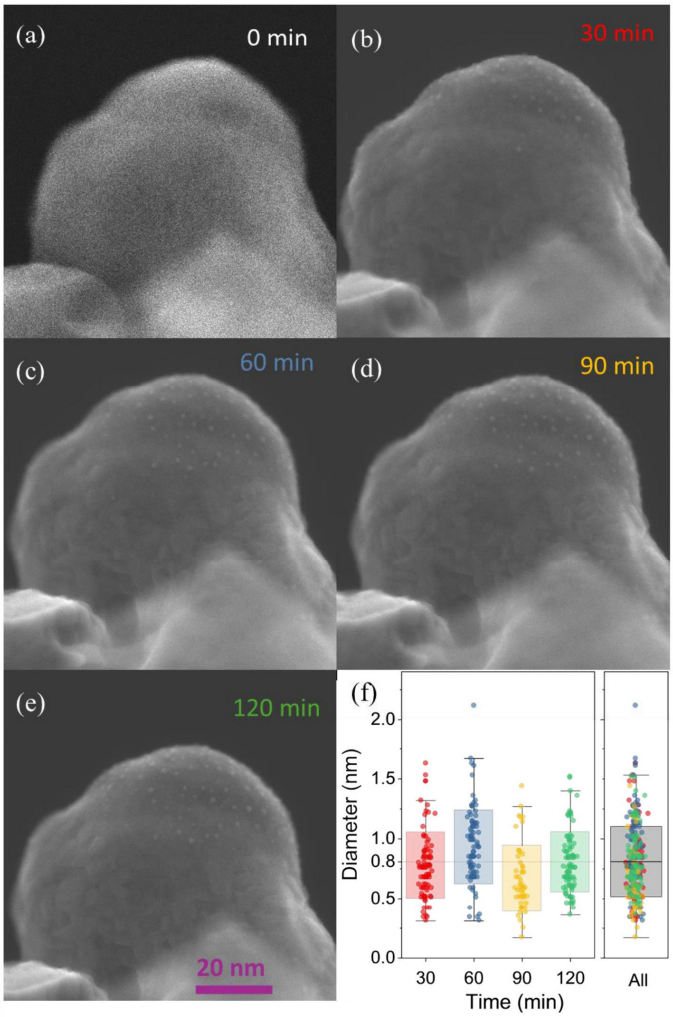

Figure S7. (a-e) *In-situ* SE-STEM images of LFRO collected after exposing to the reductive atmosphere for different time at 500 ℃ and (f) corresponding size distribution. No obvious change on the density and size distribution of the exsolved particles could be observed as the increasing reduction time.

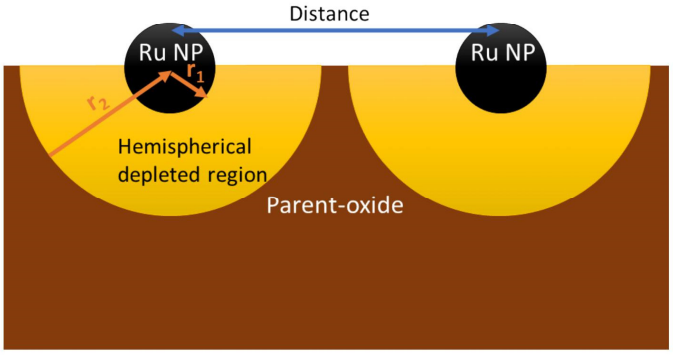

Figure S8. The model used to calculate the Ru-depleted oxide radius.

The mass of Ru in the 1 nm exsolved spherical particles should be equal to the mass of Ru in the hemispherical parent oxide.

$$\rho_{Ru} \times \frac{1}{2} \times \frac{4}{3} \times \pi {r_1}^3 = \rho_{LFRO} \times \omega \times \frac{4}{3} \times \pi {r_2}^3$$

$$r_2 = \sqrt[3]{\frac{2 \times {r_1}^3 \times \rho_{Ru}}{\rho_{\mathrm{LFRO}} \times \omega}} = \sqrt[3]{\frac{2 \times (5 \times 10^{-10})^3 \times 12.36 \times 10^3}{6.732 \times 10^3 \times 0.04}} = 2.2\ nm$$

In order to exsolve a 1 nm sized Ru particle, the Ru in a radius of 2.2 nm hemispherical should be extracted.

Parameters used in the particle size calculation.

Symbol	Parameters, unit	value
r_1	Exsolved Ru particle radius, m	5×10^{-10}
r_2	Radius of Ru depleted oxides, m	~
ρ_{Ru}	Metallic Ru density, kg/m^3	12.36×10^3
ρ_{LFRO}	Ru density, kg/m^3	~6.73×10^3
ω	Ru weight fraction in perovskite, none	0.04

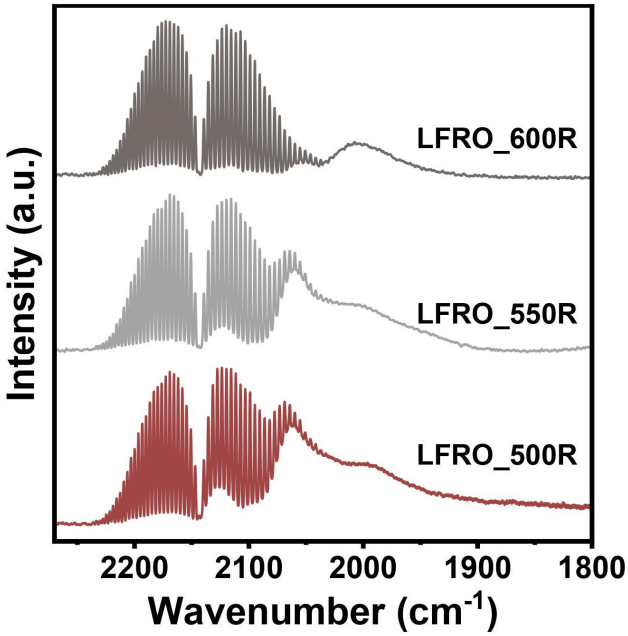

Figure S9. CO-DRIFT spectrum of LFRO_550R. The CO-DRIFTS spectra of LFR0_500R and LFRO_600R are also provided for comparison.

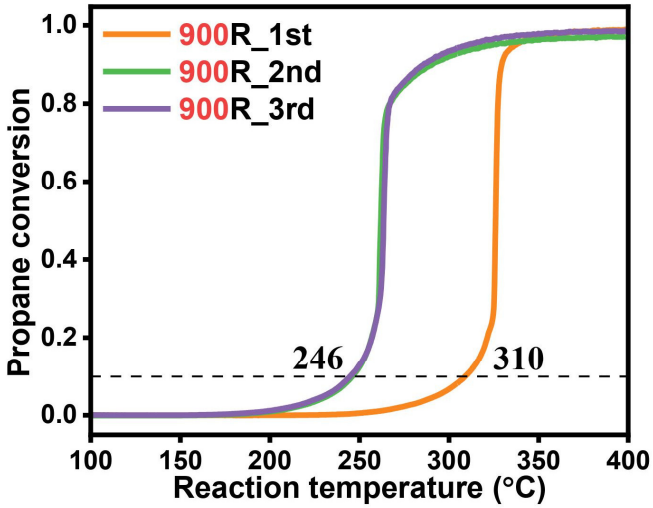

Figure S10. Three consecutive Light-off curves of LFR10_900R perovskites in three reaction cycles.

Table S1. Fitting parameters of Ru 3d in the *in-situ* XPS.

	Ru^{3+} $3d_{5/2}$		Ru^{3+} $3d_{3/2}$		Ru^{β} $3d_{5/2}$		Ru^{β} $3d_{3/2}$		Ru^{0} $3d_{5/2}$		Ru^{0} $3d_{5/2}$	
Line shape	LF(0.4,1,45,280)		LF(0.8,1,45,280)		LF(0.4,1,45,280)		LF(0.6,1,45,280)		LF(0.8,1,45,280)		LF(1.01,1.25,500,50)	
	BE (eV)	FWHM	BE (eV)	FWHM	BE (eV)	FWHM	BE (eV)	FWHM	BE (eV)	FWHM	BE (eV)	FWHM
LFRO	282.2	1.15	286.4	1.38	281.1	0.95	285.3	1.15	-	-	-	-
LFRO_600O	282.2	1.30	286.5	1.75	281.1	0.90	285.3	1.40	-	-	-	-
LFRO_300R	282.3	1.17	286.4	1.42	281.1	1.25	285.3	1.50	-	-	-	-
LFRO_400R	-	-	-	-	281.1	1.21	285.3	1.30	-	-	-	-
LFRO_500R	-	-	-	-	280.9	1.10	285.1	1.50	280.1	0.9	284.3	1.01
LFRO_600R	-	-	-	-	281.0	1.10	285.2	1.50	280.0	0.92	284.2	1.20
LFRO_700R	-	-	-	-	281.2	0.90	285.3	1.59	280.0	1.20	284.2	1.30

Table S2. Fitting parameters of Ru 3d in the *ex-situ* XPS.

	Ru^{3+} $3d_{5/2}$		Ru^{3+} $3d_{3/2}$		Ru^{β} $3d_{5/2}$		Ru^{β} $3d_{3/2}$		Ru^{0} $3d_{5/2}$		Ru^{0} $3d_{5/2}$	
Line shape	LF(0.3,1,45,280)		LF(0.8,1,45,280)		LF(0.4,1,45,280)		LF(0.6,1,45,280)		LF(0.8,1,45,280)		LF(1.01,1.25,500,50)	
Samples	BE (eV)	FWHM	BE (eV)	FWHM	BE (eV)	FWHM	BE (eV)	FWHM	BE (eV)	FWHM	BE (eV)	FWHM
LFRO	282.4	1.02	286.6	1.30	281.2	0.92	285.3	1.40	-	-	-	-
LFRO_300R	282.3	1.04	286.5	1.25	281.1	0.93	285.3	1.50	-	-	-	-
LFRO_400R	282.3	1.15	286.5	1.25	281.0	1.02	285.2	1.45	280.1	0.77	284.3	0.89
LFRO_500R	282.3	1.20	286.4	1.25	280.9	1.20	285.1	1.48	280.1	0.62	284.3	0.90
LFRO_600R	282.3	1.15	286.4	1.25	280.9	1.10	285.1	1.50	280.1	0.89	284.3	0.90
LFRO_700R	-	-	-	-	281.0	1.10	285.2	1.50	280.1	0.92	284.3	1.03
LFRO_800R	-	-	-	-	281.2	0.90	285.3	1.59	280.0	0.93	284.2	1.13
LFRO_300R-400O	282.4	1.12	286.5	1.37	281.1	0.75	285.3	1.40	-	-	-	-
LFRO_400R_400O	282.4	1.24	286.5	1.44	281.1	0.67	285.3	1.40	-	-	-	-
LFRO_500R-500O	282.4	1.10	286.5	1.43	281.1	0.67	285.3	1.40	-	-	-	-
LFRO_600R_600O	282.3	1.10	286.4	1.36	281.1	0.72	285.3	1.40	-	-	-	-
LFRO_700R-700O	282.4	1.35	286.5	1.40	281.1	0.96	285.3	1.40	-	-	-	-
LFRO_800R_800O	282.3	1.35	286.6	1.50	281.1	0.93	285.3	1.29	-	-	-	-

Chemical reactions occurring during reductive ruthenium exsolution using Kröger-Vink notation:

$$O_{O,surface}^{x} + H_2 \rightarrow V_{O,surface}^{2\cdot} + 2e^- + H_2O \quad \text{Eq. S1}$$

Oxygen extraction as water and source of electrons to conduct the Ru reduction.

$$O_{O,bulk}^{x} + V_{O,surface}^{2\cdot} \rightarrow O_{O,surface}^{x} + V_{O,bulk}^{2\cdot} \quad \text{Eq. S2}$$

Oxygen migration from the bulk to the surface

$$Ru_{Fe,surface}^{x} + (3-\beta)e^- \rightarrow Ru_{Fe,surface}^{(3-\beta)\prime} \quad \text{Eq. S3}$$

first Ru reduction step at the surface to produce Ru^{β}

$$Ru_{Fe,surface}^{(3-\beta)\prime} + (\beta)e^- \rightarrow Ru_{Fe,surface}^{3\prime} \quad \text{Eq. S4}$$

second reduction step to produce Ru^{0}

$$Ru_{Fe,surface}^{3\prime} \rightarrow Ru_{Ru}^{x} + V_{Fe,surface}^{3\prime} \quad \text{Eq. S5}$$

Ru migrates from the iron position to grow as clusters and nanoparticles

$$Ru_{Fe,bulk}^{x} + (3-\beta)e^- \rightarrow Ru_{Fe,bulk}^{(3-\beta)\prime} \quad \text{Eq. S6}$$

Ru reduction at the bulk to produce Ru^{β}

$$Ru_{Fe,bulk}^{(3-\beta)\prime} + V_{Fe,surface}^{3\prime} \rightarrow Ru_{Fe,surface}^{(3-\beta)\prime} + V_{Fe,bulk}^{3\prime} \quad \text{Eq. S7}$$

Ru migration from the bulk to the surface through the iron vacancies (exsolution)

$$La_{La,1}^{x}Fe_{Fe,1}^{x}O_{O,3}^{x} \quad \text{Eq. S8}$$

Stoichiometric perovskite

$$La_{La,1}^{x}Fe_{Fe,0.9}^{x}Ru_{Fe,0.1}^{x}O_{O,3}^{x} \quad \text{Eq. S9}$$

Ru substituted iron perovskite

$$La_{La,1}^{x}Fe_{Fe,0.9}^{x}V_{Fe,0.1}^{3\prime}O_{O,2.85}^{x}V_{O,0.15}^{2\cdot} \quad \text{Eq. S10}$$

Parent-oxide after complete exsolution of Ru

$$La_{La,1}^{x}Fe_{Fe,0.9}^{x}V_{Fe,0.1}^{3\prime}O_{O,2.85}^{x}V_{O,0.15}^{2\cdot} \rightarrow \left(La_{La,2}^{x}O_{O,3}^{x}\right)_{0.05} + La_{La,0.9}^{x}V_{La,0.1}^{3\prime}Fe_{Fe,0.9}^{x}V_{Fe,0.1}^{3\prime}O_{O,2.7}^{x}V_{O,0.3}^{2\cdot} \quad \text{Eq. S11}$$

Lanthanum precipitation

$$La_{La,0.9}^{x}V_{La,0.1}^{3\prime}Fe_{Fe,0.9}^{x}V_{Fe,0.1}^{3\prime}O_{O,2.7}^{x}V_{O,0.3}^{2\cdot} \equiv \left(La_{La,1}^{x}Fe_{Fe,1}^{x}O_{O,3}^{x}\right)_{0.9}\left(V_{La,1}^{3\prime}V_{Fe,1}^{3\prime}V_{O,3}^{2\cdot}\right)_{0.1} \quad \text{Eq. S12}$$

Parent oxide after Ru exsolution and lanthanum precipitation

4.3 List of Abbreviations

CA	citric acid
DFT	density functional theory
DRIFTS	diffuse reflectance infrared Fourier transform spectroscopy
EDS	energy dispersive spectroscopy
HAADF	high-angle annular dark-field imaging
LFO	$LaFeO_3$
LFRO	$LaFe_{0.9}Ru_{0.1}O_3$
LFRO_800R	$LaFe_{0.9}Ru_{0.1}O_3$ reduced at 800 °C
LFRO_800R_400O	$LaFe_{0.9}Ru_{0.1}O_3$ reduced at 800 °C and then oxidized at 400 °C
LPG	liquid petroleum gas
NA-XPS	near ambient X-ray photoelectron spectroscopy
NDIR	nondispersive infrared
NPs	nanoparticles
pO_2	oxygen partial pressure
SEM	scanning electron microscopy
SMSI	strong metal support interaction
SOFC	solid oxide fuel cell
STEM	scanning transmission electron microscopy
STY	space time yield
TEM	transmission electron microscopy
TOF	turnover frequency

UHV	ultra-high vacuum
VOCs	volatile organic compounds
WHSV	weight hourly space velocity
XPS	X-ray photoelectron spectroscopy
XRD	X-ray diffraction

4.4 List of Peer-Reviewed Publications

1. **Yu Wang**, Jaime Gallego, Wei Wang, Phillip Timmer, Min Ding, Alexander Spriewald Luciano, Tim Weber, Lorena Glatthaar, Yanglong Guo*, Bernd M. Smarsly*, Herbert Over*. Unveiling the Self-Activation of Exsolved $LaFe_{0.9}Ru_{0.1}O_3$ Perovskite during the Catalytic Total Oxidation of Propane. *Chin. J. Catal.* **2023**, *54*, 250–264.

2. **Yu Wang**, Paul Paciok, Lukas Pielsticker, Wei Wang, Alexander Spriewald Luciano, Min Ding, Lorena Glatthaar, Walid Hetaba, Yanglong Guo*, Jaime Gallego*, Bernd M. Smarsly*, Herbert Over*. Microscopic Insight into Ruthenium Exsolution from $LaFe_{0.9}Ru_{0.1}O_3$ Perovskite. *Chemistry of Materials*, In Press. doi: 10.1021/acs.chemmater.4c01084

3. Wei Wang, **Yu Wang**, Phillip Timmer, Alexander Spriewald Luciano, Lorena Glatthaar, Yun Guo*, Bernd M. Smarsly*, Herbert Over*. Hydrogen Incorporation in $Ru_xTi_{1-x}O_2$ Mixed Oxides Promotes Total Oxidation of Propane. *Inorganics*, **2023**, *11*, 330.

4. Wei Wang, Phillip Timmer, Alexander Spriewald Luciano, **Yu Wang**, Tim Weber, Lorena Glatthaar, Yun Guo*, Bernd M. Smarsly*, Herbert Over*. Inserted Hydrogen Promotes Oxidation Catalysis of Mixed $Ru_{0.3}Ti_{0.7}O_2$ as Exemplified with Total Propane Oxidation and the HCl Oxidation Reaction. *Catalysis Science & Technology*, **2023**, *13*, 1395–1408.

5. Zheng Wang, Omeir Khalid, Wei Wang, **Yu Wang**, Tim Weber, Alexander Spriewald Luciano, Wangcheng Zhan*, Bernd M. Smarsly*, Herbert Over*. Comparison Study of the Effect of CeO_2-based Carrier Materials on the Total oxidation of CO, Methane, and Propane over RuO_2. *Catalysis Science & Technology*, **2021**, *11*, 6839–6853.